UNIVERSITÀ DI PARMA

UNIVERSITA' DEGLI STUDI DI PARMA

DOTTORATO DI RICERCA IN
" *Scienze Chimiche*"

CICLO XXVII

Development of bio-based innovative materials for the packaging field

Coordinatore:
Chiar.mo Prof. Giovanni Maestri

Tutore:
Chiar.ma Prof.ssa Claudia Graiff

Dottoranda: Ylenia Ruberto

Anni Accademici 2021/2022 – 2023/2024

A mia sorella,
la certezza più
grande della mia vita

THESIS STRUCTURE

Chapter 1: The initial chapter focuses on the chemical modification of crystalline nanocellulose, aiming to enhance its properties or improve its intrinsic performance. This modification involves the creation of new covalent or electrostatic bonds through the addition of specific chemical groups.

Chapter 2: The second chapter examines various natural polysaccharides, investigating the formulation of suspensions to produce films and membranes for packaging purposes. The objective was to create environmentally friendly films that could serve as prototypes for materials with functional advantages over traditional plastics. Some of these films were enriched with antioxidants to produce active packaging, which helps slow the oxidation of packaged food and cosmetic products. This active packaging is especially beneficial for extending the shelf life of perishable goods. The films underwent a range of tests to assess their chemical and physical properties, such as mechanical strength, transparency, flexibility, and barrier performance. Additionally, the antioxidant activity of the enriched films was evaluated to confirm their effectiveness in preventing oxidation.

Chapter 3: The third chapter addresses the preparation of suspensions and their application as coatings for paper substrates using various deposition techniques like dip-coating, spin-coating, and slot-die coating. The research focuses on the ability of polysaccharide suspensions to enhance the barrier properties of paper against air, oxygen, and moisture.

Contents

Introduction

Chapter 1

Chapter 2

Chapter 3

Introduction

1. Packaging

The term ‘packaging’ refers to the instrument used for the preservation of a product including intangible aspects of the production process, industry and aesthetics (Wikipedia).

Packaging can be divided into three categories:

- Primary
- Secondary
- Tertiary

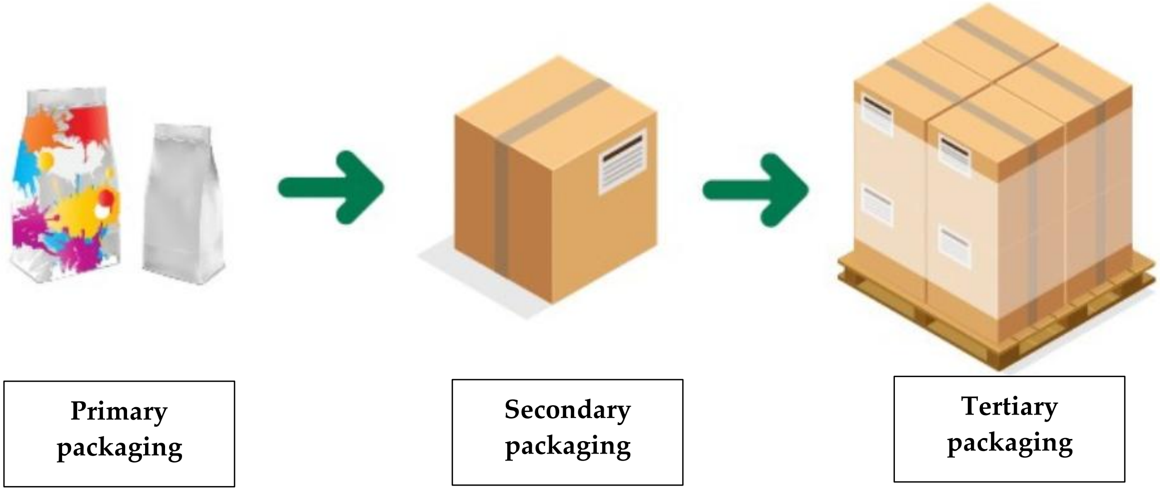

Figure 1 - Representative diagram of packaging types (Wikipedia)

Primary packaging refers to the part that is in direct contact with the product; the material used, and its properties play a crucial role in maintaining the product's preservation and quality. This packaging also displays mandatory information required by regulations, such as the expiration date, ingredients, and more.

Secondary or multipackaging serves as both the unit for sale to consumers and for retail distribution and does not directly touch the product. Its primary role is to communicate with the consumer, often through its visual appeal and design elements, to attract attention.

Tertiary packaging, on the other hand, is not intended for consumers. It is used to facilitate the transportation and handling of the product during distribution.

An emerging category of packaging gaining significant attention is active packaging. This type not only fulfills traditional packaging functions but also interacts with the product by releasing active molecules that help extend the product’s shelf life (Grimaldi et al., 2022).

For packaging to be deemed suitable, it must meet several key requirements. Among the most important characteristics are barrier properties, which refer to the material's ability to resist the penetration of moisture, oxygen, carbon dioxide, fats, and oils. Additionally, the material must be resistant to the passage of water, microorganisms, and aromatic compounds. Barrier properties are affected by the material's thickness and crystallinity, as well as the size and polarity of the substances trying to permeate it. The movement of permeants depends on factors such as storage conditions and the cohesive energy between the material and the molecule. Lower cohesive energy values lead to greater permeation, and vice versa. Water vapor and oxygen are the primary permeants because they can easily transfer from the external environment. Packaging made from paper or cardboard typically lacks these barrier properties, which is why it is often combined with materials like plastic, glass, or metal.

To improve the barrier properties of paper, synthetic polymers such as polyethylene (PE), polypropylene (PP), and ethylene vinyl alcohol (EVOH) are commonly used.

However, the use of non-renewable materials presents potential risks to both health and the environment by increasing the production of greenhouse gases like CO_2 and methane. Moreover, these materials complicate the recycling process, as plastics are insoluble in water, further raising costs. Recent data indicates that plastics represent a significant portion of global packaging, accounting for 36% of the market in 2020 (PlasticsEurope, n.d.). Their widespread use is linked to their low cost, strong mechanical properties, and versatility in production. The most commonly used polymers, including polyethylene (PE), polypropylene (PP), polyethylene terephthalate (PET), and polystyrene (PS), have demonstrated considerable adaptability across various industries, particularly in the food and pharmaceutical sectors (Hopewell et al., 2009).

1.1. Environmental issues related to the use of plastics in packaging

Although plastics offer several functional benefits, their widespread use has sparked significant environmental concerns. The production of plastic heavily relies on fossil fuels, contributing to greenhouse gas emissions. A major issue is the difficulty in managing plastic waste after consumption. Most plastic polymers can take centuries to break down in the environment, leading to their accumulation in both land and marine ecosystems, resulting in global pollution (Thompson et al., 2009). Microplastics, which are plastic particles smaller than 5 millimeters, present a direct threat to marine life and even human health, as they can be ingested by organisms and enter the food chain (Cole et al.). Additionally, plastics have harmful effects on biodiversity, degrading natural habitats and impeding the regenerative abilities of ecosystems (Rochman et al., 2013).

As a result, there has been growing interest in sustainable alternatives to petroleum- and metal-based plastics in recent years. Biopolymers have gained significant attention due to their advantageous properties, such as biodegradability, non-toxicity, and biocompatibility. Some of the most researched biopolymers include polysaccharides (such as chitin, chitosan, cellulose, starch, and alginate), lipids (various waxes and free fatty acids), and proteins (like zein and gluten).

1.2. Alternative materials to plastic in packaging

In response to the significant environmental issues linked to plastic use, there has been an increasing focus on researching and adopting alternative materials that maintain packaging functionality while minimizing environmental impact. Key alternatives include bioplastics, glass, metal, wood, and paper.

Bioplastics, which are made from renewable resources like corn, sugarcane, or other biomass, present a promising alternative to conventional polymers. These materials can be biodegradable or compostable, offering the advantage of shorter decomposition times compared to traditional plastics (PlasticsEurope, n.d.). However, challenges remain, including high production costs and the ability to biodegrade effectively under real-world environmental conditions.

While glass is non-biodegradable, it is a more sustainable option due to its 100% recyclability and the ability to be reused without losing its physical properties (Yuan et al., 2024). However, its weight and fragility can limit its use, particularly in food packaging.

Wood and paper, as natural materials, have gained popularity in sustainable packaging, especially when combined with waterproof coatings to enhance their durability (Shen et al., 2020). These materials offer an environmentally friendly, renewable option, although they may not be suitable for all types of products. The future of sustainable packaging will depend on the ability to balance industrial demands with environmental considerations, alongside ongoing research into new, high-performance, eco-friendly materials.

Natural polysaccharides like cellulose, chitosan, galactomannan, and glucomannan are attracting attention for their potential use in packaging. These biopolymers offer a sustainable alternative to traditional plastics, thanks to their biodegradability, biocompatibility, and widespread availability. Among these, cellulose and chitosan are the most widely studied, while galactomannan and glucomannan, though less known, are emerging as valuable components in packaging materials. The growing interest in these substances is driven by the need to address the environmental impact of plastic waste and the pursuit of sustainable solutions across industries, particularly in food and pharmaceuticals.

1.3. Natural polysaccharides

Natural polysaccharides are complex polymers made up of monosaccharides linked by glycosidic bonds. These biopolymers are essential in many biological and industrial processes due to their wide range of physicochemical properties. Key examples of natural polysaccharides include cellulose, starch, chitosan, and hyaluronic acid. Their supramolecular structure is defined by the self-assembly of polymer chains into organized forms such as microfibrils, lattices, or gels. The morphology of natural polysaccharides can vary significantly depending on their source and the treatments they undergo. The macroscopic properties of these polysaccharides are closely tied to their molecular and supramolecular structures. For example, cellulose is renowned for its excellent mechanical strength and thermal stability, making it suitable for use in various industries. Due to their properties and versatility, polysaccharides have been explored as raw materials for creating films and coatings that can serve as packaging materials, especially for food preservation, due to their effective barrier properties against gases like oxygen and carbon dioxide (Verma et al., 2024).

1.3.1. Cellulose and nanocellulose

Cellulose

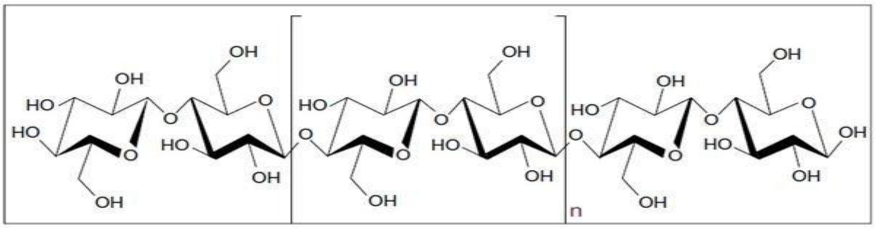

Figure 2 – Structure of cellulose (Ahmed-Haras Et. Al., 2020)

Cellulose, depicted in Figure 2, is the most abundant biopolymer on Earth (Pylkkänen et al., 2020), found in a variety of organisms such as plants, marine animals like tunicates, algae, fungi, bacteria, and invertebrates. It was first isolated in 1838 and is a high-molecular-weight homopolymer composed of anhydro-D-glucose units connected by α-1,4 glycosidic bonds, with each unit rotated 180° relative to the next (Klemm et al., 2005a). The polymerization degree (DP), or the number of glucose units in a chain, can reach up to 20,000 (Kroon-Batenburg & Kroon, 1997a). The repeating segment, called cellobiose, consists of two glucose units, each containing six hydroxyl groups that can form both inter- and intramolecular hydrogen bonds.

Cellulose chains are asymmetrical along their molecular axis: one end has a chemically reducing group, while the other has a pendant hydroxyl group, known as the non-reducing end. According to the literature, around 36 cellulose chains aggregate to form protofibrils, which then combine into microfibrils, ultimately forming the fibers that make up the plant cell walls (Lefebvre & Gray, 2005).

There are four polymorphic forms of cellulose: I, II, III, and IV, with forms I and II being the most common. Polymorph I has a crystalline structure with parallel chains, and it splits into two phases: Iα, found in bacterial cellulose, and Iβ, typical of cellulose derived from wood. The transition from polymorph I to polymorph II can occur irreversibly through mercerization with high concentrations of NaOH or by chemical regeneration with a suitable solvent followed by re-precipitation. Polymorph II has a more rigid structure due to the antiparallel arrangement of chains, which is advantageous in the paper industry (Kroon-Batenburg & Kroon, 1997b). Type III cellulose is produced by treating polymorph I with liquid ammonia at low temperatures or with organic amines such as ethylenediamine (EDA), and this transformation is reversible. Finally, polymorph IV is generated by subjecting polymorph III to high-temperature treatment.

Cellulose's linear structure and its ability to form fibers make it an ideal material for producing packaging. Cellulose derivatives like cellulose acetate and ethyl cellulose are widely used due to their excellent mechanical strength and their barrier properties against gases and moisture, making them suitable for food packaging (Moon et al., 2011). A major challenge with cellulose, however, is its hydrophilicity, which can hinder its ability to protect products from moisture effectively. Chemical modifications such as acetylation and grafting with synthetic or natural polymers can enhance its barrier properties. Additionally, combining cellulose with other natural or synthetic polymers to create composite films can improve barrier performance by reducing the absorption of oxygen and moisture (Jiang et al., 2021).

Nanocellulose

Nanocellulose is a highly promising material that has gained significant attention in both research and industrial sectors. It refers to cellulose derivatives that have been processed to achieve nanoscale structural dimensions. Nanocellulose is an advanced biomaterial derived from the chemical or mechanical treatment of cellulose. While the structure of cellulose is generally organized, some amorphous regions, caused by distortions in the fibers, are present. These regions can be removed through esterification of the hydroxyl groups (-OH) with organic or inorganic acids, or by breaking the oxygen atom of the glycosidic bond via chemical or mechanical treatments, resulting in partially crystalline nanocellulose.

Depending on the extraction method used, three types of nanocellulose can be obtained: (i) crystalline nanocellulose (CNC), primarily produced through chemical treatments of cellulose, (ii) fibrillated nanocellulose (CNF), which is derived from the mechanical disintegration of cellulose, and (iii) bacterial nanocellulose (BNC), produced by bacteria such as *Acetobacter*. Of these, CNC is the most common. The nanocrystals of CNC have a diameter ranging from 2 to 30 nm and can extend to several hundred nanometers in length. Nanocrystalline cellulose offers a variety of advantageous properties, including a large specific surface area, high elastic modulus, excellent thermal stability, optical transparency, biocompatibility, non-toxicity, and low production costs. Recent research has highlighted the impressive mechanical properties and transparency of nanocellulose, particularly CNC and CNF, making them ideal candidates for use in biodegradable packaging (Klemm et al., 2005b; Luo et al., 2020).

Nanocrystals are typically obtained through acid hydrolysis of cellulose fibers, a process that targets the degradation of glycosidic bonds in the more amorphous regions, which are more susceptible to acid attack (Lefebvre & Gray, 2005).

Cellulose can be extracted from various sources, including natural materials like cotton, agro-food waste, and industrial byproducts such as textile waste (Potenza et al., 2022). Common acids used in hydrolysis include sulfuric acid, hydrochloric acid, phosphoric acid, bromic acid, or mixtures of acids. During sulfuric acid hydrolysis, the acid not only catalyzes the hydrolysis but also forms a sulfuric ester with the primary hydroxyl group of the glycosidic ring, which contributes to the stability of the nanocrystals. The electrostatic repulsion from the sulfate anions on the surface of the crystals keeps the colloidal solutions stable. Two reaction mechanisms for acid hydrolysis have been described, as shown in Figure 3 (Lu & Hsieh, 2010a). In contrast, hydrolysis with hydrochloric acid (Araki et al., 1998) (Figure 4) does not alter the primary hydroxyl groups of cellulose, resulting in non-functionalized nanocrystals.

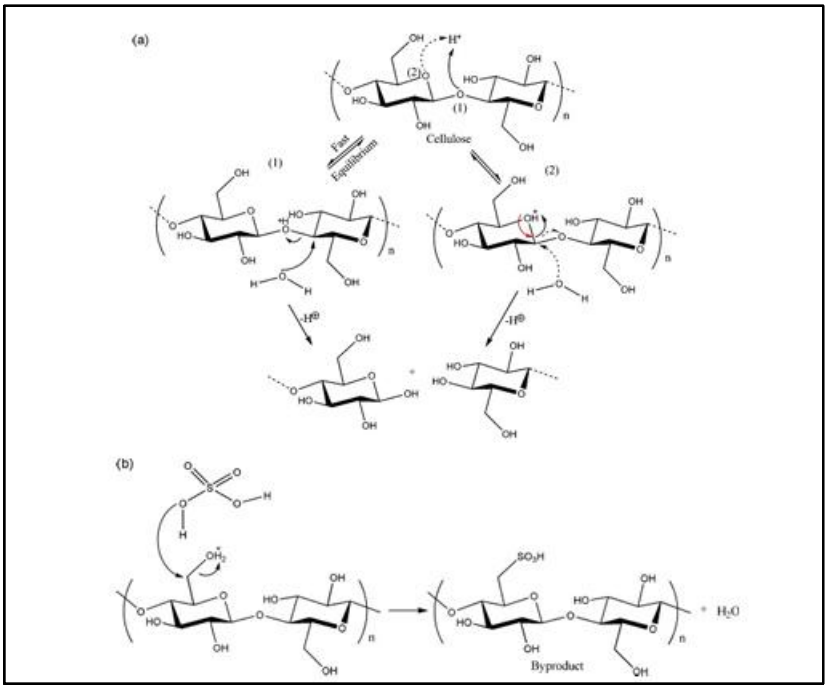

Figure 3 -a) Acid hydrolysis and b) Esterification with sulphuric acid (Lu & Hsieh, 2010b)

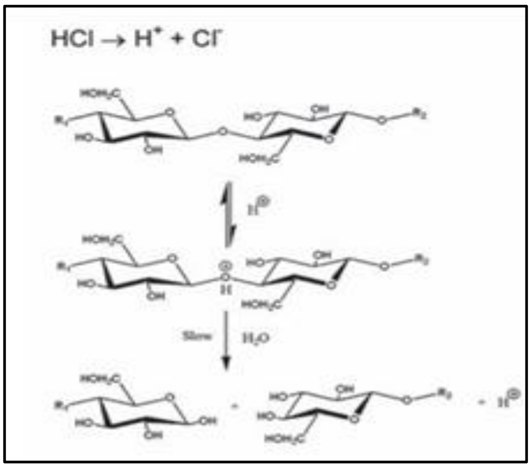

Figure 4 – Acid hydrolysis with hydrochloric acid (Habibi et Al. 2010a)

The surface functionalization of nanocellulose

The surface of nanocellulose crystals can be modified and functionalized (Araki et al., 1998; Habibi et al., 2010b), allowing for the creation of nanomaterials specifically designed for particular applications (see Figure 5). The modifications primarily target the hydroxyl groups (-CH_2OH) on the cellulose nanofibers, and one of the main goals of this functionalization is to alter the surface properties, such as enhancing their compatibility and dispersibility in particular solvents (Habibi et al., 2010b). Since cellulose is a hydrophilic material that tends to absorb moisture, various functionalization methods (Figure 5) are employed to control the moisture sensitivity of nanocellulose-based materials. These techniques include esterification, silylation, amidation, urethanization, and etherification, which help make the nanocellulose surface more hydrophobic. This functionalization primarily modifies the surface without altering the internal structure or the original morphology of the cellulose's alcohol groups.

Additionally, hydrophilic groups, such as carboxylic, phosphoric, or sulfonic groups, can be added to introduce a negative charge to the surface. This modification enables the stabilization of nanoparticles through electrostatic interactions. Chemical processes that allow the incorporation of these hydrophilic groups include phosphorylation, carboxymethylation, sulfonation, and oxidation (S. Sharma et al., 2023).

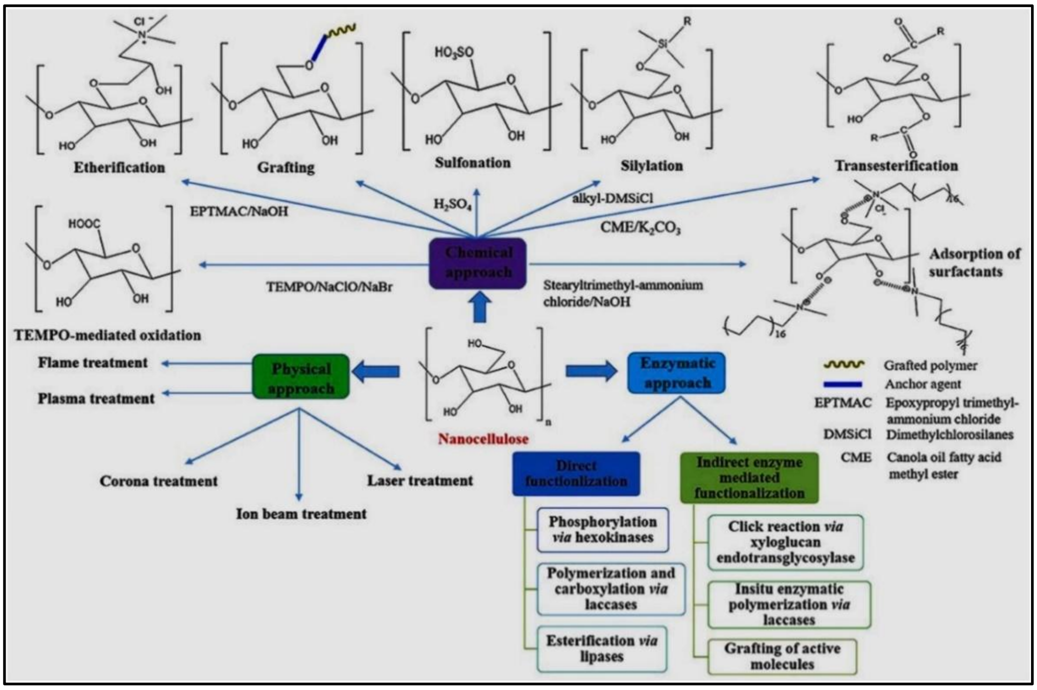

Figure 5 – Possible surface functionalization of cellulose nanocrystals (S. Sharma Et. Al., 2023)

Oxidation of nanocellulose

One of the most extensively studied functionalizations of CNC is the oxidation of the primary hydroxyl group to a carboxyl group. The oxidation method using 2,2,6,6-Tetramethylpiperidine-N-oxyl (TEMPO) is the most widely researched (Figure 6). TEMPO is a stable, water-soluble nitroxide radical that is commercially available and does not pose safety concerns, as it has tested negative in the Ames test. This oxidation is highly selective, converting the primary hydroxyl groups to carboxylic groups, with TEMPO acting as the mediator in the presence of NaBr (which serves as a co-catalyst) and NaClO (the primary oxidant). The optimal reaction conditions involve a pH of 10 and a temperature range between 0 and 10 °C. These conditions facilitate oxidation at the surface of the nanocrystals while preserving the internal crystalline structure.

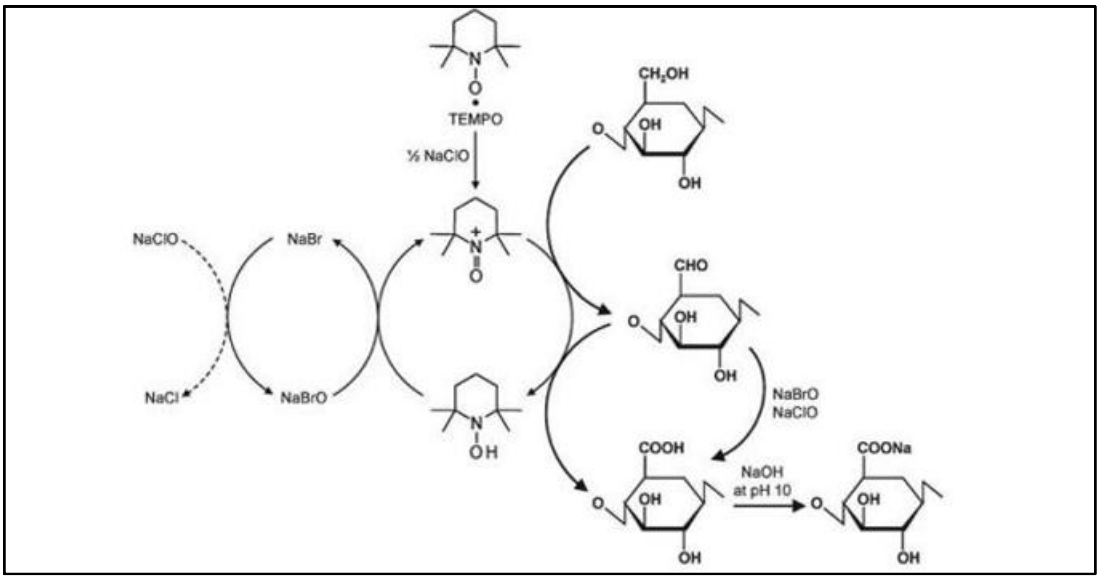

Figure 6 – Tempo-mediated cellulose oxidation reaction scheme (Habibi Et. Al., 2010a)

The primary oxidant, NaClO, oxidizes TEMPO to N-oxoammonium (TEMPO+), which then oxidizes the primary hydroxyl groups of cellulose to aldehydes (Kato et al., n.d.). Some of the aldehyde intermediates are further oxidized to carboxyl groups by NaClO, while the remaining ones undergo oxidation by TEMPO+. N-hydroxy-TEMPO is oxidized by NaBrO, which is formed from NaBr through oxidation by NaClO, regenerating the catalytically active N-oxo-ammonium species. Therefore, TEMPO and NaBr act as catalysts, and only NaClO is consumed during the oxidation process. NaClO reacts with TEMPO only during the initial stages of the reaction, after which NaBrO takes over, as it is more reactive towards TEMPO and N-hydroxy-TEMPO. Once the initial stages are completed, NaClO primarily oxidizes NaBr, which then regenerates NaBrO. The oxidation rate of both primary and secondary alcohols increases as the pH of the reaction solution rises, which is why most processes are carried out under basic conditions (Bailey et al., 2007).

Considering the chemo-selectivity of the reaction concerning pH, it was observed that under basic conditions, primary alcohols oxidize faster than secondary alcohols, while in acidic or neutral conditions, secondary alcohols oxidize more quickly. Energy calculations of the potential transition states indicated that the attack on the nitrogen atom is favored because the positive charge is more delocalized on this atom, leading to a more stable intermediate. Conversely, attacking the oxygen atom results in the formation of peroxide with a relatively weak O-O bond. Alkaline conditions promote a higher degree of dissociation of the primary hydroxyl groups, increasing their nucleophilicity and facilitating their reaction with TEMPO+. The covalent bond between primary alcohols and TEMPO+ is favored over bonding with secondary alcohols due to steric reasons. Under basic conditions, the hydration of aldehyde intermediates and subsequent deprotonation of an OH group interacting with TEMPO+ are also favored.

Cellulose nanocrystals oxidized by TEMPO are commonly used as precursors for further functionalization, such as:

Functionalization by amidation

In this type of functionalization, an amide covalent bond is formed between the carboxylate groups on the cellulose surface and the amine group of a primary amine.

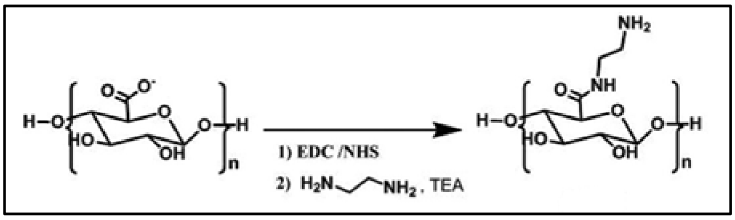

Figure 7 – Reaction scheme of oxidized nanocrystalline cellulose amidation (Ruiz-Palomero Et. Al., 2015)

During the reaction, an ester intermediate is formed between the activated carboxyl group and 1-ethyl-3-(3-dimethylaminopropyl) carbodiimide (EDC) (Eyley & Thielemans, 2014). Subsequently, attack by N-hydroxy succinimide (NHS) on the carboxylic carbon and elimination of a ureic derivative occurs. Finally, the primary amine binds to the carboxyl group forming the amide bond and restoring N-hydroxy succinimide.

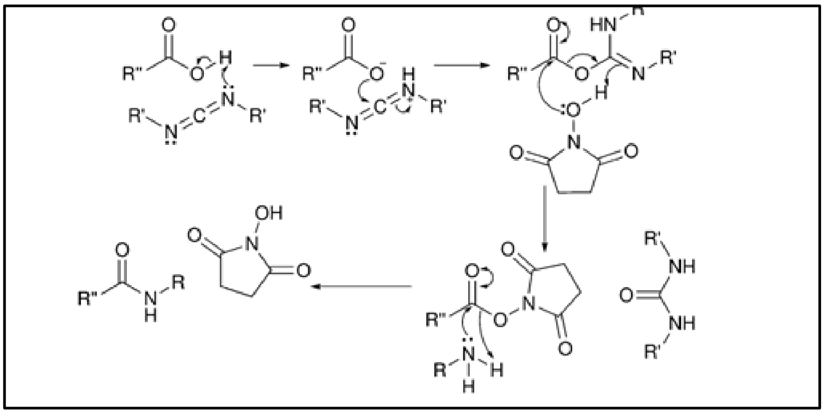

Figure 8 – Mechanism of the amidation reaction with EDC/NHS (Eyley & Thielemans, 2014)

Functionalization by esterification

The anhydroglucose units of cellulose nanocrystals (CNC) contain three -OH groups that are susceptible to modification. When cellulose nanocrystals (CNC) react with dodecyl succinic anhydride (DDSA), succinylation occurs, meaning a succinyl group is attached to the cellulose. This reaction primarily takes place at the C2 position, where modification of the hydroxyl group is most likely to happen. However, the grafting process can also impact the hydroxyl groups at the C3 and C6 positions of the glucose units in the cellulose structure. This modification with DDSA alters the properties of CNC, making it more hydrophobic, which enhances its potential as a reinforcing agent in composite or hydrophobic materials (Trinh et al., 2022).

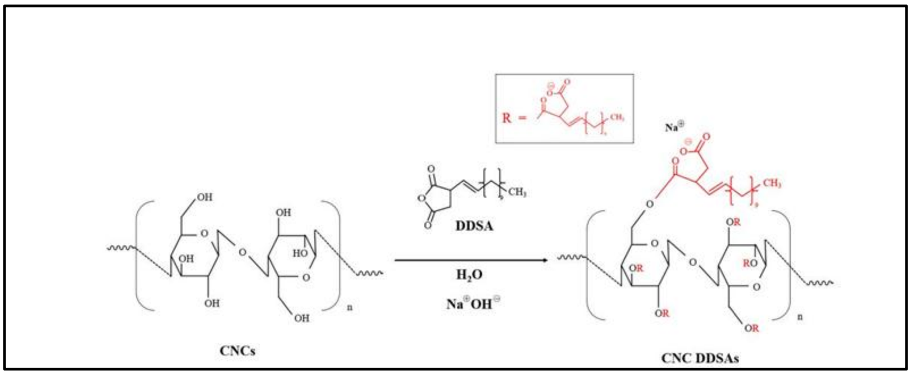

Figure 9 – Schematic diagram of succinylation reaction of nanocrystalline cellulose with dodecyl succinic anhydride (Trinh Et. Al., 2022)

1.3.2. Chitosan, Galactomannan and Glucomannan

Chitosan

Chitosan is a polysaccharide that is abundantly found in the cell walls of fungi and in the exoskeletons of crustaceans, insects, and other arthropods. Due to its diverse properties and versatility, it is extensively researched for use in biomedical, environmental, and industrial applications.

Chitosan is a linear polysaccharide composed of β-(1→4)-D-glucosamine (deacetylated) and N-acetyl-D-glucosamine (acetylated) units. Its structure closely resembles that of cellulose, but it differs by having an amine group (-NH_2) instead of a hydroxyl group (-OH) at the C2 position. This gives chitosan distinct characteristics, such as a positive charge in acidic environments, which is important for various applications (Rinaudo, 2006). Chitosan is produced by deacetylating chitin (Figure 10), which can be achieved through either chemical or enzymatic methods. The chemical method involves treating chitin with sodium hydroxide (NaOH) at elevated temperatures, while enzymatic deacetylation uses enzymes like chitin deacetylase. The degree of deacetylation (DD), or the ratio of free amine groups to acetylated groups, plays a crucial role in determining the material's properties (Kumar et al., 2004). Generally, a higher DD enhances solubility in acidic solutions and improves biological properties, affecting solubility, biocompatibility, and mechanical properties, with chitosan having a higher DD being more soluble in water.

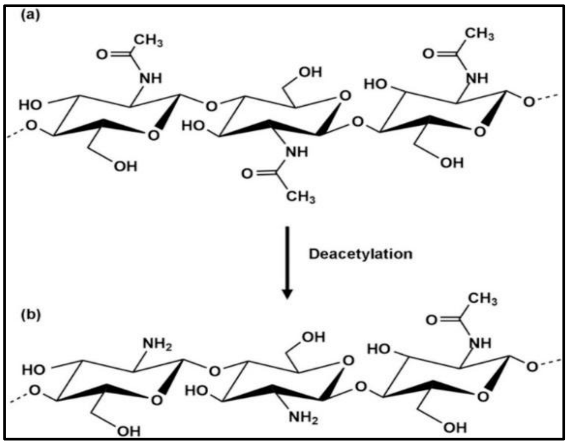

Figure 10 – Theoretical chemical structures of (a) chitin and (b) chitosan (Mei Et. Al., 2024)

Chitosan is biodegradable and biocompatible, characteristics that allow its use in biomedical applications for drug delivery and wound healing. Its biodegradability is linked to the activity of enzymes such as lysozyme, which degrade chitosan into non-toxic compounds. Furthermore, chitosan can easily be chemically modified to obtain derivatives with specific properties. For example, its reaction with anhydrides or acyl halides can produce hydrophobic derivatives, while its modification with thiol groups or negative charges can improve its interaction with proteins or cell membranes (Kean & Thanou, 2010). Chitosan shows excellent compatibility with other polysaccharides such as cellulose, making it a valuable biopolymer for composite materials. This compatibility is due to the formation of hydrogen bonds between the amine and hydroxyl groups of chitosan and those of cellulose, improving the mechanical strength and thermal stability of the material. Chitosan-cellulose composites are increasingly used in drug delivery and food packaging due to their combination of mechanical resilience and biodegradability (El-Araby et al., 2023).

Glucomannan and Galactomannan

Galactomannan and glucomannan are gaining recognition as promising polysaccharides in the packaging industry due to their functional properties and biodegradability. While not as widely used as materials like cellulose and chitosan, these polysaccharides are attracting attention for their ability to form gels, emulsify, and stabilize.

Glucomannan (Figure 11) is a water-soluble polysaccharide made up of long linear chains of glucose and mannose in a roughly 1:1.6 ratio. Its chemical structure features β (1→4) bonds linking the glucose and mannose units alternately along the polymer chain. The high hydrophilicity of glucomannan, coupled with its ability to form thick solutions even at low concentrations, results from the arrangement of hydroxyl groups (-OH) along the chain, which interact with water molecules (Kapoor et al., 2024). Derived primarily from the root of *Amorphophallus konjac*, glucomannan is known for its significant water absorption capacity, forming dense gels.

This gel-forming ability is particularly beneficial in packaging applications that require moisture barriers, enhancing the preservation of the packaged goods (Luo et al., 2019). Glucomannan can also be combined with other polysaccharides such as cellulose or chitosan to create composite films with improved mechanical and barrier properties, contributing to the development of more sustainable packaging options (Nampoothiri et al., 2020). The use of natural polysaccharides like galactomannan and glucomannan in packaging presents a promising solution to reducing the environmental impact of plastic waste. These materials are biodegradable and derived from renewable resources, making them an eco-friendly alternative. Their properties can be further enhanced through the incorporation of nanomaterials or chemical modifications, offering new opportunities for high-performance packaging in the food, pharmaceutical, and cosmetic industries (Shen et al., 2020). For example, Wu et al. (2020) found that incorporating tara gum (from 10% to 60%) significantly improved the strength of mixed gels compared to pure κ-carrageenan. Additionally, JT et al. (2020) developed a composite film combining clay, κ-carrageenan, and carob gum, which exhibited strong mechanical properties, reduced water vapor permeability (WVP), and improved antibacterial activity against *L. monocytogenes* when 16% clay was added by weight. Emerging technologies like 3D printing and customized bioplastics are facilitating the integration of these biopolymers into large-scale manufacturing, promoting a shift towards a more sustainable packaging industry (Shen et al., 2020).

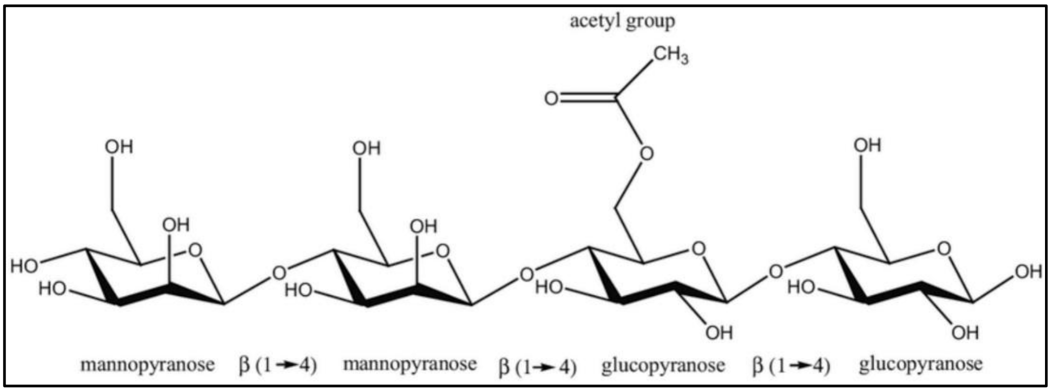

Figure 11 – Structure of KG (Kapoor Et. Al., 2024)

Galactomannans consist of a mannose (M) backbone with single galactose (G) residues linked by α-1,6 bonds. They are commonly found in the endosperm of legumes (Martins et al., 2010). The main commercial galactomannans include guar gum, tara gum, and carob seed gum, with M/G ratios of 2:1, 3:1, and 4:1, respectively. The branched structure gives galactomannan gelation and stabilization abilities, which are particularly useful in the food and pharmaceutical industries, where it is often used as a thickener and stabilizer in emulsions and suspensions (Sharma et al., 2021). Additionally, its compatibility with other biopolymers, such as cellulose, allows for enhanced mechanical properties and the formation of composite materials with potential applications in sustainable industrial sectors (P. Sharma et al., 2021). In the packaging sector, galactomannan stands out for its potential as a thickening or gelling agent, especially in the production of biodegradable films, where it improves the stability and shelf life of packaged products. Its mechanical properties can be optimized by combining it with other biopolymers or nanomaterials to increase strength and durability (Bhat et al., 2015).

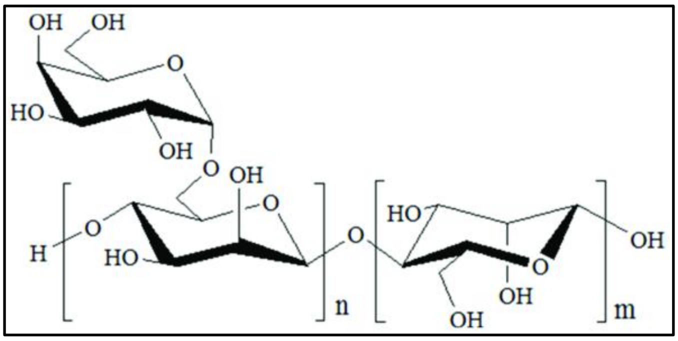

Figure 12 – Structure of Galactomannan (Wang Et. Al., 2023)

Both polysaccharides possess excellent biocompatible and biodegradable properties, making them ideal for applications in the biomedical and environmental sectors, including film production and the development of eco-friendly packaging materials (Nagarajan et al., 2024). Their combined use with other biopolymers, such as cellulose, can further enhance the mechanical and thermal properties of these materials, opening new frontiers for their use.

1.4. Use of polysaccharide suspensions as coating

Coating involves applying a thin film to substrates such as paper or lignocellulosic materials to enhance their properties, including strength, barrier performance, and durability. Reinforcing coatings are used to improve mechanical strength and moisture resistance, making them more suitable for packaging and other technical applications. Polysaccharides like chitosan and crystalline nanocellulose (CNC) are particularly promising for coatings due to their biodegradability and their ability to form robust films. Chitosan is valued for its antibacterial properties, while CNC is used to enhance mechanical strength. Positive results have been obtained when lignocellulosic substrates are treated with CNC (Basile et al., 2018; Bergamonti et al., 2020;Fornari et al., 2024 ; Haghighi Poshtiri et al., 2024). Additionally, CNC is noted for its transparency when applied to lignocellulosic materials (Bellia et al., 2023). Recent studies have demonstrated that incorporating these materials into matrices made of starch or other biopolymers significantly improves the barrier and mechanical properties of paper (Xue et al., 2022).

Viscosity is a critical property in coating processes, as it directly affects the ease of application, the formation of uniform films, and the final performance of the material. Materials with the appropriate viscosity allow for smooth application, ensuring an even distribution on the substrate without forming bubbles, streaks, or other imperfections that could degrade the coating's effectiveness. The optimal viscosity depends on the specific application and coating technique, such as spraying, gravure, or lamination (Cazón et al., 2017). In polysaccharide-based coatings like those using chitosan and CNC, viscosity plays a crucial role in the formation of strong, uniform films. Chitosan, which is soluble in acidic environments, can be prepared in solutions with varying viscosities, ideal for creating coatings with different mechanical and barrier properties (Priyadarshi & Rhim, 2020). CNC, with its crystalline structure, contributes to high viscosity and mechanical reinforcement, improving the resistance and barrier qualities of films, thereby optimizing coating performance (Cazón et al., 2017). Viscosity can also be modified by adding plasticizers or stabilizing agents, which enhance flexibility and resistance without compromising the coating's adhesion to the substrate (Potier et al., n.d.).

Coating deposition methods include a variety of techniques, such as:

- Blade coating (which uses a blade to spread the coating evenly on flat surfaces),
- Roll coating (where rollers apply the coating, suitable for large-scale continuous applications),
- Spray coating (which applies a spray of coating material and is used for irregular surfaces),
- Dip coating (where the substrate is immersed in the coating solution and then withdrawn to control the thickness),
- Electrodeposition (used for conductive surfaces, involving an electric current to deposit the coating),
- Slot-die coating (involves the uniform delivery of the solution over a surface through a distribution system, ensuring even coverage across the entire coating area).

The choice of deposition technique depends on the material characteristics and the specific coating requirements, with various adaptations made for reinforcement coatings, such as those based on nanocellulose or chitosan. The following section discusses two key deposition methods employed in the experiments for this thesis.

SPIN COATING

Spin coating is a technique used to apply a thin liquid layer onto a rotating substrate by utilizing centrifugal force (Figure 13). The coating is generally obtained from polymer solutions, where the viscosity and surface tension of the solution determine the formation of a uniform film on the substrate. As the substrate spins, the liquid thins out due to centrifugal movement and solvent evaporation.

The process consists of four main stages: dispensing the liquid, accelerating the substrate, centrifugal fluid flow outward, and drying through evaporation. The critical stages for determining the final coating thickness are the fluid flow (third stage) and evaporation (fourth stage). Factors such as the amount of liquid dispensed, final rotation speed, solution viscosity, concentration, and duration of spinning all influence the thickness and diffusion of the film. Generally, increasing the rotation speed results in a thinner film (Herrera et al., 2016).

However, spin coating has certain limitations, particularly at larger scales. These include high material waste (only 2-5% of the dispensed liquid adheres to the substrate, while the remaining 95-98% is discarded), challenges in achieving a uniform coating on larger substrates, and limited reproducibility. Despite these drawbacks, spin coating is commonly used in research laboratories, especially for developing new coating formulations for packaging and devices (El Amrani et al., 2024; Herrera et al., 2016; Sahu & Panigrahi, 2009).

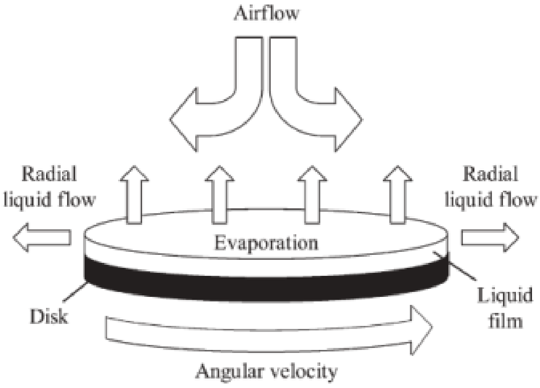

Figure 13 – Spin coating process

SLOT-DIE COATING

The Slot-Die coater is a highly versatile deposition technique used to apply thin liquid films onto a substrate. This technique allows for high levels of coating uniformity across the entire length/width of the surface, with film thickness ranging from a few nanometers to several micrometers, and deposition speeds ranging from a few centimeters per second to several meters per second. Coating materials are usually dissolved in solutions with varying viscosities. This is a pre-metered coating technique. The coating material is applied to the substrate through a coating head known as a slot-die. The advantages of the slot-die coating process include film thickness control, contactless coating mechanism, production speed, and scalability of coating areas. The disadvantages include operational issues due to the high complexity of the equipment and process optimization. Slot-die coating was developed for industrial use and is applied in large-scale production environments (Whitaker et al., 2018).

To achieve good deposition, it is necessary to control certain key parameters. These parameters are found within what is called the coating window, which is a map of coating parameters, and within this map are the ranges of values that can be applied to achieve a defect-free coating.

The coating window parameters include:

- Ratio between the slot-die height and the wet film thickness (Ho/twet)

The height of the slot-die is important for determining the quality of the deposited film, as it controls the distance the meniscus must travel to maintain the deposition process stable. The final wet film thickness (twet) is determined by the coating width (W), the volumetric pump flow rate (Q), and the relative speed between the slot-die and the substrate during coating (U).

Twet=Q/WU.

- Pump volume flow rate (Q)
- Coating speed (U)
- Pressure difference between the upstream and downstream faces of the meniscus (Λp)
- Capillary number of the liquid coating (Ca)

Capillarity refers to the phenomena due to the interaction between the molecules of a liquid and a solid, and to surface separation. The forces involved in this phenomenon are cohesion, adhesion, and surface tension. The capillary number (Ca) is a dimensionless number representing the relative effect of viscous forces compared to the surface tension of the substrate.

This number is defined as: Ca = μσ / Ɣ, where μ is the viscosity of the liquid, σ is the fluid velocity, and Ɣ is the surface tension.

For good deposition, the MINIMUM WET THICKNESS must be set, i.e., the minimum thickness that can be used at a given speed for good deposition. The higher the speed of the substrate movement, the greater the film thickness. When the deposited layer is thicker than the minimum deposition layer (T > Tmin), coating uniformity problems occur.

Deposition speeds Vmin, Vmax must also be set: substrate movement speeds below and above which good coating is not possible. Starting from zero speed, a suitable Vmin is reached, and then the maximum speed (Vmax) is set for a given film thickness (Whitaker et al., 2018)

The quality of the final film depends on many factors, including factors outside the ideal coating window. Slot-die coating is a mechanical process in which parameter optimization is crucial to obtain uniform coatings; however, mechanical imperfections such as irregular movement in the pump and coating systems, poor parallelism between the slot-die and the substrate, and external vibrations in the environment can lead to undesirable variations in film thickness and quality. Therefore, the slot-die coating equipment and its environment must be properly specified to meet the requirements of a given process and avoid defects in the coated film caused by imperfections in the hardware or environment.

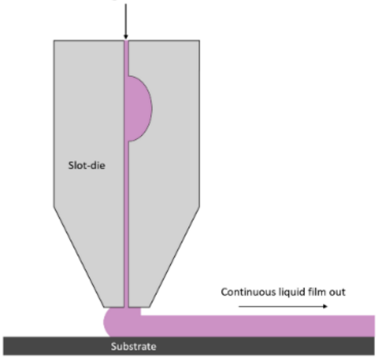

Figure 14 – Representative diagram of slot-die coating (Wikipedia)

Chapter 1

CNC SURFACE FUNCTIONALIZATION AND CHARACTERIZATION

1. Abstract

This chapter focuses on the study of the functionalization of nanocrystalline cellulose and the chemical characterization of the products obtained. Various modifications can be carried out on nanocellulose: non-covalent modifications, in which small molecules or macromolecules are adsorbed onto the surface of the nanocrystals by exploiting electrostatic and van der Waals interactions, or covalent modifications, in which the primary OH groups on the surface glucose units are replaced.

The functionalizations performed are:

- **Oxidation** mediated by the persistent radical 2,2,6,6-Tetramethylpiperidine-N-oxyl (TEMPO), which enables the selective oxidation of primary hydroxyl groups to carboxylate functionality.
- **Amidation** by means of 1-ethyl-3-(3-dimethylaminopropyl) carbodiimide hydrochloride (EDC·HCl) and N-hydroxy succinimide (NHS), yielding a further functionalisable compound. From the reaction between the amide product and different reagents, a material with modifiable properties can be produced.
- **Esterification** using dodecyl succinic anhydride (DDSA), chosen to provide the CNC with greater hydrophobicity due to its long chain.

2. Experimental

2.1. Materials

The following were used as solvents Distilled water, methanol (Sigma-Aldrich), ethanol (96%, Sigma Aldrich).

The reagents used are: Cellulose nanocrystals (CelluForce NCC®; production no. 2015-011) purchased from CelluForce (Canada); TEMPO (Sigma Aldrich); NaBr (Sigma Aldrich); NaClO (Sigma Aldrich); 1-ethyl-3-(3-dimethylaminopropyl) carbodiimide hydrochloride (EDC-HCl) (Sigma Aldrich); N-hydroxy succinimide (NHS) (Sigma Aldrich); ethylenediamine; triethyl amine (TEA); trioctyl methyl ammonium chloride (SERVA Feinbiochemica Heidelberg/ New York); and dodecyl succinic anhydride (DDSA) (SERVA Feinbiochemica Heidelberg/ New York).

2.2. Reaction of oxidation of cellulose sources: preparation of TEMPO-oxidated nanocellulose

Cellulose nanocrystals (CelluForce NCC®) were utilized to perform the oxidation reaction. The oxidation of the primary alcohol was achieved using the free radical 2,2,6,6-tetramethylpiperidine 1-oxyl (TEMPO), following the method previously developed in our laboratory as part of a thesis project (Fedele, 2021). In this procedure, a suspension of CNC was prepared, and TEMPO was added while maintaining a constant ratio of millimoles of TEMPO to grams of cellulose. TEMPO, NaBr (sodium bromide), and NaClO (sodium hypochlorite) were then added sequentially, with the quantities of NaBr and NaClO varied according to the details provided in Table 1. To ensure thorough removal of any residuals and achieve a neutral pH, the sample underwent dialysis using Sigma Aldrich cellulose acetate dialysis tubes (diameter=15mm, width=23mm pore size=MWCO 12400). The oxidised samples were named 'CNCox' followed by the experiment number.

Table 1 – Experimental data for TEMPO mediated oxidation reaction of CNC

Sample	Cellulose(g)	Tempo (nmol/g)	NaBr (mmol/g)	NaClO (mmol/g)	T (˚C)	Reaction time
CNCox1	0,22	2	0,5	6	25	6h
CNCox2	0,11	2	0,5	6	25	6h
CNCox3	0,22	2	0,5	12	25	6h
CNCox4	0,22	2	0,5	3	25	6h
CNCox5	0,11	2	1	6	25	6h
CNCox6	0,11	2	5	6	25	6h
CNCox7	0,11	2	10	6	25	6h
CNCox8	0,11	2	4	6	25	6h
CNCox9	0,11	2	4	6	25	6h
CNCox10	0,11	2	4	6	25	6h
CNCox11	0,11	2	10	6	25	6h
CNCox12	0,11	2	10	6	25	6h
CNCox13	0,11	2	4	6	25	6h
CNCox14	0,11	2	5	6	25	6h
CNCox15	0,11	2	4	5	25	6h
CNCox16	0,11	2	5	5	25	6h

2.3. CNC amidation reaction

The amidation reaction (at room temperature for 12 hours) was carried out following the procedure outlined in the literature (Ruiz-Palomero et al., 2015). A suspension was prepared by combining CNCox (700 mg), 1-ethyl-3-(3-dimethylaminopropyl) carbodiimide hydrochloride (EDC·HCl), and N-hydroxy succinimide (NHS) in methanol (20 mL). Then, a solution of ethylenediamine and triethylamine (TEA) in methanol (10 mL) was added to the suspension. The resulting precipitate was washed with dichloromethane and ethyl acetate to remove impurities and excess reagents, followed by a final wash with water to neutralize the pH to 7. The resulting samples were stored as a powder under the name CNCox-CH.

Table 2 – Table showing the amounts, expressed in mmol and mg, of the reactants used in the reaction

	EDC·HCl	NHS	Ethylenediamine	TEA
mmol	1,2	1,2	18	2,2
Mg	460	280	900	222
chemical structure	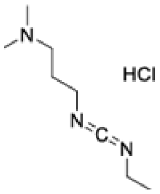	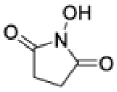		

2.4. Functionalization of CNC with docecyl succinic anhydride (DDSA)

The functionalization with dodecyl succinic anhydride (DDSA) was carried out following the procedure described in the literature (Trinh et al., 2022). DDSA was chosen due to its long alkenyl chain, which enhances the hydrophobicity of CNC (Trinh et al., 2022). The hydroxyl group (-OH) on the CNC surface reacts with the anhydride group of DDSA, forming an ester bond (-O-C=O) and releasing the anhydride. This reaction introduces an ester group ($-COO-C_{12}H_{25}$) onto the CNC surface. A 3% CNC solution in distilled water was prepared, and DDSA powder was added. The reaction was carried out at room temperature for approximately 6 hours, with the pH monitored and maintained at 9 by adding NaOH.

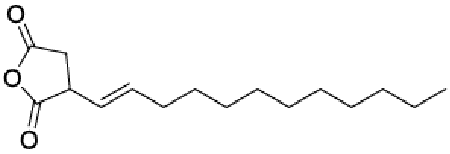

Figure 15 – Chemical structure of succinic anhydride (Wikipedia)

3. Methods

3.1. *pH measurements*

The pH of the aqueous suspensions of CNC was tested with a Crison Basic 20 pH meter. The average of the measurements taken in triplicate was taken into account.

3.2. *Conductimetric titration*

The degree of oxidation of the CNCox samples was determined using conductimetric titration, based on the method outlined by Habibi et al. (2006), with a Dosimat 665 dispenser (Metrohm) and a Crison microCM 2201 conductometer. Prior to the titration, 50 μL of 1.2 M HCl was added. The samples were titrated with a standardized 0.00978 M NaOH solution, prepared using potassium hydrogen phthalate, and dispensed with an automated burette. The conductivity was recorded after each addition of titrant. Multiple trials were performed to identify the optimal number of data points to accurately generate the titration curve. A total of 15 mL of titrant was used, with measurements taken at 1 mL intervals from 0 to 4 mL, at 0.3 mL intervals from 4 to 8 mL, and at 1 mL intervals from 8 to 15 mL. Once the data were collected, the equivalence volumes for the titration of the strong acid and weak acid were calculated. The difference between these two volumes, in terms of equivalents, represents the amount of weak acid, which correlates with the quantity of oxidized nanocrystals. The titration curve consists of three segments: the first segment (Figure 1) represents the titration of the strong acid, which was added in a known amount to each sample. In this phase, the conductivity decreases linearly as NaOH is added, due to the neutralization of free protons, which contribute to the solution's conductivity. Once the buffer region is reached, the curve flattens, as the carboxylated cellulose nanocrystals behave as a weak acid, following the equilibrium:

$$\text{CNC-COOH} \rightleftarrows \text{CNC-COO}^- + \text{H}^+$$

Finally, with excess NaOH, the conductivity increases due to the presence of OH^- ions in the solution. To determine the equivalent volume from the titration curve, the length of the plateau must be identified, which corresponds to the difference between the volume where the buffer system ends and the volume where it begins. The initial volume of the buffer system is determined by the intersection point of the line representing the strong acid phase (orange line in Figure 16) and the line interpolating the buffer region (black line in Figure 16). Similarly, the final volume of the buffer system is found by the intersection of the flat section of the curve and the line corresponding to the base excess (blue line in Figure 16).

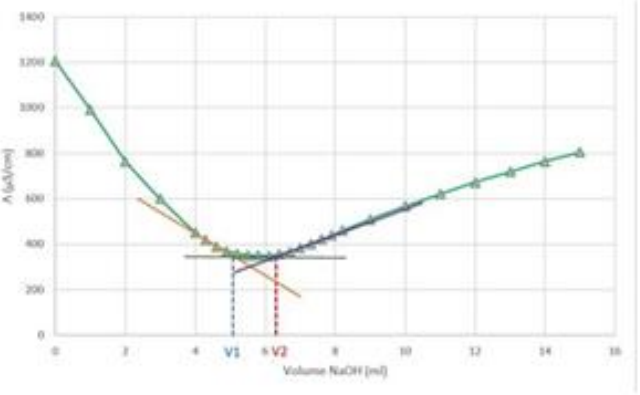

Figure 16 – Image related to the method for calculating the equivalent volume

After obtaining the two equivalence volumes, V1 and V2, formula (1) was used to calculate the degree of oxidation (OD %) of the individual samples:

$$DO\ (\%) = \frac{162\ x\ C\ x\ (V_2 - V_1)}{w - 36\ x\ C\ x\ \ (V_2 - V_1)} x\ 100$$

In this formula, C represents the concentration of NaOH (mol/L), V1 and V2 are the volumes of NaOH (in L), and wis the mass of the dried sample (in g); the value 36 corresponds to the difference between the molecular weight of an anhydrous glucose unit (AGU) and that of a unit of sodium salt, while 162 is the molecular mass of an AGU unit. The error associated with the degree of oxidation was also calculated, propagating the volume uncertainty in the parameter described above. The uncertainty on volume corresponds to 1/1000th of the flow rate of the burette, which in this case is 50 mL.

3.3. Fourier Transform Infrared Spectroscopy (FTIR)

FTIR spectra, in ATR mode, of all samples were obtained using the Thermo-Nicolet Nexus spectrometer, equipped with the Thermo Smart Orbit ATR diamond accessory, in the range 4000-400 cm^{-1} and with a spectral resolution of 4 cm^{-1}. The software used for curve fitting LabSpec 5 (Jobin Yvon Horiba, Kyoto, Japan).

3.4. Solid-state NMR (SSNMR)

SSNMR measurements were carried out using a Bruker Avance Neo spectrometer, operating at Larmor frequencies of 500.13 MHz for ^{1}H and 125.77 MHz for ^{13}C. Depending on the sample size, either a double-resonance CP/MAS probe (with 4 mm rotors) or a triple-resonance H/X/Y CP/MAS probe (with 2.5 mm rotors) was employed. The ^{13}C experiments were performed at various MAS frequencies (5-15 kHz), using a CP ^{1}H-^{13}C sequence with a contact time of 1 ms, selected based on preliminary tests and literature references, and a recycling delay of 5-7 seconds. The number of scans ranged from 400 to 40,000, depending on the sample and probe used. The ^{13}C chemical shifts were referenced to the signal of adamantane at 38.46 ppm as an external standard. All experiments were conducted at room temperature, using dry air as spin gas.

4. Results and discussion

4.1. Oxidised CNC results

pH mesurements

For all the solutions obtained, the pH values were measured (Table 3).

The presence of acid groups makes the solutions acidic (pH~3), amine groups or NaOH make the solutions basic (pH~10). In the case of oxidised cellulose, the dialysis process makes it possible to eliminate reagents with pH values close to neutrality.

Table 3 – Results of pH measurement

SAMPLE	pH
CNC-OX	6.2 (5)
CNC-NH	8.3 (3)
CNC-DDSA	9.2(1)

Conductimetric titration

The degree of oxidation (OD%) of the oxidized CNC (CNCox) was evaluated through conductivity titration. The results, shown in Table 4, align with the literature (Habibi, 2014), ranging from 3% to 12%, depending on the amount of NaClO used. An exponential increase in the degree of oxidation is observed as the NaClO amount rises, confirming the effectiveness of the reaction. This trend is particularly noticeable in samples 1 and 3, where the NaClO amount increased from 6 to 12 mmol (Table 1). An increase in OD was noted for samples treated with 1 and 5 mmol/g, whereas no significant change occurred with a 10 mmol/g treatment. Additionally, the amount of co-catalyst necessary to achieve an optimal reaction rate was evaluated, aiming to minimize the use of both the co-catalyst and primary oxidant to balance reaction time and yield.

Two sets of samples, CNCox 12-13 and CNCox 14-15, were oxidized with 6 mmol and 5 mmol NaClO, respectively, using varying co-catalyst amounts. In both cases, the samples with a higher OD were those treated with a larger quantity of co-catalyst. Notably, a good degree of oxidation was achieved with samples CNCox 12 and 15 by using less oxidant but a higher amount of co-catalyst. To investigate the role of basicity in the reaction, samples CNCox 8, 9, and 10 were prepared by adding different amounts of NaOH before introducing the primary oxidant. The ratios were 0 mmol:1g (CNCox 11), 6 mmol:1g (CNCox 12), and 12 mmol:1g (CNCox 13). The results indicate that adjusting the pH with a strong base had no significant impact on the reaction.

This suggests that the addition of the primary oxidant is sufficient to create a suitable basic environment to start the reaction. The timing of the reactions was also evaluated by performing some syntheses. It was observed that about 3h of reaction time is required to obtain a good D0.

Table 4 – Results of conductimetric titration

SAMPLE	DO (%)
CNCox1	4.1
CNCox2	3.1
CNCox3	13.0
CNCox4	2.1
CNCox5	5.4
CNCox6	9.3
CNCox7	6.9
CNCox8	7.1
CNCox9	5.3
CNCox10	6.0
CNCox11	3.0
CNCox12	9.6
CNCox13	8.1
CNCox14	9.9
CNCox15	7.2
CNCox16	9.8

Fourier Transform Infrared Spectroscopy (FTIR)

To confirm the oxidation reaction of nanocrystalline cellulose (CNC), the product was characterized by FTIR spectroscopy. Figure 17 shows a spectroscopic comparison between CNCox and the non-oxidized starting CNC.

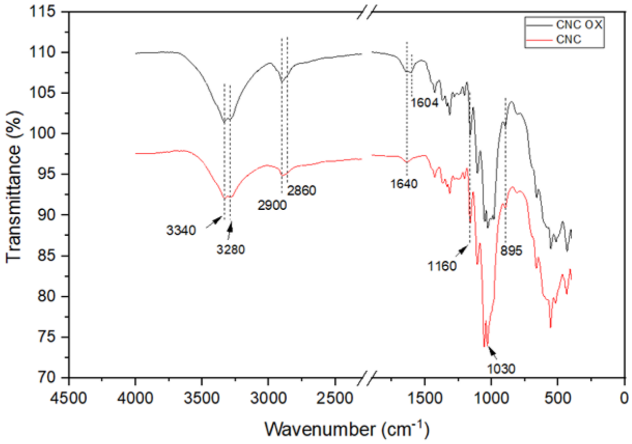

Figure 17 – Spectroscopic comparison between CNCox and CNC

From the spectroscopic analysis, it is evident that the CNC bands are primarily characterized by vibrations linked to the OH groups. The bands corresponding to the stretching vibrations of the OH groups involved in intermolecular hydrogen bonding appear at 3340 cm^{-1} and 3280 cm^{-1}. The stretching vibrations of the CH and CH_2 groups are observed around 2900 cm^{-1} and 2860 cm^{-1}, while bands at 1160 cm^{-1} and 1030 cm^{-1} are associated with the stretching vibrations of the ether group in the pyranose ring (νas C-O-C) and the C-OH group of carbon C6, respectively. At 1200 cm^{-1}, a weak peak is observed, attributed to the stretching vibration of the sulfate group resulting from hydrolysis with sulfuric acid. A peak at 895 cm^{-1} corresponds to the stretching vibration of the C-O-C group involved in the glycosidic bond between two adjacent rings (Potenza et al., 2022). The band at 1640 cm^{-1} is associated with the bending vibrations of adsorbed water molecules on the cellulose. Additionally, a weak band at 1604 cm^{-1}, related to the stretching vibration of the C=O carboxylate group, is seen in all CNCox spectra.

Solid-state NMR (SSNMR)

Cellulose oxidation was also investigated by means of the analytical technique solid-state nuclear magnetic resonance, thanks to which the signals attributed to the carbon atoms in the polymer chain can be appreciated and the crystallinity index of the samples can be derived.

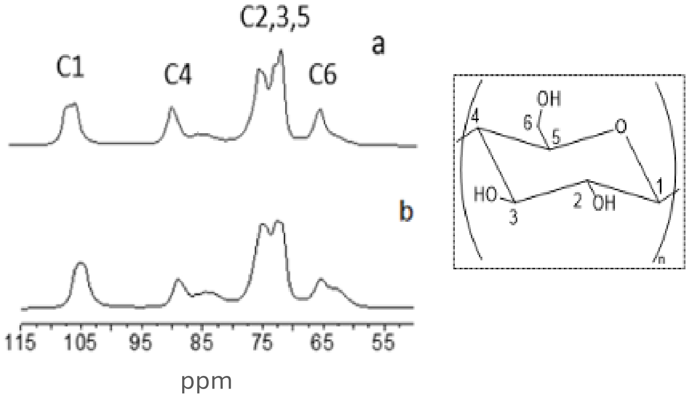

Figure 18 – ^{13}C CP/MAS spectrum for a): oxidized cellulose (CNCox); b) CNC. The numbering scheme of the carbon atoms of the 6-loop anhydroglucopyranose unit is shown in the box

The spectra for cellulose (b) and oxidized cellulose (a) are shown in the figure. In these spectra, signals for C1 are observed between 104 and 106 ppm, C2, C3, and C5 between 71 and 76 ppm, C4 signals between 82 and 90 ppm, and C6 signals between 62 and 66 ppm, which correspond to the carbon atoms of cellulose in their characteristic spectral regions.

For the C4 signals, the narrower band between 88 and 90 ppm is associated with the carbon atoms in the internal structure of the nanocrystals, while the broader band centered at 84 ppm corresponds to the cellulose chains on the surface of the crystals.

The classical numbering of the carbon atoms in the glucose molecule's six-membered ring was used to identify the carbon atoms (Atalla et al., 1980; Earl & VanderHart, 1980).

The signals corresponding to the amorphous part, for the other carbon atoms, are weaker than those associated with the crystalline part. Both spectra exhibit broad bands, indicating the low degree of order in the samples. The relative intensities of the signals from the crystalline and amorphous components can be used to estimate their quantities and the crystallinity index (CI).

To quantify the contributions of the crystalline and amorphous components of cellulose, as shown in Figure 19 and Table 5, the spectra were fitted using the non-linear least squares method available in the SPORT-NMR software (Geppi & Forte, 1999).

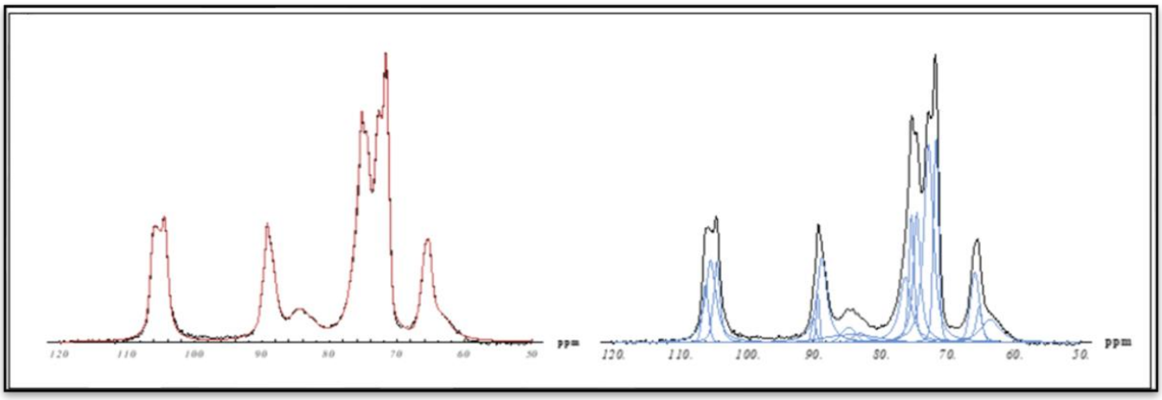

Figure 19 – ^{13}C CP/MAS spectrum fitting of oxidized cellulose (CNCox). On the left are the experimental (black) and calculated (red) spectra, on the right are the experimental spectrum (black) and the peaks for fitting (blue).

Table 5 – Chemical shift values obtained from the best "fit" and relative peak areas obtained from analysis of the ^{13}C CP/MAS spectrum of CNCox

Chemical shift (ppm)	Assignment	Area	Area %
106.09	Carbon 1	23.9	2.9
105.29	Carbon 1	76.4	9.3
104.34	Carbon1	39.0	4.7
89.90	Carbon4 (crystalline)	7.60	0.92
89.28	Carbon 4 (crystalline)	10.7	1.3
88.68	Carbon 4 (crystalline)	76.5	9.3
84.70	Carbon 4 (amorphous)	14.1	1.7
84.20	Carbon 4 (amorphous)	28.8	3.5
83.00	Carbon 4 (amorphous)	8.80	1.1
76.20	Carbon 2,3,5	67.0	8.1
75.27	Carbon 2,3,5	52.3	6.4
74.48	Carbon 2,3,5	79.7	9.7
72.73	Carbon 2,3,5	159	19
71.61	Carbon 2,3,5	74.8	9.1
65.81	Carbon 2,3,5	44.3	5.4
65.20	Carbon 6 (crystalline)	19.2	2.3
63.50	Carbon 4 (amorphous)	40.4	4.9

The integration of the C4 signal is used to calculate the crystallinity index (CI). The spectral areas considered are from 80 to 93 ppm (A80-93, which includes all C4 signals) and from 86.5 to 93 ppm (A86-93, representing the crystalline C4 signals).

The crystallinity index is calculated using the following formula:

$$CI = A86\text{-}93 / A80\text{-}94 \cdot 100$$

The relative intensities of the C4 signal components can also be employed to estimate the lateral dimensions of cellulose fibrils (LFDs) (Newman, 1999).

Assuming an average size of 0.57 nm for the cellulose polymer, the average LFD value is determined by the formula:

$$LFD = 0.57 \cdot n$$

where n refers to the number of cellulose polymer chains perpendicular to the cross-section of the nanocrystalline cellulose.

Table 6 – Crystallinity index (CI) and lateral fibril size (LFD) of oxidized cellulose from spectra analysis and signal integration.

Sample	s.r.	Probe	Method	CI	LFD
CNC-ox	15 kHz	4 mm	Integration	64%	5,7 nm
CNC-ox	15 kHz	4 mm	Fitting	65%	5,9 nm

Fig.20 shows the peak expansion around 174.9 ppm where the carboxyl group carbon signal can be observed (Cui et al.; 2014; Liu et al; 2018).

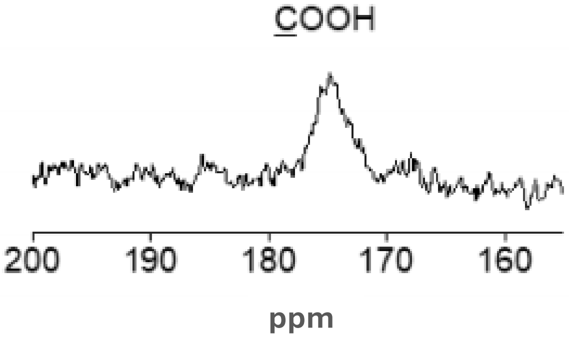

Figure 20 – Expansion of the ^{13}C CP MAS spectrum of the CNCox in the spectral region showing the COOH

4.2. Amidated cellulose results

Elemental analysis

To check for the presence of nitrogen atoms, an elemental analysis was carried out, the results of which, i.e. the percentage amount of carbon, hydrogen, nitrogen and sulphur atoms, are shown in Table 7.

Table 7 – Elementary analysis results

Sample	**C (%)**	**H (%)**	**N (%)**	**S (%)**
CNC	40,31	40,31	/	1,05
CNCox-NH	40,93	6,22	2,34	0,66

Fourier Transform Infrared Spectroscopy (FTIR)

Amidated nanocrystalline cellulose (CNCox-NH) displays a distinct spectrum with several notable absorption bands (Figure 21), each corresponding to specific vibrational modes of the functional groups in its structure. The band at 3340 cm^{-1} is attributed to the stretching vibration of the hydroxyl (OH) groups in cellulose. A broad band around 2900 cm^{-1} is due to the stretching vibration of the methyl ($-CH_3$) and methylene ($-CH_2-$) groups, which are part of the modified cellulose's organic structure. The band at 1640 cm^{-1} corresponds to the stretching vibration of the C=O double bond from the amide group formed during the amidation reaction. Lastly, the band at 1550 cm^{-1} is associated with the bending vibration of the N-H bond, characteristic of the amine group introduced into the cellulose structure.

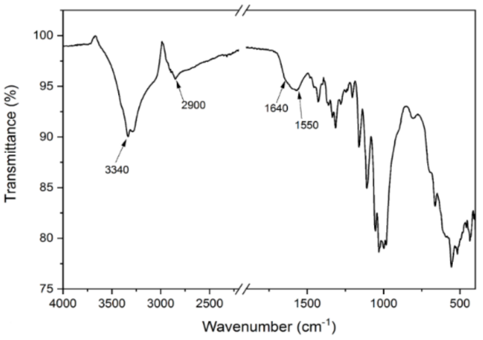

Figure 21 – FTIR spectrum of nanocrystalline cellulose functionalized by amidation

Solid state NMR (SSNMR)

To verify the amidation of the samples, a nuclear magnetic resonance analysis was performed, which resulted in the acquisition of the ^{13}C CP MAS spectra.

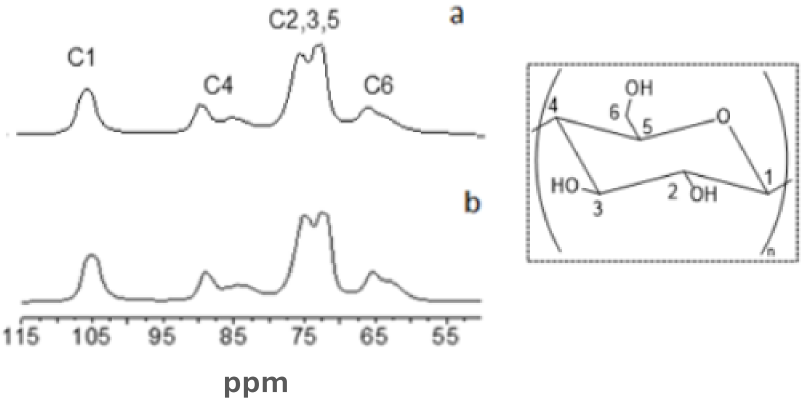

Figure 22 – ^{13}C CP/MAS spectrum of (a) animated cellulose (CNCox-NH) and (b) nanocrystalline cellulose (CNC Box shows the numbering scheme of the carbon atoms of the 6-loop anhydroglucopyranose unit)

As seen in Figure 22, both spectra exhibit characteristic cellulosic carbon signals in their respective spectral regions: C1 signals between 104 and 106 ppm, C2, C3, and C5 signals between 71 and 76 ppm, C4 signals between 82 and 90 ppm, and C6 signals between 62 and 66 ppm. In the NMR spectrum of CNCox-NH, compared to the pure CNC, the signals appear with lower intensity, suggesting a lower degree of functionalization. The relative intensities of the crystalline (inner) and amorphous (surface) signal components can be used to estimate the proportions of these different regions and determine the crystallinity index (CI). To assess the contributions of the crystalline and amorphous components, the spectra were fitted using the non-linear least squares method available in the SPORT-NMR software (Geppi & Forte, 1999).

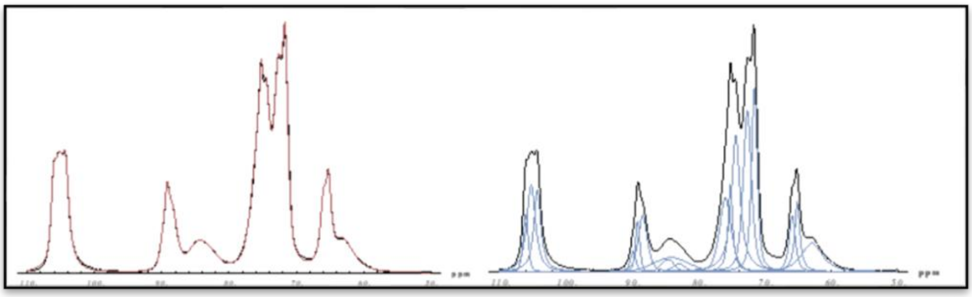

Figure 23 – Fitting of the ^{13}C CP/MAS spectrum of starch cellulose (CNCox-NH). On the left are the experimental (black) and calculated (red) spectra, on the right are the experimental spectrum (black) and the peaks for fitting (blue).

Table 8 – Best fit values of chemical shifts and relative peak areas obtained from analyst of the ^{13}C CP/MAS spectrum of CNCox-NH

Chemical shift (ppm)	Assignment	Area	Area %
106.08	Carbon 1	25.10	2.8
105.25	Carbon 1	75.4	8.5
104.30	Carbon1	60.90	6.9
89.90	Carbon4 (crystalline)	10.70	1.2
89.23	Carbon 4 (crystalline)	19.50	2.2
88.44	Carbon 4 (crystalline)	47.20	5.3
84.70	Carbon 4 (amorphous)	12.80	1.4
84.20	Carbon 4 (amorphous)	38.60	4.3
83.00	Carbon 4 (amorphous)	8.20	0.92
76.00	Carbon 2,3,5	76.40	8.6
75.25	Carbon 2,3,5	41.80	4.7
74.48	Carbon 2,3,5	123.8	14
72.70	Carbon 2,3,5	120.3	14
71.65	Carbon 2,3,5	99.00	11
65.90	Carbon 2,3,5	33.60	3.8
65.19	Carbon 6 (crystalline)	37.60	4.2
63.80	Carbon 4 (amorphous)	58.20	6.6

The integration and relative intensities of the C4 signal components can be used to estimate the crystallinity index (CI) and lateral dimensions of cellulose fibrils (LFDs), respectively (Newman; 1999).

Table 9 – Crystallinity index (CI) and lateral fibril size of starch cellulose from spectra analysis and signal integration

Sample	s.r.	Probe	Method	CI	LFD
CNC-NH	5 kHz	4 mm	Integration	58%	4,8 nm
CNC-NH	5 kHz	4 mm	Fitting	56%	4,5 nm

The reaction was confirmed by the expansion of the peaks around 40 and 175 ppm where the signals of CH_2 and CO carbons can be observed, indicating that the CNC functionalization reaction had taken place (Fig. 24) (Kumar et al.;2020; Pettignano et al.; 2019).

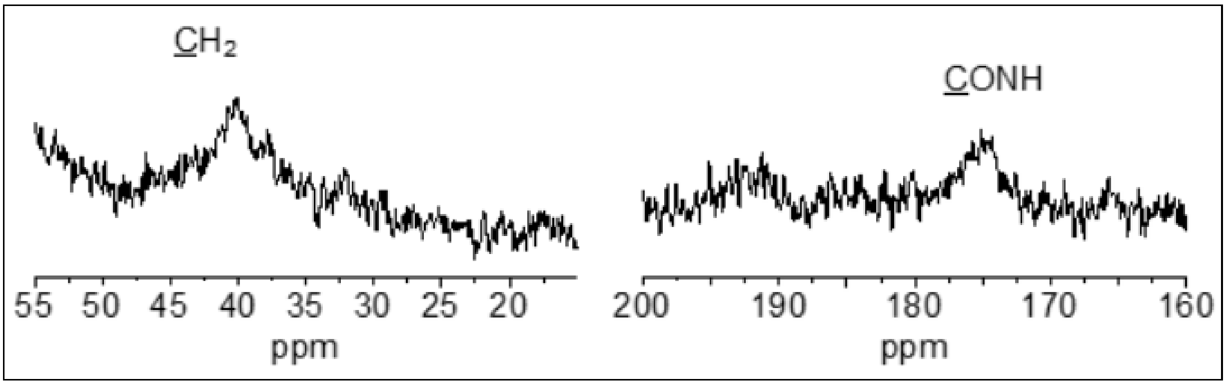

4.3. Results of the reaction between CNC and dodecyl succinic anhydride (DDSA)

Fourier Transform Infrared Spectroscopy (FTIR)

The characteristic profile of CNC is recognizable in all the spectra, where the vibration bands already discussed in paragraph 4.1 (Trinh et al.; 2022) are clearly visible.

Following the reaction of CNC with DDSA, new bands appear in the region between 1750 and 1500 cm^{-1}. The band at 1712 cm^{-1} is attributed to the stretching vibration of the ester carbonyl group from the anhydride, formed after reacting with the primary alcohol group of cellulose. The bands at 1568 cm^{-1} and 1550 cm^{-1} are related to the stretching vibrations of the carboxylate COO^- group in CNC/DDSA. The peak at 2960 cm^{-1} visible in the FTIR spectrum of CNC/DDSA is due to the stretching vibrations of the CH_3 group from the methylene chain introduced by DDSA. The absence of the bands at 1790 cm^{-1} and 1860 cm^{-1}, characteristic of anhydrides proves that no unreacted anhydrides are present in the product (Leszczyńska et al.; 2019).

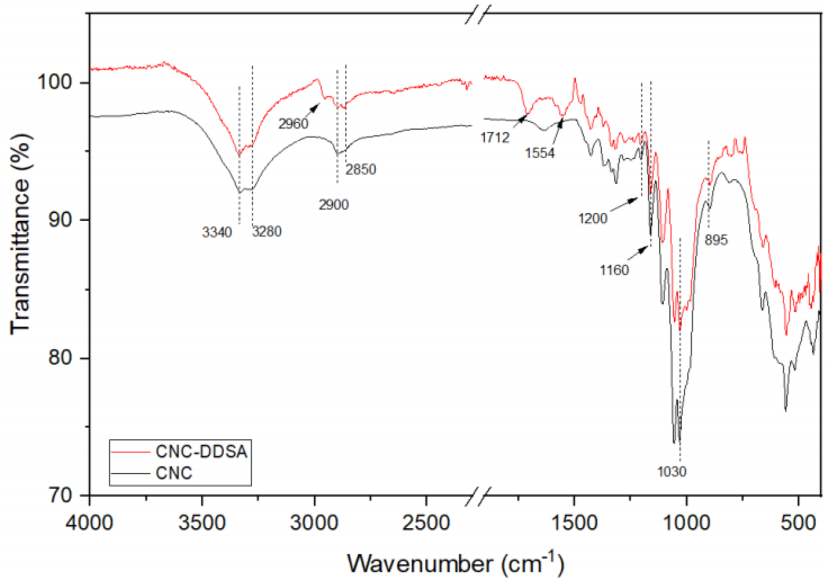

Figure 25 – Spectroscopic comparison between CNC and CNC-DDSA

5. *Conclusions*

The results highlight the success in optimizing the cellulose functionalization processes, with particular attention to oxidation. The oxidation of cellulose allows the introduction of carboxyl groups, which modify the chemical reactivity. Thanks to the optimization of oxidation parameters, we were able to achieve a satisfactory yield, with results ranging from 3% to 12% in the degree of oxidation. Furthermore, regarding the reaction times, we successfully optimized the duration, achieving times that strike a balance between reaction efficiency and good product yield. This means we managed to reduce the time required to obtain the desired results without compromising the quality and effectiveness of the reaction. The optimization of parameters has therefore allowed us to make the process faster and more efficient while maintaining control over the results obtained.

Chapter 2

DEVELOPMENT OF NATURAL POLYSACCHARIDES AND SUBSEQUENT ADDITIVATION WITH ANTIOXIDANT COMPOUNDS FOR PACKAGING FIELD

1. Abstract

The second chapter focuses on the formulation of new biodegradable materials based on natural polysaccharides, presented in the form of films with enhanced barrier properties towards oxygen and moisture.

For the formulation of the films, three polysaccharides were selected: chitosan, glucomannan, and galactomannan, known for their film-forming ability and their potential to interact with other polysaccharides or biopolymers to create blends. The films were analyzed through swelling degree, contact angle, and FT-IR spectroscopy to assess their chemical and physical characteristics. After identifying the polysaccharide with the best performance, it was combined with cellulose nanocrystals and microfibrillated cellulose, known for their reinforcing properties, to obtain blends. The blends were further characterized to study the interactions between functional groups and to analyze their wettability, thermal properties, and barrier properties to oxygen and water vapor.

In parallel, membranes based on cellulose nanocrystals (CNC) and microfibrillated cellulose (CMF) were developed, to which antioxidant compounds such as oregano essential oil and Vitamin C were added to create active packaging. The use of antioxidant compounds combined with natural materials like cellulose, has been studied to develop packaging that better protects products from oxidative agents, thus improving their longevity and quality. In this study, the ability of crystalline nanocellulose (CNC) and microfibrillated cellulose (CMF) to encapsulate the antioxidant agents was evaluated. In detail, the films added with oregano essential oil were studied to observe the absorption of the oil into the film as the CNC concentration varied.

2. Experimental

2.1. Materials

The solvents used were: Distilled water, alcohol vinegar (brillaceto). The reagents used were: Cellulose nanocrystals (CelluForce NCC®; production no. 2015-011) purchased from CelluForce (Canada); microfibrillated cellulose (90%) in the form of a thick white paste purchased from the Brazilian company Suzano; high molecular weight chitosan (290 - 320 kDa) (Sigma-Aldrich); galactomannan from carob seed flour (LBL) (Sigma-Aldrich); glucomannan (KGM) (Vita Natura); vegetable glycerol with >99% purity (Farmalabor); oregano essential oil purchased from the Italian company Fontana S.r.l.; ascorbic acid (Molecular weight 176.13 CAS-No: [50-81-7]) (RIEDEL-DE HAEN).

2.2. Formulation of films and blends based on natural polysaccharides

The sol-gel technique was used for the preparation of the films and blends (Grimaldi et al., 2022b). The formulation protocol adopted is the same for all films and blends: the reagents were precisely weighed, and then a solution in water and glycerol was prepared using a thermostatically controlled mechanical agitator. The temperature was varied depending on the polysaccharide, and the stirring lasted for 1 hour. The resulting suspensions were poured into plates and left to dry under a fume hood at room temperature (RT) for 48 hours.

Tables 10 and 11 show the formulations used for the preparation of the films and blends shown in Figures 26 and 27, respectively.

Table 10 – Formulations for films

Film	Solvent	Temperature (˚C)	Plasticizer Glycerol (%P/P)	Polysaccharides (%P/V)
Chitosan	Water/acetic acid (80:20)	65	2.5	1.7
Galactomannan	Water	85	2.5	1.4
Glucomannan	Water	25	2.5	0.3

Table 11 – Formulation of the blends

Blend	Solvent	Temperature (˚C)	Plasticizer Glycerol (%P/P)	Polysaccharides (%P/V)
Chitosan/CNC	Water/acetic acid (80:20)	65	2.5	1.7 1.7
Chitosan/CNC/CMF	Water	85	2.5	1.4 1.4 1.4

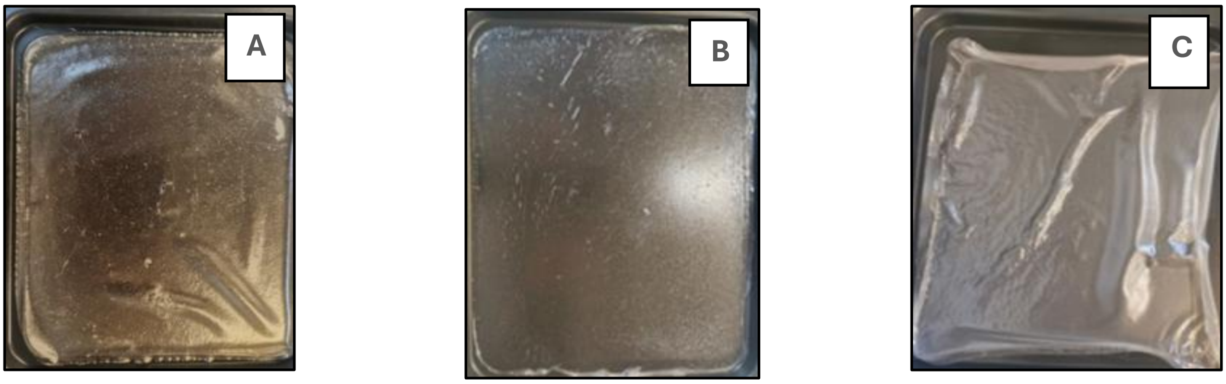

Figure 26 – Images of the films a) Chitosan; b) Glucomannan; c) Galactomannan

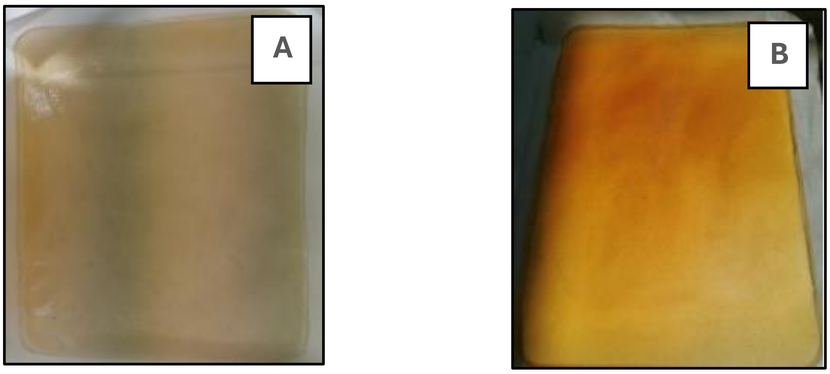

Figure 27 – Image of blends a) Chitosan/CNC; b) Chitosan/CNC/CMF

2.3. Formulation of films added with antioxidants

The films additivated with oregano essential oil (OEO) and ascorbic acid (Vit C) were prepared by formulating solutions based on nanocrystalline cellulose (CNC) and Microfibrillated cellulose (CMF) (which, despite its low hydrophobicity, has excellent film-forming properties), obtained through mechanical stirring at room temperature for one hour. Subsequently, the additives, namely oregano essential oil (OEO) or ascorbic acid (Vit C), were incorporated into the solutions, maintaining stirring for an additional hour. The prepared solutions were then poured into Petri dishes and left to dry under a fume hood for 24 hours.

In the case of the films added with OEO, the concentrations of CNC and CMF were varied to evaluate whether these changes would affect the absorption of the essential oil. The choice to vary the ratio of the two polymers was made to understand if the amount and arrangement of CNC and CMF had an impact on the efficiency with which the OEO was incorporated into the film. This variation in concentrations allows for the study of the interaction between the polymers and the essential oil, and how these affect the film's ability to retain and release the OEO over time.

For the films added with Vit C, both the absorption and release of ascorbic acid were evaluated. In this case, the goal was to understand how the solubility and distribution of ascorbic acid in the films were influenced by the polymer composition. Additionally, the release behavior of Vit C over time was studied to assess its ability to be released in a controlled and prolonged manner, an aspect particularly important for packaging applications that require continuous antioxidant protection.

The formulations of the added films are shown in tables 12 and 13 and in figure 28.

Table 12 – Formulation of films added with oregano essential oil (OEO)

Film	Solvent	Temperature (˚C)	Polysaccharides [Concentrations]	Additive [Concentrations]
CMF/CNC/OEO	Water	RT	1:1	0,5
CMF/CNC/EOE	Water	RT	1:2	0,5
CMF/OEO	Water	RT		0,5

Table 13 – Formulation of films added with ascorbic acid (vit. C)

Film	Solvent	Temperature (˚C)	Polysaccharides [Concentrations]	Additive [Concentrations]
CNC/CMF/Vit C	Water	RT	1:1:1	0,5

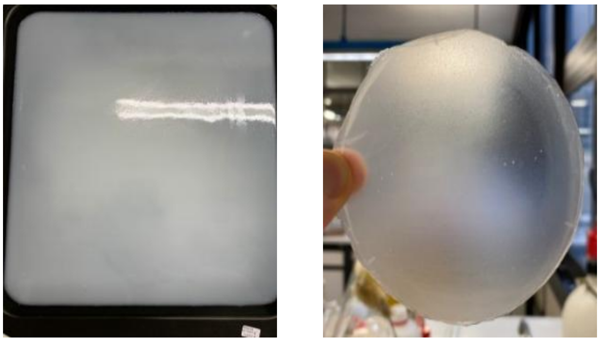

Figure 28 – On the left, photo of the film added with oregano essential oil, on the right, photo of the added with ascorbic acid

3. Characterization of films, blends and active packaging film

3.1. Degree of swelling

The films were cut with a puncher with a diameter of 20 mm, obtaining 5 samples from each film.

Each sample was weighed (Initial weight T0), dried in an oven at 60 °C, and reweighed (Dry weight: T1). Each dry sample was immersed in 25 mL of distilled water for 10 minutes, weighing it every 60 seconds (Wet weight). The degree of swelling was calculated using the following equation:

$$\text{Degree of swelling} = \frac{(wet\ weight - dry\ weight\ T1)}{dry\ weight\ T1}$$

3.2. Surface contact angle

The contact angle was measured using the OCA system from Dataphysics. The measurement parameters were set as follows:

- Syringe: DS-D 1000 SF
- Needle: SNS-D 051/025 (Øo = 0.51 mm)
- Liquid: water
- Dosage volume: 5 µL
- Dosage speed: 5 µL/s
- Measurement: sessile drop

Automatic calculation of the contact angle with the dpiMAX 20P software, vprofessional.

The substrates are placed on a support provided by Dataphysics and positioned on the mobile linear table. Using direct input from the software, the drop is dosed. The table on which the sample is placed is then moved upward until the drop is captured.

3.3.Fourier Transform Infrared Spectroscopy (FTIR)

The FT-IR analysis was performed as described in Chapter 1 section 3, sub-section 3.3.

3.4.Thermal properties

The thermogravimetric analysis (TGA) and differential scanning calorimetry (DSC) were performed on the samples using the PerkinElmer Thermogravimetric Analyzer TGA 8000 and the PerkinElmer Differential Scanning Calorimeter DSC 6000. The analysis parameters set for both tests are:

- Temperature range: RT - 300°C
- Heating rate: 10°C/min
- Gas flow: nitrogen

3.5.Permeability measurement (WVTR, OTR)

The water vapor transmission rate (WVTR, $g/m^2 \cdot d$) was evaluated under ambient conditions of temperature T = 23°C and relative humidity RH = 50%, according to the standard method ASTM F1249, using samples with a surface area of 50 cm^2. The relative humidity of the opposite chamber was conventionally considered to be 0%. Water vapor permeability (WVP) was calculated from the obtained WVTR values using the following formula: $WVP = WVTR \times l / (g \cdot mm/m^2 \cdot d \cdot kPa)$, where l represents the film thickness (in mm) and the partial pressure difference between the two sides of the sample is expressed in kPa. Specifically, the partial pressure of the permeating vapor was considered based on the test conditions, with a saturated vapor pressure of 2.810 kPa at 23°C and a relative humidity of the external side of 50%.

Regarding the oxygen transmission rate (OTR, $cm^3/m^2 \cdot d$), this was evaluated under the same temperature (T = 23°C) and relative humidity (RH = 50%) conditions, using samples with a surface area of 50 cm^2. Oxygen permeability (OP) was calculated from the obtained OTR values according to the formula: OP = OTR × l / (cm^3·mm/m^2·d·atm), where l represents the film thickness (mm) and the partial pressure difference between the two sides of the sample is expressed in atm. For the test, a pressure difference of 1 atm between the sides of the sample was considered, with the partial pressure of oxygen in nitrogen equal to zero, as the permeated oxygen through the film was continuously transported by the system to be analyzed at the end.

The thickness of each individual sample was determined by averaging 7 measurements taken with a micrometer at various points on the surface. Two samples for each composition were characterized.

For the barrier property characterization, the TotalPerm permeabilimeter (ExtraSolution) (PermTech srl, Italy) was used, which is equipped with two different sensors, one for oxygen (O2TR) and one for water vapor (WVTR), allowing the measurement of barrier properties for two distinct gases on the same surface. The samples were modeled and placed in the diffusion chamber, where the analysis was performed on a circular surface of 50 cm^2 (with a diameter of 8 cm).

The test conditions for the oxygen analysis were T = 23°C, RH = 50%, elevated conditioning level, and a minimum conditioning time of 6 hours. The conditions for the water vapor analysis were the same, with an elevated conditioning level.

The barrier properties of the produced samples were analyzed, specifically the variations in permeability (normalized based on the film thickness) for both oxygen and water vapor.

3.6. Chemical analysis

For the qualitative and quantitative analysis of the films added with oregano essential oil (OEO) and ascorbic acid (Vit C), the HPLC-UV-DAD technique (High-Performance Liquid Chromatography with UV-DAD detector) was used. The qualitative analysis identifies the presence of specific compounds in the film, while the quantitative analysis provides a measure of the concentration of these compounds. In particular, HPLC-UV-

DAD is useful for analyzing and quantifying compounds such as essential oils and vitamins present in the films, leveraging the UV-DAD detector's (dual wavelength detector) ability to monitor absorbances at specific wavelengths, providing accurate data on the sample composition.

To construct the calibration curve, samples were prepared from a solution of oregano essential oil in MeOH. The samples were then analyzed in triplicate using HPLC-UV-DAD, following the external standard method.

The aromatic film samples for targeted analysis of carvacrol and ascorbic acid were prepared by cutting squares, weighing them with an analytical balance, and placing them in a 100 mL sample container. To simulate 'worst-case' extraction conditions, 20 mL of 96% EtOH was added to the flask. The flask was then placed in a sonic bath for 30 minutes. The fragments were left in contact with the solvent for 24 hours to maximize extraction. Carvacrol and ascorbic acid extraction tests were set for 24 and 72 hours for carvacrol and 24, 48, and 240 hours for ascorbic acid.

At the end of the different time periods, the supernatant was collected from the flask and transferred to another flask, with 20 mL of ethanol added. After these steps, the solutions were filtered with a 0.45 μm PTFE filter the first time and then a second time with a 0.2 μm PTFE filter.

The filtered solutions were analyzed with HPLC-UV-DAD in duplicate.

The HPLC-UV-DAD is equipped with a C18 column. The selected method and separation parameters are set as follows:

- Isocratic mode with 60% A1 (MilliQ H2O) and 40% B2 (ACN)
- Injection volume = 100 μL
- Flow rate = 0.5 mL/min
- Stop time = 20 minutes
- The UV-DAD detector is set to a wavelength of 274 nm, and the reference is at 360 nm.

4. Results and discussion

4.1. Results obtained from the characterization of the films

Degree swelling of films

The swelling degree is a measure that quantifies the expansion or swelling of a material, in this case, a film, as a result of water absorption, and is typically expressed as the percentage change in the volume or mass of the sample compared to its initial state. In the context of the analysis of glucomannan, galactomannan, and chitosan films, the swelling degree was calculated to evaluate the swelling of the films when immersed in water.

Figure 29 shows the histograms related to the swelling degree of the films based on glucomannan, galactomannan, and chitosan, respectively.

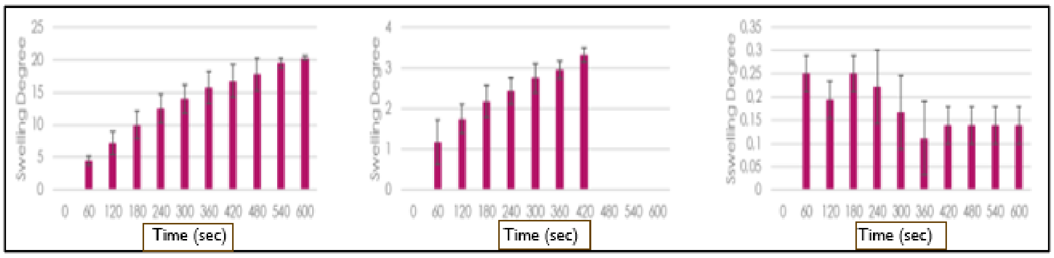

Figure 29 – Histograms relating to the degree of swelling of Glucomannan, Galactomannan and chitosan

As shown in Figure 29, the swelling degree of the glucomannan film (A) increases linearly over time. This indicates that the glucomannan film absorbs water in a continuous and progressive manner, swelling gradually. The galactomannan film (B) also shows the same linear pattern for water absorption, but after 420 seconds, it becomes completely dissolved. In contrast, the chitosan film exhibits a swelling degree that remains constant over time, without showing any swelling in water. This behavior indicates a greater hydrophobicity of the material (Silva et al., 2024).

Surface contact angle

The contact angle analyses reported confirm the hydrophobicity of chitosan, which was already shown by the swelling degree measurements and is also supported by the literature. Table 14 presents the estimated contact angle values for each film, along with the respective standard deviation. Figure 30 shows the image of the contact angle of the chitosan-based film.

Table 14 – Contact angle values for each film with their respective standard deviation

FILM	**A (°)± Dev.St.**
Galactomannan	69± 1.3
Glucomannan	22± 3.3
Chitosan	107± 0.8

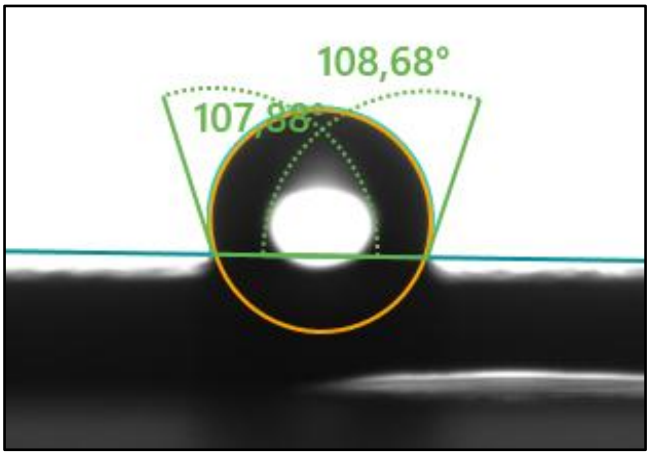

Figure 30 – Contact angle of the Chitosan film

Fourier Transform Infrared Spectroscopy (FTIR)

The FT-IR analysis (Figure 31) was performed on the chitosan film, which was found to be the most promising due to its good hydrophobic properties. This type of analysis was carried out to evaluate the chemical bonds present in chitosan and to observe how they might evolve as a result of the physicochemical interactions between the molecules during film formation. Specifically, the FT-IR spectrum of the chitosan film was compared with that of chitosan powder.

From the comparison of the FT-IR spectra, it is evident that in the film, the polysaccharide adopts a more ordered structure compared to the non-crosslinked chitosan powder. This structural change is due to the fact that, in solution, chitosan forms intramolecular interactions between its polar groups and intermolecular interactions with water molecules. In particular, the band at 3300 cm^{-1}, corresponding to the vibration of the amide and water, appears much more intense and defined in the film compared to the chitosan powder. Additionally, a characteristic band between 1100 and 1200 cm^{-1}, corresponding to the symmetric stretching of the glycosidic bond, is observed.

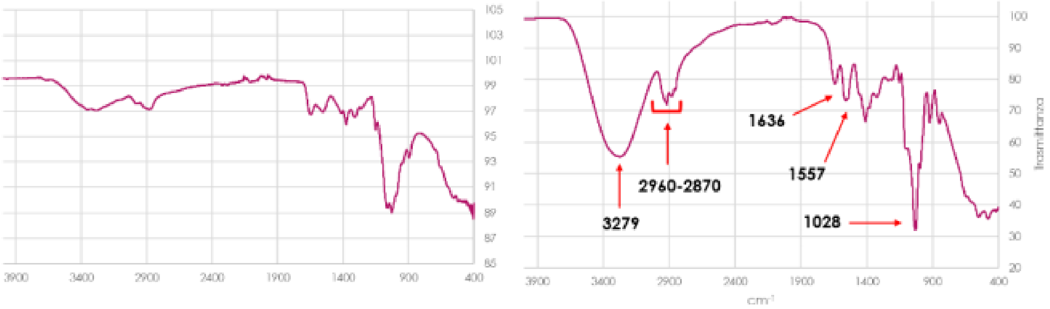

Figure 31 – Spectroscopic comparison between Chitosan powder (left) and Chitosan film (right)

4.2. Results obtained from the characterizations performed on the blends

Surface contact angle

Contact angle analyses on the Chitosan-CNC and Chitosan-CNC-CMF blends were performed to evaluate the variation in hydrophobicity values following the incorporation of cellulose matrices into the chitosan film. The analysis and calculation of the contact angles of the blends were carried out using the same equipment, software, and parameters already used for the film analyses.

In Figure 32 (left, right), a comparison of the contact angle images for the Chitosan-CNC blend (left) and the Chitosan-CNC-CMF blend (right) is shown. The value is higher for the Chitosan-CNC film (left), which has a contact angle greater than 90°, whereas the Chitosan-CNC-CMF blend (right) is hydrophilic and was therefore discarded from the subsequent characterizations.

This difference is due to structural differences and the surface properties of the two materials. Microfibrillated cellulose (MFC) is made up of larger and less ordered cellulose fibrils compared to nanocrystalline cellulose (CNC). The fibrils in MFC consist of microfibrils that are not fully crystalline, whereas CNC is composed of highly crystalline cellulose crystals. Additionally, both microfibrillated and nanocrystalline cellulose contain hydroxyl groups (-OH), which are hydrophilic. However, in CNC, the higher crystallinity reduces the exposure of these groups, promoting a less hydrophilic behavior. Microfibrillated cellulose has higher porosity than nanocrystalline cellulose, which means it can absorb more water, further reducing its hydrophobic properties compared to CNC, which has a more compact and less porous structure (Abbasi Moud, 2022; Ahankari et al., 2021).

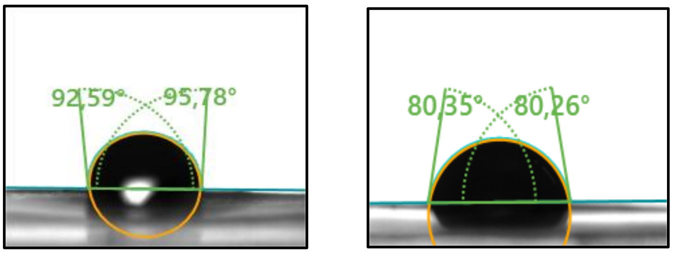

Figure 32 – Contact angles of the Chitosan/CNC blend (left) and the Chitosan/CNC/CMF blend (right)

Fourier Transform Infrared Spectroscopy (FTIR)

The FTIR-ATR analysis was performed to evaluate the types of chemical bonds present within the blends and the possible establishment of physicochemical interactions between the molecules. In this regard, a spectroscopic comparison was made between the chitosan film (left) and the chitosan/CNC blend (right).

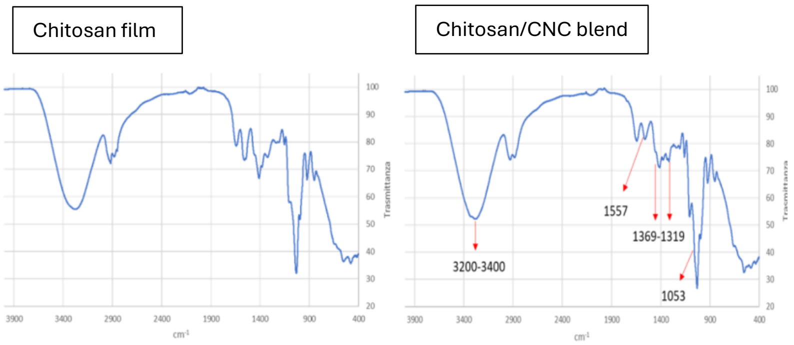

Figure 33 – FT-IR comparison between the Chitosan film and the Chitosan/CNC blend

As shown in the figure 33, the chitosan/CNC blend exhibits new bands at 1369, 1319, and 1053 cm^{-1}, corresponding to the stretching of the C-O bonds of CNC. Additionally, the band in the region between 3200-3400 cm^{-1}, related to the stretching of O-H bonds, is much sharper and more intense, suggesting the formation of hydrogen bonds between CNC and chitosan. Finally, the band at 1557 cm^{-1}, corresponding to the stretching of the N-H bond, appears less intense, suggesting the formation of electrostatic interactions and hydrogen bonds by the amine group. The obtained data are consistent with those reported in the literature for chitosan-CNC blends (Costa et al., 2021a; Kusmono et al., 2021; Yadav et al., 2020b).

Thermal analyses

To thoroughly assess the thermal stability of the Chitosan/CNC blend using TGA and DSC, a comparison was made between this blend and the chitosan-only film. The DSC results (Table 15) show that for all the films, two thermal transitions occur: the first related to the evaporation of water and glycerol, and the second related to the degradation of the chitosan chains. The Chitosan/CNC blend also presents a third transition due to the decomposition of CNC (342.72 °C).

It can be observed that the transition temperatures are higher in the Chitosan/CNC film compared to the chitosan-only film, suggesting that the presence of CNC improves the thermal stability of the film (Grząbka-Zasadzińska et al., 2017).

Table 15 – DSC results

FILM	DSC		
	Phenomenon 1	Phenomenon 2	Phenomenon 3
	T (˚C)	T (˚C)	T (˚C)
Chitosan	153.47	287.20	/
Chitosan/CNC	140.67	290.82	342.72

The TGA results (Table 16) show that for all the films, three phenomena occur that lead to a weight loss: the first (30–100 °C) related to the loss of water/acetic acid, the second (100–250 °C) related to the degradation of glycerol, and the third (250–400 °C) related to the decomposition and depolymerization of chitosan.

Table 16 – TGA results

FILM	TGA							
	Phenomenon 1		Phenomenon 2		Phenomenon 3		Phenomenon 4	
	T (˚C)	Loss weight	T (˚C)	Loss weight	T (˚C)	Loss weight	T (˚C)	Loss weight
Chitosan	30-100	23%	100-250	44%	250-400	21%	/	/
Chitosan/CNC	30-100	19%	100-250	33%	250-400	12%	300-400	18%

In the Chitosan/CNC film, a fourth phenomenon (300–400 °C) is present, related to the loss of CNC due to its degradation, confirming its presence in the polymeric matrix. Furthermore, the peak corresponding to the degradation of CNC (300–400 °C) overlaps with the same temperature range of chitosan degradation (250–350 °C). The obtained data are in perfect agreement with those reported in the literature for Chitosan/CNC blends (Costa et al., 2021b).

Permeability measurements (WVTR/WP; OTR/OP)

For the permeability analysis, the thickness of the samples was measured first, as the permeability values are normalized based on the film thickness. The thicknesses of the samples are reported in table 17.

Table 17 – Average thickness value of the two samples

Samples	**Average thicknesses [mm]**
Chitosan	0.423
Chitosan/CNC	0.534

Table 18 reports the data related to the permeability tests, specifically the values of oxygen permeability (OP) and water vapor permeability (WVP), both normalized along with the corresponding standard deviation.

Table 18 – Results of the oxygen permeability and water vapor permeability tests

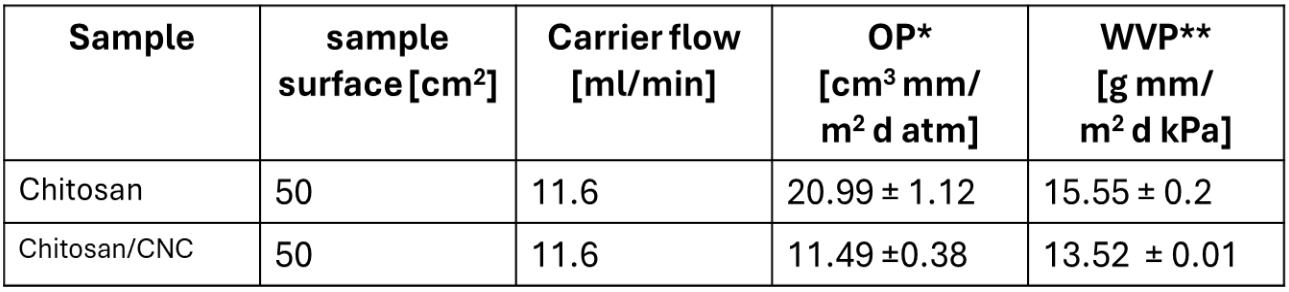

Sample	**sample surface [cm^2]**	**Carrier flow [ml/min]**	**OP* [cm^3 mm/ m^2 d atm]**	**WVP** [g mm/ m^2 d kPa]**
Chitosan	50	11.6	20.99 ± 1.12	15.55 ± 0.2
Chitosan/CNC	50	11.6	11.49 ±0.38	13.52 ± 0.01

It is observed that the chitosan-only film shows higher values of OP and WVP; thus, the addition of CNC to the composition improves the barrier properties, both for oxygen and moisture. Regarding oxygen permeability (OP), the Chitosan/CNC blend shows a decrease in the permeability value of about 45% compared to the chitosan-only film.

Water vapor permeability is also improved, with a reduction from a value of 15.55 ± 0.2 g·mm/m²·d·kPa for the chitosan-only film to a lower value of 13.52 ± 0.01 g·mm/m²·d·kPa and 0.52 ± 0.12 g·mm/m²·d·kPa for the Chitosan/CNC sample, resulting in a 15% improvement in moisture barrier properties.

Overall, the data indicates that the inclusion of CNC results in an increase in barrier properties, and in general, the measured barrier properties are promising and show significant improvements compared to the chitosan-only film.

Some studies in literature highlight the relationship between crystallinity and permeability, indicating that higher crystallinity is associated with lower permeability. The crystalline regions in a polymer film are less permeable, extending the path through which the permeant diffuses. Numerous studies have shown that intermolecular interactions (mainly hydrogen bonds and van der Waals interactions) lead to a more compact packing, higher cohesive energy density, and lower free volumes, which results in lower gas permeability. This could partly explain the very low permeability values observed (Babaei-Ghazvini et al., 2024; Salim et al., 2022).

4.3. Results obtained from the characterization of films added with oregano essential oil

Fourier Transform Infrared Spectroscopy (FTIR)

In the comparison between pure oil and the film doped with oregano essential oil (OEO) the characteristic signals of the oil (such as the peaks at 1465 cm^{-1} and 1426 cm^{-1}, associated with Carvacrol) and the aromatic peaks at 1622 cm^{-1} and 1591 cm^{-1} (associated with the C=C aromatic stretching vibration) are indicative of the presence of OEO in the film. These peaks were also identified in relation to the study by Solano Valderrama et al. (2017), which reported similar frequencies for pure OEO.

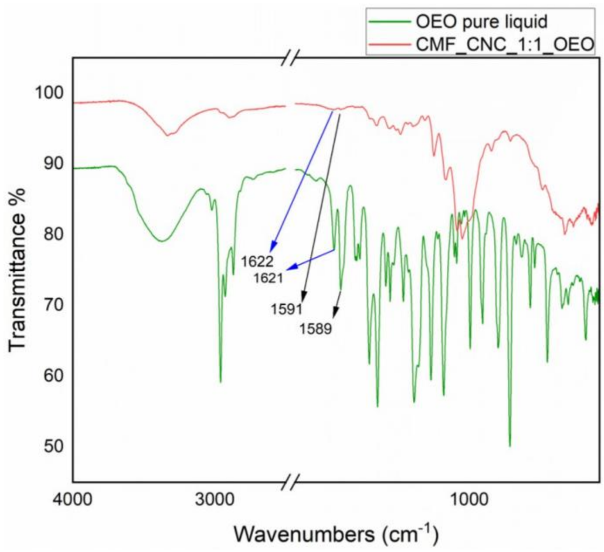

Figure 34 – FT-IR comparison between OEO and CNC/CMF/OEO film

The peaks at 1458 cm^{-1} and 1420 cm^{-1} are associated with Carvacrol. The absence or weakness of these peaks in the films may suggest a change in the interactions between OEO molecules when encapsulated in the film, or a partial alteration in the chemical structure. In the nanocrystalline, microfibrillated and oregano essential oil (CNC/CMF/OEO) doped film, the peaks are shifted to 1465 cm^{-1} and 1426 cm^{-1}. These shifts to higher wavenumbers could indicate changes in the interaction forces between Carvacrol and the polymer or other components in the film.

Chemical analysis

This section presents the results obtained from the HPLC-DAD data, derived from the extraction tests performed on the films loaded with OEO. A chromatogram of the CMF_CNC_1:1_OEO after 24 hours is shown as an example in Figure 35, where the Carvacrol peak is visible at 12 minutes.

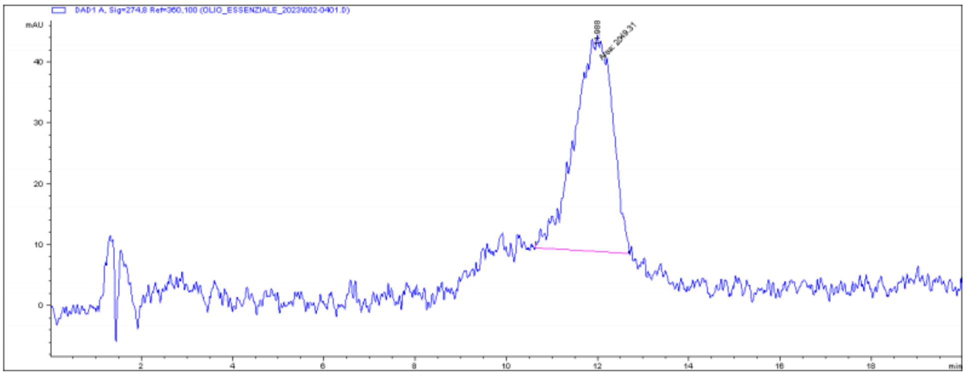

Figure 35 – Chromatogram of CMF/CNC_1:1_OEO after 24 hours

The experimental UV spectrum of Carvacrol is shown in Figure 35, and by comparing it with the literature (Figure 36) (Lopes Jesus, et al., 2021), it can be observed that there is good agreement between the two spectra.

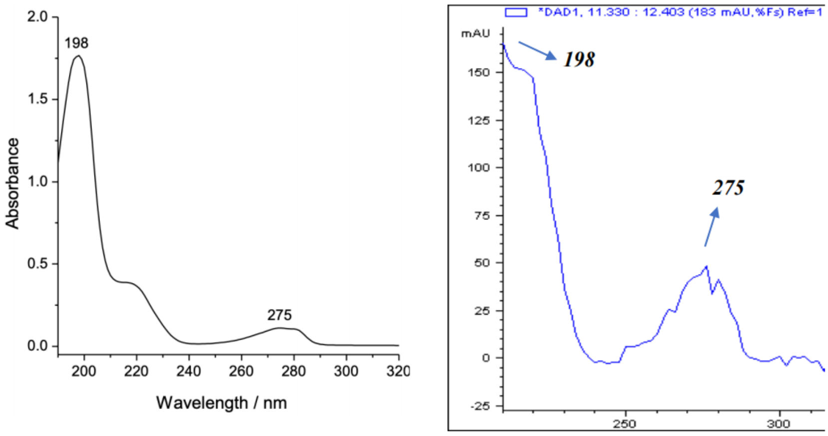

Figure 36 – (left): UV spectrum of Carvacrol in acetonitrile solution ($5*10^{-5}$ mol dm^{-3}) (Lopes Jesus, Et. Al., 2021); (right): Experimental UV spectrum of Carvacrol

Using the calibration curve, calculated with a standard OEO solution in a range from 10 to 100 mg/L, the average amount of Carvacrol (μg) absorbed per cm^2 of film was determined.

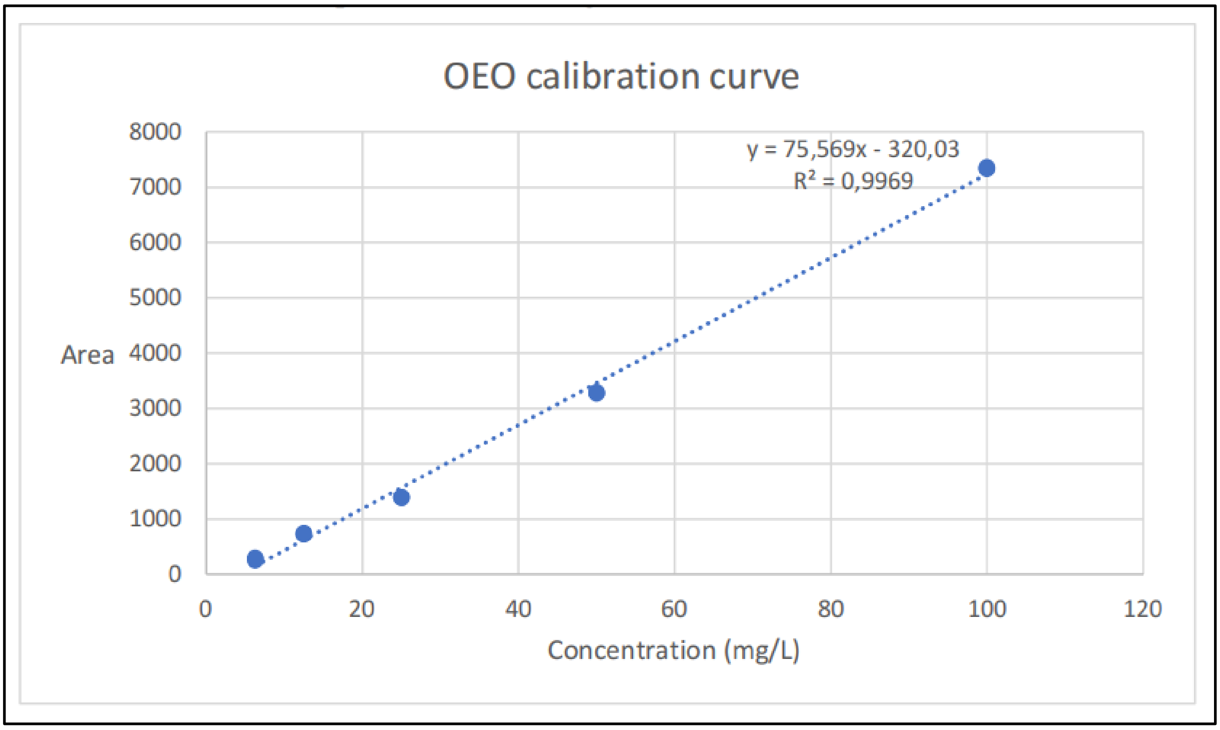

Figure 37- Calibration curve of OEO

From the experiments involving CMF_OEO, after 24 hours and 72 hours of contact between the fragments and 96% EtOH, which was used for the extraction to perform the analysis, it can be stated that: the average amount of this active component retained within a film is 11.9 μg/cm^2 (± 1.3).

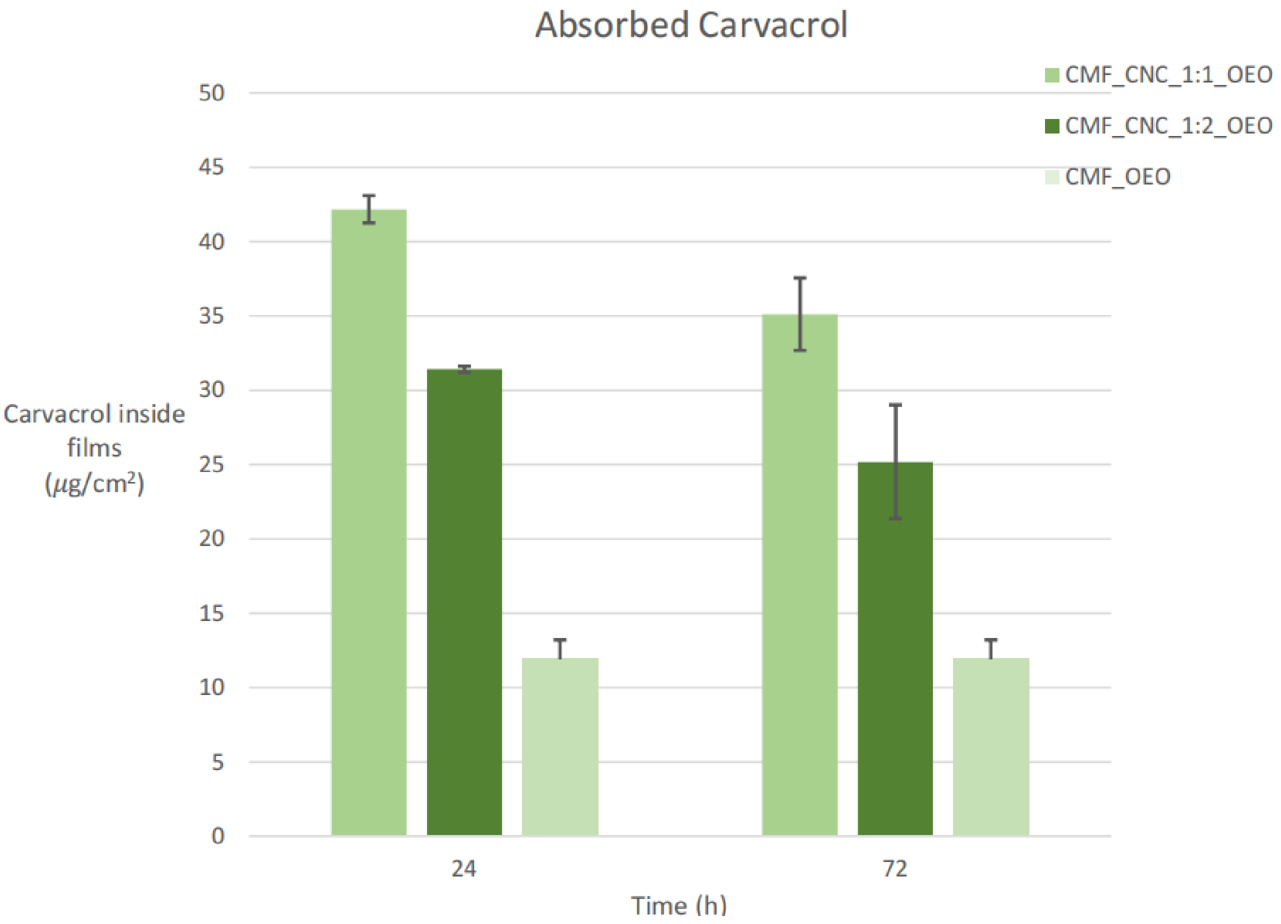

Figure 38- Histogram of the OEO absorption degree in the various samples

Since the same amount of oregano essential oil (OEO) was added to each polymeric matrix, the extraction tests show that: the CMF_OEO sample retains the least amount of essential oil, while the CMF_CNC_1:2_OEO sample absorbs more OEO compared to the previous preparation, and the CMF_CNC_1:1_OEO is the type that can retain the highest amount of essential oil.

The fact that the presence of CNC leads to an increase in the retention capacity of the matrix could be due to the arrangement of these nanocrystals between the CMF fibers.

Indeed, through physical interactions, CNC reduces the free volume present between the fibers, which is the main cause of OEO diffusion.

This behavior is confirmed by the literature (Mascheroni, et al., 2011), which states that the addition of nanoparticles improves the retention of active components, such as essential oils. However, as mentioned above, the CMF_CNC_1:2_OEO sample retains less oil than the CMF_CNC_1:1_OEO. Considering that the amount of nanocrystals in the CMF_CNC_1:2_OEO sample is double that in CMF_CNC_1:1_OEO, this particular result can be explained by the possible formation of CNC aggregates (Isogai, et al., 2011), which have larger dimensions than the nanocrystals contained in CMF_CNC_1:1_OEO. Consequently, this could lead to an increase in free volume, and thus, easier diffusion of the OEO.

4.3. Results obtained from the characterizations of ascorbic acid-added samples

Chemical analysis

HPLC-UV-DAD analyses were also performed on the samples doped with Vitamin C. The analyses were conducted on both control samples and doped samples that were in contact with a simulant to observe the possible migration of ascorbic acid over a period of 1 day, 2 days, and 7 days. After extraction, the samples were analyzed. The chromatogram results were processed through a quantitative analysis based on a calibration curve. The calibration curve, shown in Fig. 39, was obtained using a standard ascorbic acid solution at different concentrations in a range from 10 to 100 mg/L.

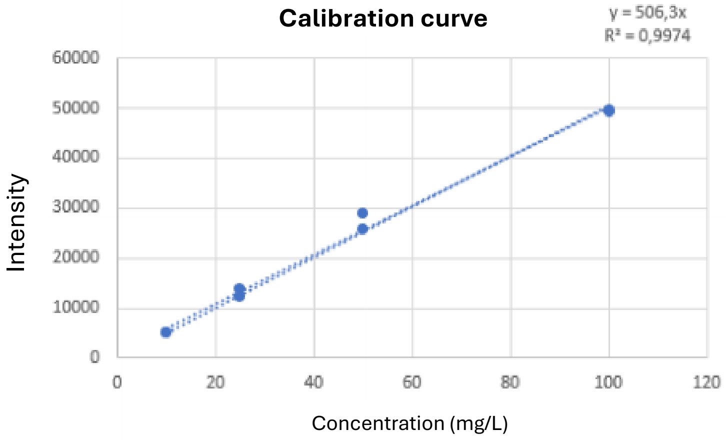

Figure 39- Ascorbic acid calibration curve

The areas of the chromatographic peaks were calculated, and then a histogram was constructed, showing that the concentration of ascorbic acid (in mg/L) in the films decreases as the contact time with the simulant increases, suggesting that there is migration of this molecule from the cellulosic film to the simulant.

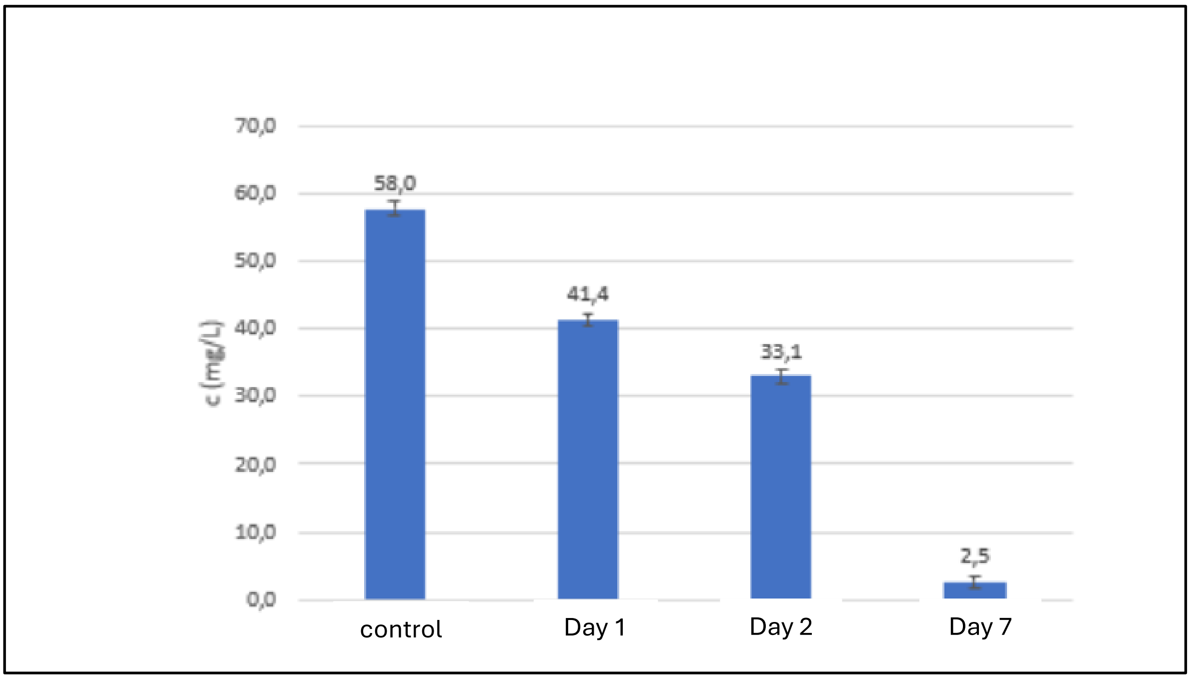

Figure 40- Histogram of the Ascorbic Acid absorption trend

The study on the integration and qualitative and quantitative evaluation of antioxidants in biodegradable films has proven to be very effective. In fact, it offers a promising outlook for the production of active packaging using exclusively biodegradable materials. This type of research is crucial for the development of sustainable solutions, as it enhances the protective properties of biodegradable films without compromising their biodegradability, thus helping to reduce the environmental impact of materials used in packaging.

5. Conclusions

In conclusion blends based on chitosan and crystalline nanocellulose (CNC) proved to be particularly promising due to their significant oxygen and water vapor barrier properties and good hydrophobicity. These blends combine the favorable characteristics of both polymers, with chitosan providing good hydrophobicity and CNC enhancing the material's rigidity and stability. Moreover, the good affinity between the two polymers lies in their ability to interact effectively at the molecular level. Chitosan, being a polysaccharide with free amine groups, can form hydrogen bonds and electrostatic interactions with CNC, another polysaccharide with hydroxyl groups. This affinity allows for a good blend and homogeneity between the two materials.

Moreover, the doped films have proven promising for their effectiveness in retaining active substances, which are incorporated into the crystalline nanocellulose (CNC) and remain anchored there. This is a very positive aspect, as it means that the active substances are not prematurely released during the use of the film, ensuring more efficient and long-lasting control over their activity.

CNC's ability to incorporate and retain active substances not only optimizes the functionality of the packaging but also contributes to improving the sustainability of the final product by reducing the use of non-biodegradable plastics.

These results open the way for future applications of these materials in the sustainable packaging sector, where it is essential to find solutions that combine product protection with a low environmental impact. The synergy between CNC and active substances in doped films represents a significant advancement in the research and development of new eco-friendly and functional materials, designed to meet the growing sustainability needs in the industrial sector.

Chapter 3

COATING ON PAPER SUBSTRATES USING BIO BASED MATERIALS

1. Abstract

The third part of this research focused on the development of polysaccharide-based coatings aimed at enhancing the barrier properties of lignocellulosic materials, particularly paper. The goal was to achieve uniform coatings using spin-coating and slot-die coating techniques. The combination of cellulose nanocrystals (CNC) and cellulose nanofibrils, both in their native and surface-modified forms (CNF, CMF), combined with polysaccharides such as chitosan, starch, pectin, and alginate, has been thoroughly studied for its potential as high-performance barrier coatings, due to its strong interaction with oxygen molecules. Spin coating is a technique in which a small amount of polysaccharide solution is spread on the paper surface, which is then rapidly rotated to ensure even coverage across the entire surface. This method is typically used in laboratories for preliminary studies. Slot-die coating, on the other hand, is a method that uses a thin-film deposition head to apply a polysaccharide-based solution onto the paper. This technique was employed to create thicker and more uniform coatings on larger paper surfaces, making it suitable for industrial or pilot plant applications. Part of the research, specifically related to slot-die coating, was carried out at the Mechanical Engineering Laboratory at the University of Maribor, under the supervision of Professor Vanja Kokol. I spent six months there, initially focusing on optimizing the process parameters and later applying bio-based coatings to paper. This work resulted in the publication of the article titled "Slot-die coating of cellulose nanocrystals and chitosan for improved barrier properties of paper" (Ruberto et al., 2024).

2. Experimental

2.1. Materials

The solvents used were: Distilled water, alcohol vinegar (brillaceto). The reagents used were: Cellulose nanocrystals (CelluForce NCC®; production no. 2015-011) purchased from CelluForce (Canada); TEMPO-oxidized cellulose (3%) produced in our laboratory; high molecular weight chitosan (290 - 320 kDa) (Sigma-Aldrich); vegetable glycerol with purity > 99% (Farmalabor).

2.2. Bio-based coatings formulation and paper substrates used

Bio-based coatings

The coatings were formulated using CNC and chitosan. The polysaccharides were weighed and then mixed with the solvents in a beaker. The solutions were mechanically stirred overnight. A 20% by weight plasticizer was added to the suspensions to improve their viscosity. The pH of the suspensions was measured and adjusted in the case of chitosan, increased with the addition of NaOH to prevent possible acid hydrolysis of the cellulose fibers and acid-induced paper aging. The compositions of the solutions used for the coating are listed in table 19.

Table 19- Suspensions used for coating paper substrates

Suspension	Solvent	Temperature (˚C)	Plasticizer Glicerole (%P/P)	Polysaccharides (%)	pH
Chitosan	Water/acetic acidi (90:10)	RT	2.5	2	5
CNC	Water	RT	2.5	11	5
CNC+Cht	Water	RT	2.5	6	5

Substrates used

The substrates used for coating deposition are paper (non-pretreated) (44±2 g/m², 65±2 μm) and pigment-pretreated paper (hot-pressed formulation containing $CaCO_3$ particles, starch as a binder, and carboxymethyl cellulose as a co-binder) (51±2 g/m², 78±3 μm). The papers were produced by Papirnica Vevče d.o.o. (Slovenia).

Deposition of coatings

Deposition by spin coating

To optimize the deposition process, several preliminary tests were conducted on Whatman filter paper (Tab. 20). These tests were essential for correctly setting the deposition parameters, in terms of speed, time, deposition method (static/dynamic) and the amount of solution deposited.

Table 20- Parameter optimization tests

Test	Suspensions	Velocity (rpm · s)	Deposition method	Amount of suspension (mL)
1	Cht 2%	1300/1950·18 1800/2200·18 1900/2880·18	Static	2 mL
2	Cht 2%	1300/1950·18 1800/2200·18 1900/2880·18	dynamic	3 mL
3	CNC 11%	1300/1950·18 1800/2200·18 1900/2880·18	Static	2 mL
4	CNC 11%	1300/1950·18 1800/2200·18 1900/2880·18	dynamic	3 mL
5	CNC+Cht 6,5%	1300/1950·18 1800/2200·18 1900/2880·18	Static	2 mL
6	CNC+Cht 6,5%	1300/1950·18 1800/2200·18 1900/2880·18	dynamic	3 mL

Following the preliminary tests and analyzing the results obtained, depositions were made on the Paper 44 and 51 substrates. Table 21 shows the deposition conditions used, and Figure 41 shows the equipment used for the depositions.

Table 21- Deposition conditions used for the Paper 44 and Paper 51

Substrate	suspension	Velocity	suspension volume
44- 51	Cht2% CNC11 CNC/Cht6,5%	1300/1950·18 1800/2200·18 1900/2880·18	2 mL
44-51	Cht2% CNC11 CNC/Cht6,5%	1300/1950·18 1800/2200·18 1900/2880·18	2 mL

Figure 41- Image of the Spin Coating in the SCVSA department

Deposition by slot-die coating

To optimize the deposition process and achieve high-quality results, several preliminary tests were required to establish the ideal operational parameters. In particular, it was essential to fine-tune the injection rate, coating speed, shim thickness, and gap distance, as these factors directly influence the quality, uniformity, and precision of the deposited film.

The injection rate controls the amount of material applied, while the coating speed impacts the distribution and uniformity of the film on the substrate surface. The shim thickness governs the distance between the coating head and the substrate, which in turn affects the thickness of the film, while the gap distance significantly influences the material flow during deposition.

All these parameters had to be carefully optimized through preliminary testing, as even slight changes could lead to coating defects, such as streaks or inconsistencies in thickness. It was only after adjusting these parameters that a stable and reproducible deposition process was achieved, producing uniform and high-quality films.

Figure 42 presents the Slot-Die Coating system. On the left, we can see the photo of the equipment in the mechanical engineering laboratory at the University of Maribor. On the right, the system and some of the key parameters used during deposition."

Additionally, two-layer deposition tests were conducted to assess the performance further.

Figure 42- Slot-die coating system of the University of Maribor

3. Methods

3.1. Measurement of suspension viscosity

The viscosity of the suspensions was measured using an NDJ-8S Digital Rotational Viscometer with a measurement range from 10 mPa·s to 2,000,000 mPa·s. The device is equipped with a backlit ultra-bright LCD display that allows for clear viewing of the test data.

Measurement range: 10 mPa·s～2,000,000 mPa·s

Spindles: No.1～No.4, a total of four spindles

Rotational speeds: 0.3 RPM, 0.6 RPM, 1.5 RPM, 3 RPM, 6 RPM, 12 RPM, 30 RPM, and 60 RPM, a total of 8 speeds

Measurement accuracy: ±3% (F·S)

Power supply: AC 220 V±10%, 50 Hz±10%; or AC 110V, 60Hz

Ambient temperature: 5 ℃～35 ℃

3.2. *Fourier Transform Infrared Spectroscopy (FTIR)*

The FTIR spectra of both the uncoated and coated paper samples were recorded using a Spectrum One FTIR spectrometer (Perkin-Elmer Inc., USA), equipped with a Golden Gate ATR attachment and a diamond crystal. Measurements were carried out under ambient conditions, with 16 scans collected at a resolution of 4 cm^{-1} over a wavelength range of 4000 to 600 cm^{-1}, and the air spectrum was subtracted as the background. FTIR mapping of the surface of selected samples was performed in a 2×2 mm area with 100 measurement points, each measuring 100×100 μm, and a depth of 6.5 μm, to analyze the spatial distribution of components using the Spotlight 200i Spectrum3 FTIR microscope (Perkin-Elmer Inc., USA). The data were processed using Spectrum 5.0.2/10 software. All measurements were repeated in duplicate.

3.3. Scanning electron microscopy (SEM) imaging

All samples were analyzed using scanning electron microscopy (SEM). The samples coated using the Spin Coating technique were examined in collaboration with the Materials Science and Technology research group from the Department of Systems and Industrial Technologies Engineering at the University of Parma, utilizing a Nova NanoSEM 450 – FEI Scanning Electron Microscope (SEM). For the samples coated using the Slot-Die Coating method, high-resolution images of both uncoated and variously coated paper samples were captured with a FEG SEM JSM IT800 SHL (JEOL Ltd., USA) microscope, available at the Mechanical Engineering Laboratory of the University of Maribor.

3.4. Grammage, thickness, density, and coating weight

In accordance with the ASTM D646-96 standard, 4 to 6 samples of both uncoated and coated papers were cut into 1 cm^2 squares (1 cm x 1 cm), conditioned at 23±2 °C and 65±2% relative humidity for a minimum of 24 hours, and weighed using an analytical balance (AE 240 Analytical Balance, Mettler Toledo). The grammage (G, g/m^2) was calculated using the formula M/A, where M is the weight of the paper sample in grams and A is the area in square meters. Thickness measurements were taken using a Kafer Prec 0.001 mm F 1000/30 micrometer (Käfer Messuhrenfabrik GmbH & Co. KG, Germany), and the density (ϱV, g/cm^3) was determined accordingly. The results presented are the arithmetic mean of 4 to 6 independent measurements, along with the corresponding standard deviations. The coating weight (g/m^2) was calculated theoretically, based on the total coating mass applied (CNC and Cht, including sorbitol) to the application area.

3.5. Air fow rate and permeability

The air flow rate (q, mL/min) was measured at 23±2 °C and 65±2% relative humidity using a Bendtsen air permeability tester (Rycobel, Belgium) in accordance with ISO 5636-3:2014, applying a pressure of 1.47 kPa at the measurement head. The reported values are the arithmetic means and standard deviations of at least ten independent measurements. The air permeability (AP, nm/Pa s) was calculated using the formula: $P = 0.0113 \times q$, where q denotes the average air flow rate passing through the test area of 1000 mm^2 at the specified pressure.

3.6. Surface contact angle

The contact angle analyses were performed using the same equipment and parameters described in Chapter 2, Section 3, Subsection 3.2.

3.7. Water vapour transmission rate (WVTR) and permeability (WVP)

The water vapour transmission rate (WVTR, $g/m^2 \cdot d$) was measured in duplicate at 23±2 °C and 50±5% relative humidity, following the ASTM F1249 Standard, using an Extra solution MultiPerm 050 instrument (PermTech srl, Italy). The surface area analyzed was 2.01 cm^2. The water vapour permeability (WVP, g $mm/m^2 \cdot d$ Pa) was subsequently calculated from the WVTR values using the equation: $WVP = WVTR \times l/\Delta p$, where l represents the thickness of the coated paper, and Δp is the partial water vapour pressure difference between the two sides of the paper (21.1 mmHg*0.85).

3.8. Oxygen transmission rate (OTR) and permeability (OP)

The oxygen transmission rate (OTR, $cm^3/m^2 \cdot d$) was measured on a surface area of 7.069 cm^2 at 23±1 °C and 50±2% relative humidity, using the Oxygen Transmission Rate System PERME® OX2/230 (Labthink Instruments Co., Ltd, China), following the ASTM D3985 Standard. The reported values are the average results from 2–3 measurements, with an oxygen flux rate of 10 mL/min and a pressure of 80 kPa. The upper limit of the OTR tester used is approximately 65,000 $cm^3/m^2 \cdot d$. The oxygen permeability (OP, cm^3 $mm/m^2 \cdot d \cdot kPa$) was calculated based on the thickness of the coated paper.

3.9. CIE whiteness and CIELAB colour measurement

The color of both coated and uncoated paper surfaces was measured using a CIE-Lab* system with a portable spectro-densitometer, Spectrodens B110040 (Techkon GmbH, Germany). The measurements included the L* value (ranging from 0 for darkness to 100 for lightness), the a* value (where negative values indicate greenness and positive values indicate redness), and the b* value (where negative values indicate blueness and positive values indicate yellowness). Additionally, the whiteness index was determined in accordance with UNI-EN 15866:2010, using a D65 illuminant.

4. Results and discussion

4.1. Results of the coating tests with Spin Coating

Viscosity of the suspensions

The table shows the viscosities measured for the suspensions used as coating for deposition.

Table 22- Viscosity of the suspensions

Suspension/solution	**Viscosity (dPas)**
CNC 11 Wt%	50±2
Cht 2Wt%	52±1
CNC+Cht 6,5 Wt%	25±1

Coating efficiency and correlation with the decrease in air permeability

To assess the efficiency of the coating process, the thicknesses of Paper44 and Paper51 substrates were measured before and after coating using a precision micrometer. As shown in the graphs in Fig. 43, all Paper44 substrates displayed an increase in thickness after coating. Additionally, substrates coated with 2 mL of any suspension exhibited a greater thickness increase compared to those coated with 3 mL, likely due to the stronger cohesive forces between the particles in suspension, which hindered adhesion to the paper substrate. The greatest thickness increase for Paper44 (38%) was observed when it was coated with 2 mL of a 11% CNC suspension at 1300/1950 rpm.

An unexpected observation was that the coatings did not adhere to the pretreated Paper51 substrates. The thickness variation measurements for all suspensions used yielded unsatisfactory results. This can be explained by the pretreatment of the Paper51 substrates, which likely inhibited the suspension from adhering to the paper surface. For instance, Fig. 44 shows a graph of the percentage thickness variation for Paper51 substrates treated with chitosan, where the thickness changes are even negative (suggesting measurement errors). Consequently, further characterizations were performed using the Paper44 substrates.

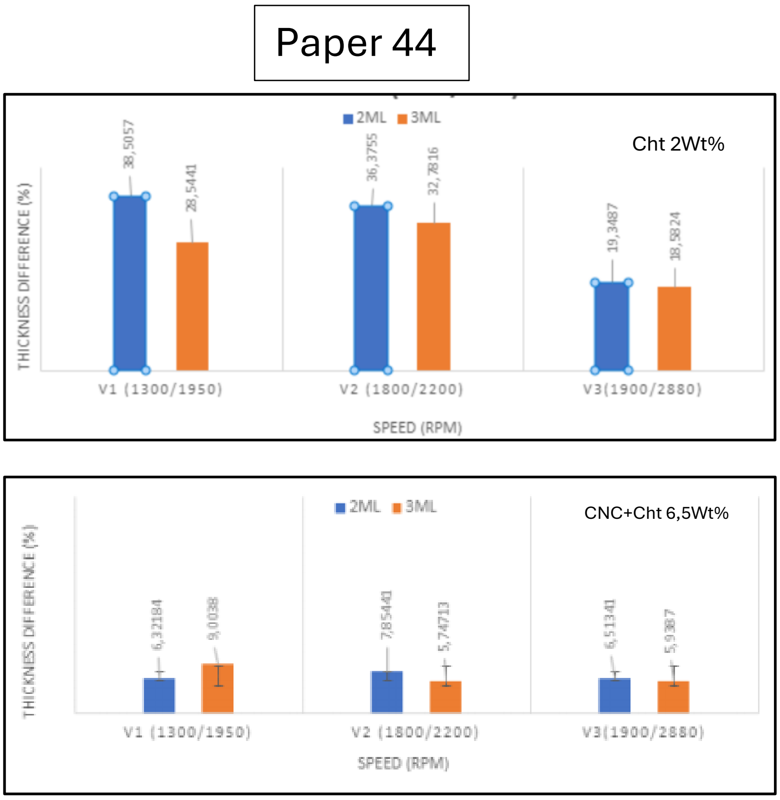

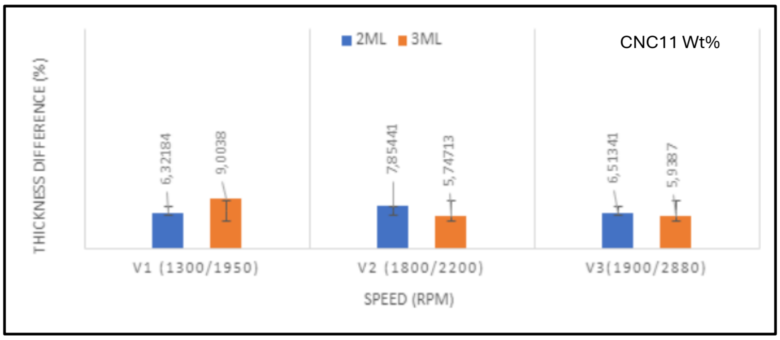

Figure 43- Results of the paper thickness measurements 44

Paper 51

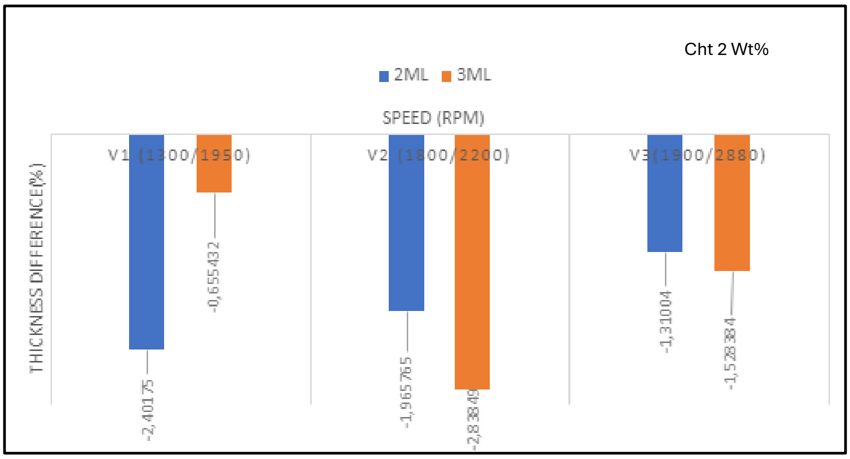

Figure 44- Results of the paper thickness measurements 51

The results observed through thickness measurements are consistent with the permeability measurements. For all the coated substrates, a decrease in air permeability was recorded. The values went from being unmeasurable for the control papers to excellent permeability values, with the best result obtained for the paper coated with the 11%Wt CNC mixture.

Table 23- Air permeability measurements

Solution	Air permeability [mL/min]
Control sample	/
CNC 11 Wt%	5.35±0.5
CNC+Cht 6 Wt %	90±3.3
Chitosan2 Wt %	78.5±1.5

Fourier Transform Infrared Spectroscopy (FTIR)

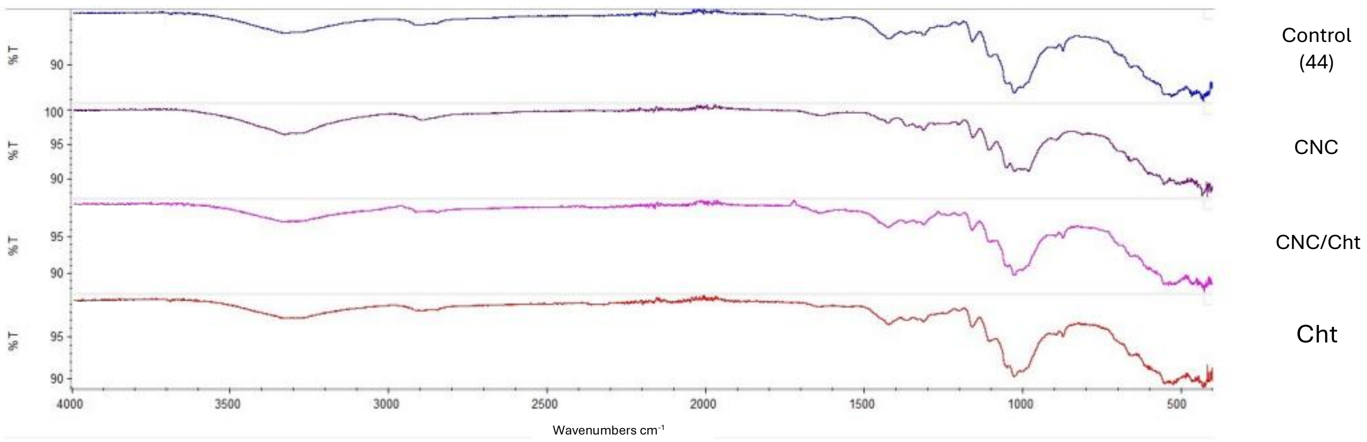

Figure 45- FT-IR spectra of the Paper 44 samples

As shown in Fig. 45, the IR spectra of the Paper44 substrates are quite similar due to the dominant presence of the cellulose matrix. However, some differences are noticeable across the spectra, which are summarized as follows:

- A weak signal at 874 cm^{-1} is present in all the samples, except for the one treated with the 11% CNC-based suspension. This band is associated with the amorphous component of cellulose, suggesting that it is less pronounced in the sample enhanced with crystalline nanocellulose from the coating.

- For the sample treated with the Cht-based suspension, a low-intensity band at 1554 cm^{-1} is observed, which is attributed to the bending vibration of the N-H bond of chitosan.

Scanning electron microscopy (SEM) imaging

All the samples were analyzed using scanning electron microscopy. The treated papers exhibit a smoother surface compared to the control paper, which clearly shows a three-dimensional network formed by cellulose fibers (Fig. 46). The papers treated with the chitosan-based suspension have an even smoother surface than those treated with CNC and CNC+Cht suspensions, likely because chitosan fills the pores of the paper's three-dimensional fiber network. On the other hand, the CNC and CNC + Cht suspensions appear to adhere to the substrates uniformly and continuously, following the alignment and length of the paper fibers.

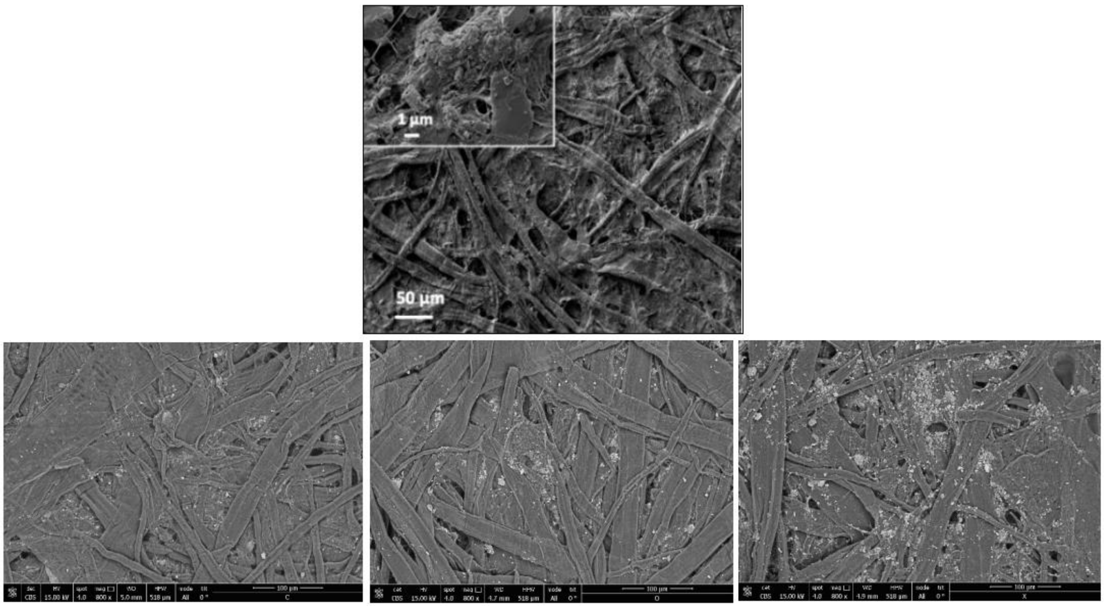

Cht 2Wt% CNC+Cht 6Wt% CNC 11Wt%

Figure 46- SEM analysis on the coated papers

Permeability measurements

To evaluate the water permeability properties of the samples before and after treatment, the water vapor transmission rate (WVTR) was measured. The results revealed that, in contrast to the control samples, where the permeability was too high to be measured, the Paper 44 samples treated with 11% CNC and CNC+Cht 6.5% exhibited notable improvements. The WVTR value increased from "non-measurable" in the control samples to 136 g/m²d and 65 g/m²d for the 11% CNC and 6.5% CNC+Cht treated samples, respectively. Even the Paper 44 sample treated with the 2% Cht suspension showed a measurable WVTR value of 79 g/m²d. However, unlike the WVTR measurements, the oxygen transmission rate (OTR) results from the spin-coated samples were unsatisfactory and did not yield significant findings.

Table 24- Water vapour (WVP) and oxygen (OP) permeabilities of differently coated papers

SAMPLE	**sample surface [cm^2]**	**Carrier flow [ml/min]**	**OP* [cm^3 mm/ m^2 d atm]**	**WVP** [g mm/ m^2 d kPa]**
CNC11Wt%	50	11.6	Non measurable	136.02± 0.01
CNC+Cht 6,5Wt%	50	11.6	Non measurable	65.60± 0.2
Chitosan2Wt%	50	11.6	Non measurable	79.00± 0.6

Surface contact angle

This section presents the results of the contact angle measurements performed on the Paper44 sheets before and after the coating deposition. The untreated substrates are completely hydrophilic, and the drop is immediately absorbed by the paper (Fig. 47).

The contact angle analyses performed on the papers treated with the 11Wt% CNC suspension also yielded contact angle values lower than 90°, highlighting the hydrophilic nature of the cellulose nanocrystals.

The results for the papers coated with the CNC+Cht 6Wt% and Cht 2Wt% suspensions are more promising, especially for the papers coated with Cht 2Wt%, which show a contact angle higher than 90° (Fig. 48).

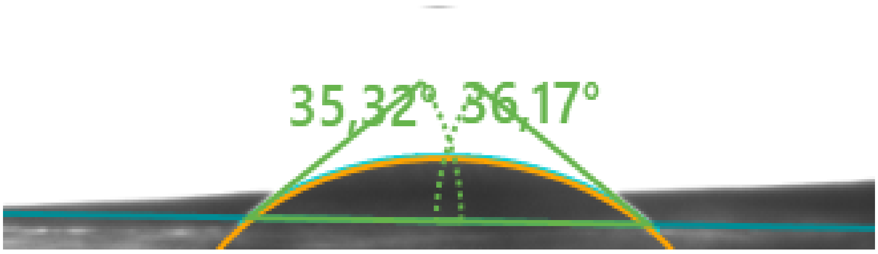

Figure 47- Example of contact angle for the papar coated with the CNC 11 Wt% suspension

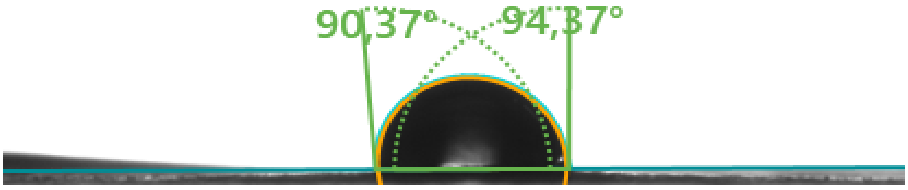

Figure 48- Example of contact angle for the paper coated with the CNC 2 Wt% suspension

4.2. Results of the coating tests with Slot-Die Coating

Coating efficiency and correlation with the decrease in air permeability.

Figure 49 ((a) for Paper 44; (b) for Paper 51) presents the results of Slot-Die Coating tests, showing the relationship between the increase in thickness of the coated substrates and the reduction in air permeability, based on adjustments to the coating parameters.

For Paper 44 (Fig. 49a), the thickness increased slightly with higher injection speeds, directly corresponding to a rise in dry thickness (5, 7, 10, and 15 μm) and the applied coating weight after drying. The most significant thickness change occurred with the CNC+Cht (6.5 wt%) mixture, where the thickness increase compared to the control ranged from 27.6% (with an injection speed of 19 mL/min and a 5 μm dry thickness) to 39.3% (with an injection speed of 38 mL/min and a 10 μm dry thickness), resulting in a 76.7% reduction in air flow rate.

For the highly concentrated CNC suspension (11 wt%), the air flow rate decreased by approximately 51.1% (from 51.8 to 25.3 mL/min), with a further reduction of about 99.8% (from 8.47 to 0.013 mL/min). Similarly, a coating of about 4 g/m² (2 wt%) Cht solution, achieved with a lower injection speed of 9.5 mL/min and a 10 μm dry thickness, resulted in a 3 mL/min air flow rate, demonstrating Cht's ability to form a uniform coating when proper parameters are used.

In the case of Paper 51 (Fig. 49b), the coating performance was similar, although the reduction in air permeability was more pronounced due to the paper's relatively higher permeability, likely from the porous $CaCO_3$ mineral particles. The air flow rate was reduced by approximately 97.8% (from 1724.2 to 37.6 mL/min), with a further 99% reduction (to 13.3 mL/min) after applying a 4 g/m² Cht coating. A 99.6% reduction in air flow rate (to 4.7–6.2 mL/min) was achieved with a 22 g/m² CNC coating (applied with an injection speed of 47.5 mL/min and a 10 μm dry thickness setting), and air permeability dropped below 1 mL/min for a 33 g/m² coating (applied with higher injection speeds of 57–85 mL/min and a 15 μm dry thickness setting).

The results also highlighted that a high-viscosity CNC suspension could be applied more uniformly at higher injection speeds (up to 80 mL/min, corresponding to a substrate speed of 2.4 m/min), compared to the Cht solution, which was limited to around 30 mL/min with the same shim width. This difference is attributed to the distinct surface tensions and visco-capillary forces of the two liquids, which influence their operational conditions and coating efficiency (Ding et al. 2016). Additionally, for both Paper 44 and Paper 51, the CNC coating on untreated paper (with a 20% thickness increase) was more superficial than on pre-treated paper (with a 15% thickness increase), even with the same 10 μm dry coating thickness and varying injection speeds. For both papers, a two-layer coating (22 g/m^2 of 11 wt% CNC, followed by 3 g/m^2 of 2 wt% Cht, resulting in a total coating weight of 24–25 g/m^2) made the paper almost impermeable to air. The air flow rates for these samples were reduced to about 0.01 mL/min for Paper 44 and 0.5 mL/min for Paper 51.

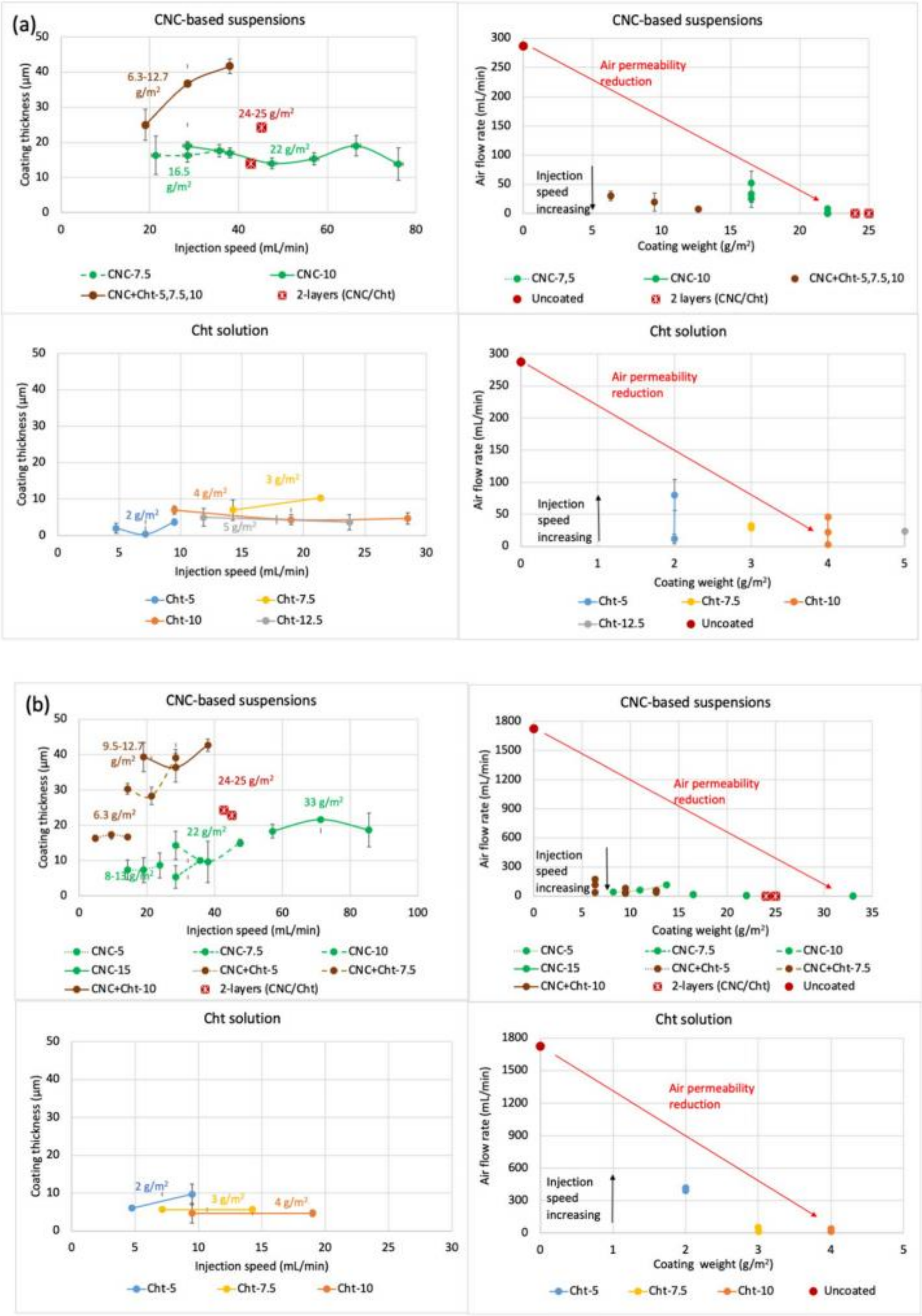

Figure 49 - Effect of slot-die coating of different CNC-based suspensions and CHT solution on increasing the coating weight (g/m²) and coating thickness (µm), and reducing the airflow rate (mL/min) for (a) plain and (b) pre-treated paper, depending on the coating parameter settings (i.e., injection speed 5–80 mL/min and dry thickness 5–12.5 µm) (Ruberto et al., 2024)

Fourier Transform Infrared Spectroscopy (FTIR)

Figure 50 ((a)for Paper 44 and (b) for Paper 51) presents the FTIR spectra for both uncoated papers and those coated with CNC, Cht, and a two-layer (CNC/Cht) coating, displayed for both the coated (top) and uncoated (bottom) sides. The spectra highlight the differences between the uncoated and coated papers, with the uncoated side showing no evidence of coating penetration. The spectra of uncoated papers and CNC-coated papers did not exhibit significant differences, except for a slight peak between 1311 and 1376 cm^{-1} for the CNC-coated papers, which can be attributed to the S=O band from the stretching vibrations of sulfate groups present in the CNC. This peak was diminished in the two-layer CNC/Cht coatings. A band around 1644 cm^{-1}, corresponding to the C=O vibration in the glucose ring of cellulose, was observed in all spectra and overlapped with the carbonyl stretching in amides, becoming more pronounced in the Cht-coated papers. Additionally, a band around 1561 cm^{-1}, attributed to the bending vibration of the N–H bond in amine groups, was present only in the Cht-coated papers (Zakaria et al. 2015).

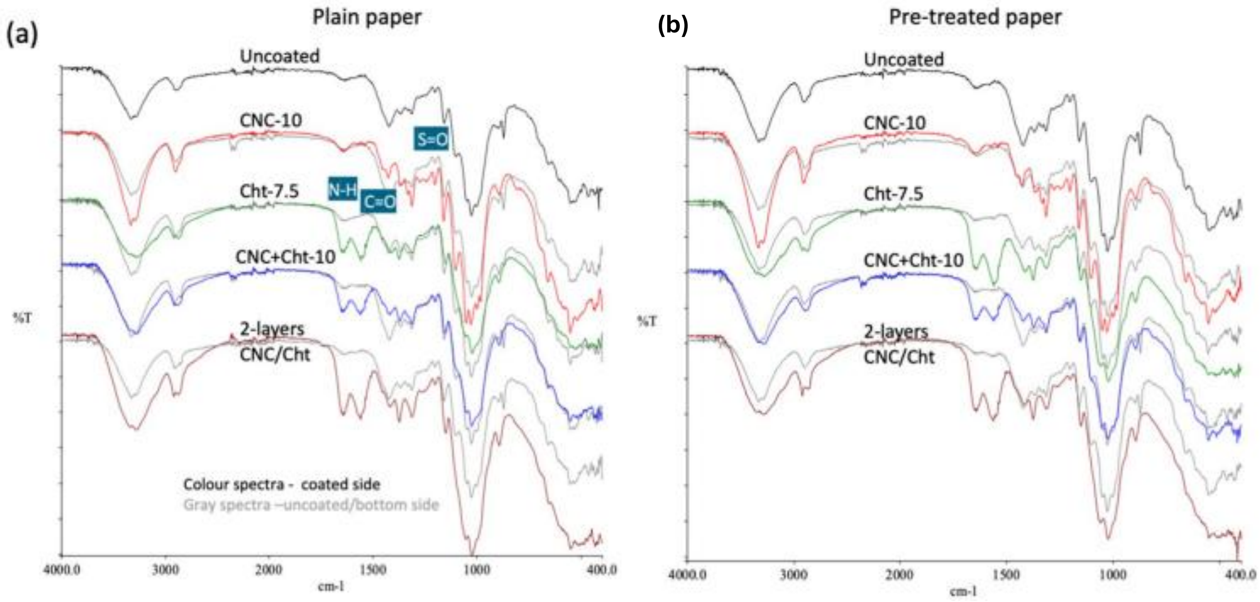

Figure 50 - (a) IR spectra of untreated paper 'paper 44', (b) IR spectra of pre-treated paper 'paper 51'(Ruberto et al.. 2024)

Scanning electron microscopy (SEM) imaging

Figure 51 provides a clear comparison of the surfaces of the papers before and after coating. The coated paper exhibits a noticeably smoother and more uniform surface than the uncoated ones. This change in surface morphology is due to the application of the coatings, which form a protective layer that fills in the paper's natural porosity and imperfections.

Uncoated papers generally have a rougher texture with more irregularities, resulting from the arrangement of visible cellulose fibers, which can be felt easily. In contrast, after applying the coatings, the surface becomes much smoother, indicating that the coatings enhance the material’s homogeneity and compactness. This effect is particularly prominent in the papers treated with CNC (cellulose nanocrystals) and the CNC + Cht (chitosan) mixture, which, due to their ability to form thin and even films, significantly reduce surface roughness.

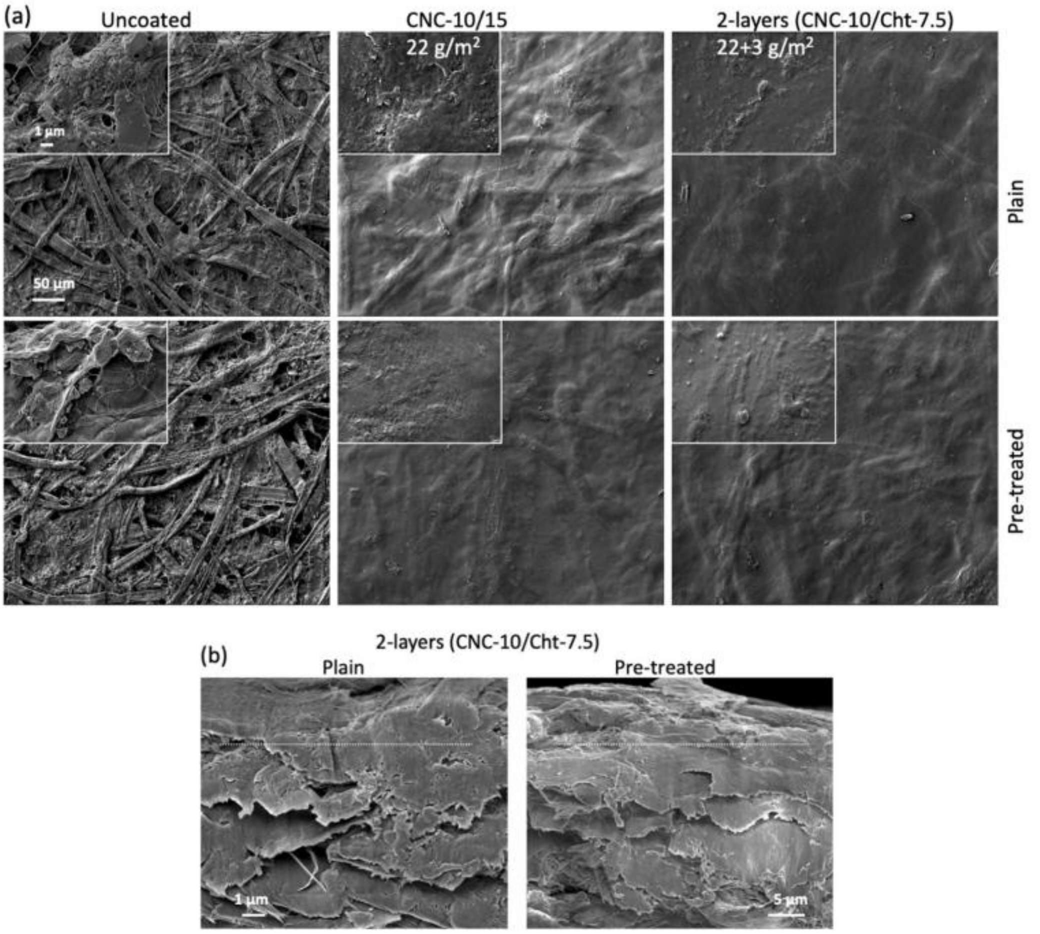

Figure 51- SEM images of the uncoated and differently coated papers: (a) surface and (b) cross-sections (Ruberto et al., 2024)

Whiteness, surface wettability, and water vapor permeability

For surface wettability and water properties, contact angle (CA) and water vapor transmission rate (WVTR) tests were conducted. Figure 52 illustrates the relationship between surface wettability (evaluated through contact angle measurement) and WVTR values for papers coated with various suspensions, showing a clear correlation with their moisture retention characteristics. Both uncoated Paper 44 and Paper 51 were found to be highly permeable to water vapor, causing the WVTR tests to fail. However, the contact angle (CA) of Paper 51 was notably higher (118°) compared to Paper 44 (85°), indicating a distinct hydrophilic nature of the surface that could influence the spreading, absorption, and adhesion of the CNC and Cht suspensions.

As a result, Paper 51 was expected to have higher suspension retention, leading to faster absorption of the water-rich suspensions/solutions and improved adhesion, which also impacted the WVTR values. For papers coated with the 11 wt% CNC suspension, the CA decreased to about 40°, and the WVTR dropped from unmeasurable values (for the uncoated Paper 51) to 136-128 g/m^{2}d, due to the high-water retention of the hydrophilic CNCs.

The Cht solution penetrated more deeply into the paper, slightly lowering the WVTR values (48-67 g/m^{2}d), with moderate hydrophobicity (increasing the CA to 102° for the uncoated paper with a maximum deposition of 5 g/m^2 and reducing it to 88° for the pre-treated paper). In contrast, the CNC-Cht mixture did not significantly affect any properties due to the formation of aggregates and their uneven distribution on the paper surface. Previous studies have indicated that up to three layers of Cht (with a coating weight of 13.7-20 g/m^2) were necessary to fully fill the paper's surface pores, saturating the paper matrix and reducing the WVTR to 49 g/m^{2}d by controlling interactions with water molecules (dos Santos et al., 2022; Bordenave et al., 2007). In contrast, the two-layer coatings resulted in a CA between 84-93° (associated with the hydrophobic nature of chitosan) and a WVTR of 68-70 g/m^{2}d, due to the controlled interactions with water molecules.

Both CNCs and Cht contributed to the reduction of air permeability, where the CNCs generated a highly hydrogen-bonded network with the paper, while electrostatic interaction with the Cht applied on top reduced the paper surface wettability and WVTR. The random orientation of the Cht polymer chains, their free volume, and swelling by water, reduced moisture permeation by absorbing vapor molecules (Trinh et al., 2023).

The whiteness measurement further confirmed the uniformity and homogeneity of the coatings. A slight reduction in lightness (L*), redness (a*), and yellowness (b*) was observed for the CNC-coated papers compared to the uncoated ones, while no changes were found for the Cht-coated papers. The average color values between the coated and uncoated papers for all samples were less than 3, a value that is not perceptible to the naked eye. Whiteness, on the other hand, increased significantly for the CNC-coated papers (up to 23% for a 20 µm thick coating of 22–33 g/m²; from 78 to 94 for the plain paper, and from 80 to 99 for the pre-treated paper), giving a glossy effect.

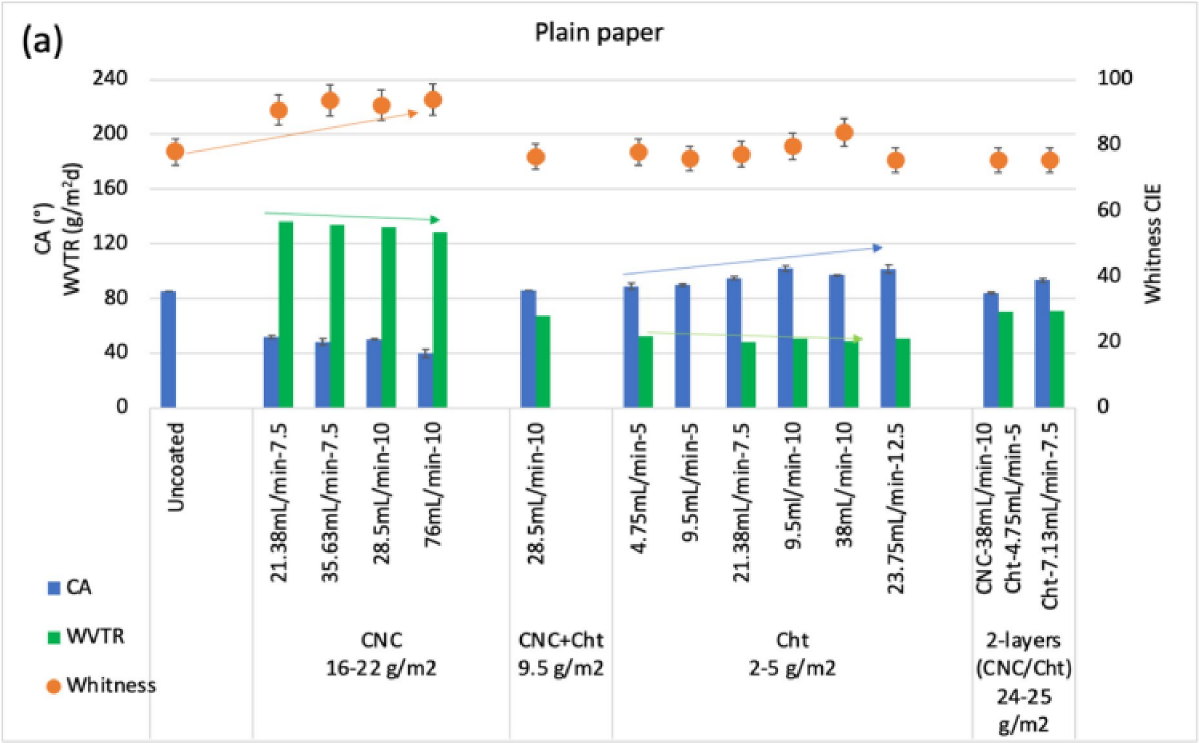

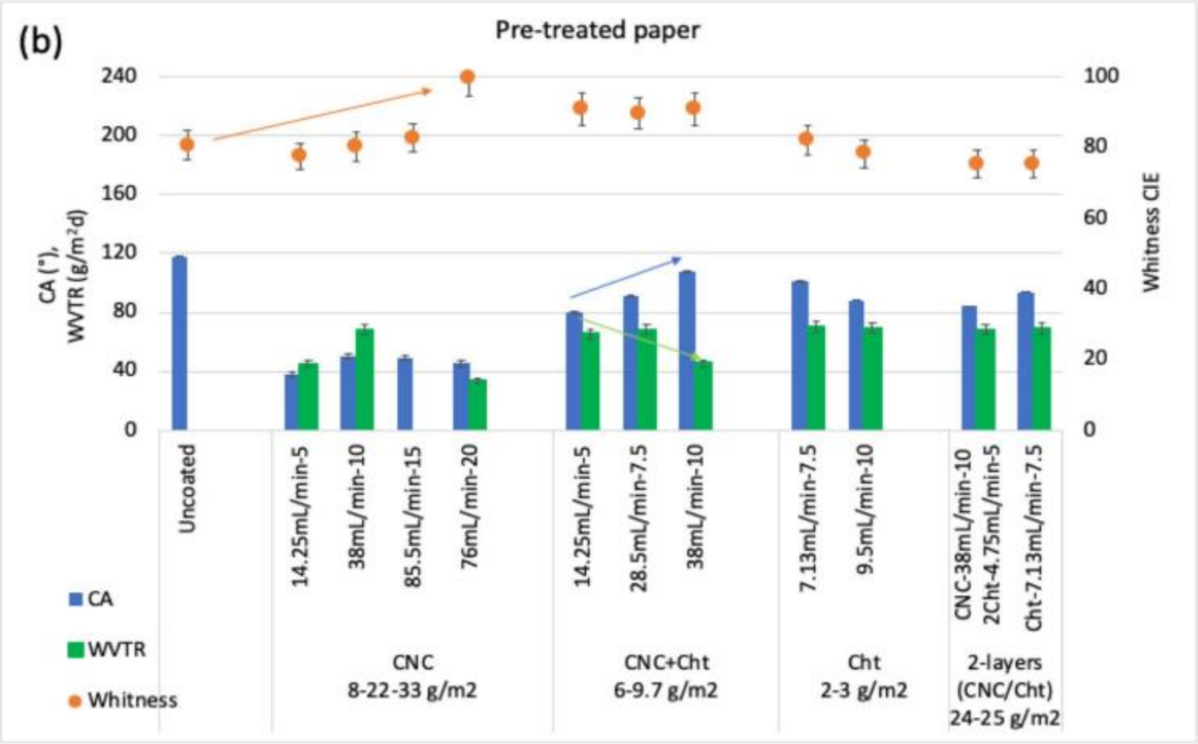

Figure 52- Whiteness, contact angle (CA), and water vapour transmission rate (WVTR) values for (a) uncoated and (b) pre-treated paper, depending on the coating parameters and applied coating weights (Ruberto et al., 2024)

Oxygen permeabilities

Coatings based on chitosan (Cht) and cellulose nanocrystals (CNC) greatly enhanced the oxygen and water vapor barrier properties of the papers. Specifically, the Cht coating (with a weight of 3-4 g/m²) resulted in a marked improvement in both air and oxygen permeability, making these values measurable (in contrast to the uncoated papers, which were too permeable to measure). The addition of CNC further boosted the oxygen barrier properties, owing to its crystalline structure and hydrogen bonding, which help reduce oxygen permeability. However, the effectiveness of CNC and Cht coatings also relies on various factors such as coating thickness and paper pre-treatment. For instance, CNC coatings led to a substantial reduction in oxygen permeability, with values even lower than those of common oxygen barrier materials like ethylene vinyl alcohol (EVOH) (Li et al., 2013).

Table 25- Water vapour (WVP), air (AP), and oxygen (OP) permeabilities of papers with different coatings (Ruberto et al., 2024)

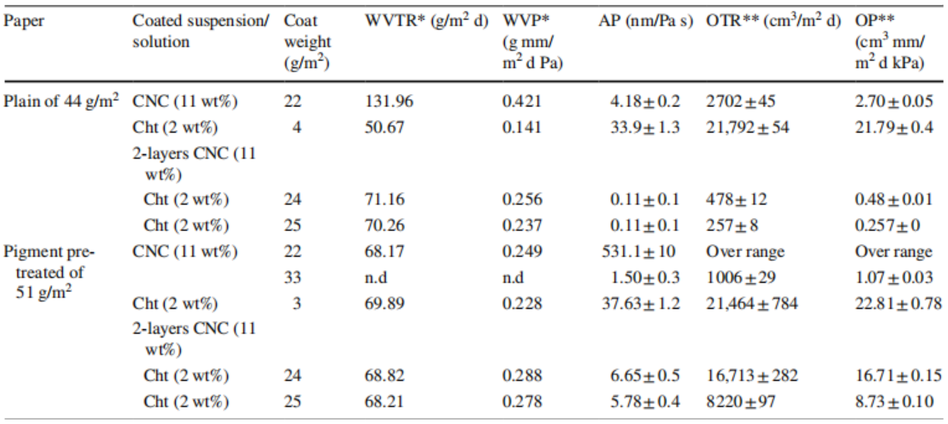

Paper	Coated suspension/ solution	Coat weight (g/m^2)	WVTR* (g/m^2 d)	WVP* (g mm/ m^2 d Pa)	AP (nm/Pa s)	OTR** (cm^3/m^2 d)	OP** (cm^3 mm/ m^2 d kPa)
Plain of 44 g/m^2	CNC (11 wt%)	22	131.96	0.421	4.18 ± 0.2	2702 ± 45	2.70 ± 0.05
	Cht (2 wt%)	4	50.67	0.141	33.9 ± 1.3	21,792 ± 54	21.79 ± 0.4
	2-layers CNC (11 wt%)						
	Cht (2 wt%)	24	71.16	0.256	0.11 ± 0.1	478 ± 12	0.48 ± 0.01
	Cht (2 wt%)	25	70.26	0.237	0.11 ± 0.1	257 ± 8	0.257 ± 0
Pigment pre-treated of 51 g/m^2	CNC (11 wt%)	22	68.17	0.249	531.1 ± 10	Over range	Over range
		33	n.d	n.d	1.50 ± 0.3	1006 ± 29	1.07 ± 0.03
	Cht (2 wt%)	3	69.89	0.228	37.63 ± 1.2	21,464 ± 784	22.81 ± 0.78
	2-layers CNC (11 wt%)						
	Cht (2 wt%)	24	68.82	0.288	6.65 ± 0.5	16,713 ± 282	16.71 ± 0.15
	Cht (2 wt%)	25	68.21	0.278	5.78 ± 0.4	8220 ± 97	8.73 ± 0.10

5. Conclusions

In conclusion, it can be stated that the *slot-die* coating proved to be more efficient compared to the spin-coating treatment, as it showed a significant reduction in oxygen and water vapor permeability, thus improving the barrier properties of the papers. This treatment led to greater uniformity in the coating distribution, contributing to a reduction in surface porosity and enhancing protection against external factors like humidity and oxygen, which can compromise the quality of packaged products.

The papers, after coating, exhibited good permeability values, meaning that the process had a positive effect on their ability to resist water vapor and oxygen transmission. The coating contributed to greater surface density and compactness, reducing permeation pathways and improving barrier properties, without compromising the material's functionality. This makes the treated papers more suitable for applications where protecting the contents from environmental factors is essential, such as in the packaging of food or pharmaceutical products.

Additionally, the use of the *slot-die* coating further improved the aesthetic appearance of the papers, giving them a glossy effect and enhancing their whiteness, which is also beneficial from a visual and commercial standpoint. Therefore, the combination of good oxygen and water vapor barrier properties, along with an aesthetic enhancement, makes the coated papers more competitive in various application sectors.

References

1. Abbasi Moud, A. (2022). Advanced cellulose nanocrystals (CNC) and cellulose nanofibrils (CNF) aerogels: Bottom-up assembly perspective for production of adsorbents. In *International Journal of Biological Macromolecules* (Vol. 222, pp. 1–29). Elsevier B.V. https://doi.org/10.1016/j.ijbiomac.2022.09.148
2. Agnihotri, S. A., Mallikarjuna, N. N., & Aminabhavi, T. M. (2004). Recent advances on chitosan-based micro- and nanoparticles in drug delivery. In *Journal of Controlled Release* (Vol. 100, Issue 1, pp. 5–28). https://doi.org/10.1016/j.jconrel.2004.08.010
3. Ahankari, S. S., Subhedar, A. R., Bhadauria, S. S., & Dufresne, A. (2021). Nanocellulose in food packaging: A review. In *Carbohydrate Polymers* (Vol. 255). Elsevier Ltd. https://doi.org/10.1016/j.carbpol.2020.117479
4. Ahmed-Haras, M. R., Kao, N., Islam, Md. S., & Ward, L. (2020). An Overview of Recent Developments in Hetero-Catalytic Conversion of Cellulosic Biomass. *Research Communication in Engineering Science & Technology*, *4*, 43–54. https://doi.org/10.22597/rcest.v4.65
5. Araki, J., Wada, M., Kuga, S., & Okano, T. (1998). Flow properties of microcrystalline cellulose suspension prepared by acid treatment of native cellulose. In *Colloids and Surfaces A: Physicochemical and Engineering Aspects* (Vol. 142).
6. Babaei-Ghazvini, A., Vafakish, B., Patel, R., Falua, K. J., Dunlop, M. J., & Acharya, B. (2024). Cellulose nanocrystals in the development of biodegradable materials: A review on CNC resources, modification, and their hybridization. In *International Journal of Biological Macromolecules* (Vol. 258). Elsevier B.V. https://doi.org/10.1016/j.ijbiomac.2023.128834
7. Bailey, W. F., Bobbitt, J. M., & Wiberg, K. B. (2007). Mechanism of the oxidation of alcohols by oxoammonium cations. *Journal of Organic Chemistry*, *72*(12), 4504–4509. https://doi.org/10.1021/jo0704614

8. Bellia, L., De Natale, A., Fragliasso, F., Graiff, C., Petraretti, M., Pollio, A., & Potenza, M. (2023). Chromatic alterations induced by preservation treatments on paper: The case of Ag-functionalized nanocrystalline cellulose. Journal of Cultural Heritage, 64, 120–131. https://doi.org/10.1016/j.culher.2023.09.008
9. Basile, R., Bergamonti, L., Fernandez, F., Graiff, C., Haghighi, A., Isca, C., Lottici, P. P., Pizzo, B., & Predieri, G. (2018). Bio-inspired consolidants derived from crystalline nanocellulose for decayed wood. Carbohydrate Polymers, 202, 164–171. https://doi.org/10.1016/j.carbpol.2018.08.132
10. Bergamonti, L., Potenza, M., Haghighi Poshtiri, A., Lorenzi, A., Sanangelantoni, A. M., Lazzarini, L., Lottici, P. P., & Graiff, C. (2020). Ag-functionalized nanocrystalline cellulose for paper preservation and strengthening. Carbohydrate Polymers, 231. https://doi.org/10.1016/j.carbpol.2019.115773
11. Cole, M., Lindeque, P., Halsband, C., & Galloway, T. S. (2011). Microplastics as contaminants in the marine environment: A review. In *Marine Pollution Bulletin* (Vol. 62, Issue 12, pp. 2588–2597). https://doi.org/10.1016/j.marpolbul.2011.09.025
12. Costa, S. M., Ferreira, D. P., Teixeira, P., Ballesteros, L. F., Teixeira, J. A., & Fangueiro, R. (2021a). Active natural-based films for food packaging applications: The combined effect of chitosan and nanocellulose. *International Journal of Biological Macromolecules*, *177*, 241–251. https://doi.org/10.1016/j.ijbiomac.2021.02.105
13. Costa, S. M., Ferreira, D. P., Teixeira, P., Ballesteros, L. F., Teixeira, J. A., & Fangueiro, R. (2021b). Active natural-based films for food packaging applications: The combined effect of chitosan and nanocellulose. *International Journal of Biological Macromolecules*, *177*, 241–251. https://doi.org/10.1016/j.ijbiomac.2021.02.105
14. Cazón, P., Velazquez, G., Ramírez, J. A., & Vázquez, M. (2017). Polysaccharide-based films and coatings for food packaging: A review. Food Hydrocolloids, 68, 136–148. https://doi.org/10.1016/j.foodhyd.2016.09.009

15. El-Araby, A., Janati, W., Ullah, R., Ercisli, S., & Errachidi, F. (2023). Chitosan, chitosan derivatives, and chitosan-based nanocomposites: eco-friendly materials for

advanced applications (a review). In *Frontiers in Chemistry* (Vol. 11). Frontiers Media SA. https://doi.org/10.3389/fchem.2023.1327426

16. Eyley, S., & Thielemans, W. (2014). Surface modification of cellulose nanocrystals. *Nanoscale*, *6*(14), 7764–7779. https://doi.org/10.1039/c4nr01756k
17. Grimaldi, M., Pitirollo, O., Ornaghi, P., Corradini, C., & Cavazza, A. (2022). Valorization of agro-industrial byproducts: Extraction and analytical characterization of valuable compounds for potential edible active packaging formulation. *Food Packaging and Shelf Life*, *33*. https://doi.org/10.1016/j.fpsl.2022.100900
18. Grząbka-Zasadzińska, A., Amietszajew, T., & Borysiak, S. (2017). Thermal and mechanical properties of chitosan nanocomposites with cellulose modified in ionic liquids. *Journal of Thermal Analysis and Calorimetry*, *130*(1), 143–154. https://doi.org/10.1007/s10973-017-6295-3
19. Habibi, Y. (2014). Key advances in the chemical modification of nanocelluloses. In *Chemical Society Reviews* (Vol. 43, Issue 5, pp. 1519–1542). Royal Society of Chemistry. https://doi.org/10.1039/c3cs60204d
20. Habibi, Y., Chanzy, H., & Vignon, M. R. (2006). TEMPO-mediated surface oxidation of cellulose whiskers. *Cellulose*, *13*(6), 679–687. https://doi.org/10.1007/s10570-006-9075-y
21. Habibi, Y., Lucia, L. A., & Rojas, O. J. (2010a). Cellulose nanocrystals: Chemistry, self-assembly, and applications. *Chemical Reviews*, *110*(6), 3479–3500. https://doi.org/10.1021/cr900339w
22. Habibi, Y., Lucia, L. A., & Rojas, O. J. (2010b). Cellulose nanocrystals: Chemistry, self-assembly, and applications. *Chemical Reviews*, *110*(6), 3479–3500. https://doi.org/10.1021/cr900339w
23. Herrera, M. A., Sirviö, J. A., Mathew, A. P., & Oksman, K. (2016). Environmental friendly and sustainable gas barrier on porous materials: Nanocellulose coatings prepared using spin- and dip-coating. *Materials and Design*, *93*, 19–25. https://doi.org/10.1016/j.matdes.2015.12.127

24. Hopewell, J., Dvorak, R., & Kosior, E. (2009). Plastics recycling: Challenges and opportunities. In *Philosophical Transactions of the Royal Society B: Biological Sciences* (Vol. 364, Issue 1526, pp. 2115–2126). Royal Society. https://doi.org/10.1098/rstb.2008.0311
25. Jiang, J., Zhu, Y., & Jiang, F. (2021). Sustainable isolation of nanocellulose from cellulose and lignocellulosic feedstocks: Recent progress and perspectives. *Carbohydrate Polymers*, *267*. https://doi.org/10.1016/j.carbpol.2021.118188
26. Kapoor, D. U., Sharma, H., Maheshwari, R., Pareek, A., Gaur, M., Prajapati, B. G., Castro, G. R., Thanawuth, K., Suttiruengwong, S., & Sriamornsak, P. (2024). Konjac glucomannan: A comprehensive review of its extraction, health benefits, and pharmaceutical applications. In *Carbohydrate Polymers* (Vol. 339). Elsevier Ltd. https://doi.org/10.1016/j.carbpol.2024.122266
27. Kato, Y., Matsuo, R., & Isogai, A. (n.d.). *Oxidation process of water-soluble starch in TEMPO-mediated system*. www.elsevier.com/locate/carbpol
28. Kean, T., & Thanou, M. (2010). Biodegradation, biodistribution and toxicity of chitosan. In *Advanced Drug Delivery Reviews* (Vol. 62, Issue 1, pp. 3–11). https://doi.org/10.1016/j.addr.2009.09.004
29. Klemm, D., Heublein, B., Fink, H. P., & Bohn, A. (2005a). Cellulose: Fascinating biopolymer and sustainable raw material. In *Angewandte Chemie - International Edition* (Vol. 44, Issue 22, pp. 3358–3393). https://doi.org/10.1002/anie.200460587
30. Klemm, D., Heublein, B., Fink, H. P., & Bohn, A. (2005b). Cellulose: Fascinating biopolymer and sustainable raw material. In *Angewandte Chemie - International Edition* (Vol. 44, Issue 22, pp. 3358–3393). https://doi.org/10.1002/anie.200460587
31. Kroon-Batenburg, L. M. J., & Kroon, J. (1997a). The crystal and molecular structures of cellulose I and II. In *Glycoconjugate Journal* (Vol. 14).
32. Kroon-Batenburg, L. M. J., & Kroon, J. (1997b). The crystal and molecular structures of cellulose I and II. In *Glycoconjugate Journal* (Vol. 14).

33. Kumar, M. N. V. R., Muzzarelli, R. A. A., Muzzarelli, C., Sashiwa, H., & Domb, A. J. (2004). Chitosan chemistry and pharmaceutical perspectives. *Chemical Reviews*, *104*(12), 6017–6084. https://doi.org/10.1021/cr030441b
34. Kusmono, Wildan, M. W., & Lubis, F. I. (2021). Fabrication and characterization of chitosan/cellulose nanocrystal/glycerol bio-composite films. *Polymers*, *13*(7). https://doi.org/10.3390/polym13071096
35. Lefebvre, J., & Gray, D. G. (2005). AFM of adsorbed polyelectrolytes on cellulose I surfaces spin-coated on silicon wafers. In *Cellulose* (Vol. 12, Issue 2, pp. 127–134). https://doi.org/10.1007/s10570-004-1574-0
36. Lu, P., & Hsieh, Y. Lo. (2010a). Preparation and properties of cellulose nanocrystals: Rods, spheres, and network. *Carbohydrate Polymers*, *82*(2), 329–336. https://doi.org/10.1016/j.carbpol.2010.04.073
37. Lu, P., & Hsieh, Y. Lo. (2010b). Preparation and properties of cellulose nanocrystals: Rods, spheres, and network. *Carbohydrate Polymers*, *82*(2), 329–336. https://doi.org/10.1016/j.carbpol.2010.04.073
38. Luo, X., Shen, J., Ma, Y., Liu, L., Meng, R., & Yao, J. (2020). Robust, sustainable cellulose composite aerogels with outstanding flame retardancy and thermal insulation. *Carbohydrate Polymers*, *230*. https://doi.org/10.1016/j.carbpol.2019.115623
39. Martins, J. T., Cerqueira, M. A., Souza, B. W. S., Carmo Avides, M. D. O., & Vicente, A. A. (2010). Shelf life extension of ricotta cheese using coatings of galactomannans from nonconventional sources incorporating nisin against listeria monocytogenes. *Journal of Agricultural and Food Chemistry*, *58*(3), 1884–1891. https://doi.org/10.1021/jf902774z
40. Mei, Z., Szczepanski, C. R., Montreuil, O., Kuzhir, P., & Godeau, G. (2024). Investigation on novel chitin and chitosan from dung beetle Heteronitis castelnaui (Harold, 1865) and its potential application for organic dyes removal from aqueous solution. *International Journal of Biological Macromolecules*, *280*. https://doi.org/10.1016/j.ijbiomac.2024.135605

41. Moon, R. J., Martini, A., Nairn, J., Simonsen, J., & Youngblood, J. (2011). Cellulose nanomaterials review: Structure, properties and nanocomposites. *Chemical Society Reviews*, *40*(7), 3941–3994. https://doi.org/10.1039/c0cs00108b
42. Nagarajan, D., Senthilkumar, G., Chen, C. W., Karmegam, N., Praburaman, L., Kim, W., & Dong, C. Di. (2024). Sustainable bioplastics from seaweed polysaccharides: A comprehensive review. In *Polymers for Advanced Technologies* (Vol. 35, Issue 8). John Wiley and Sons Ltd. https://doi.org/10.1002/pat.6536
43. Njus, D., Kelley, P. M., Tu, Y. J., & Schlegel, H. B. (2020). Ascorbic acid: The chemistry underlying its antioxidant properties. In *Free Radical Biology and Medicine* (Vol. 159, pp. 37–43). Elsevier Inc. https://doi.org/10.1016/j.freeradbiomed.2020.07.013
44. Perumal, A. B., Huang, L., Nambiar, R. B., He, Y., Li, X., & Sellamuthu, P. S. (2022). Application of essential oils in packaging films for the preservation of fruits and vegetables: A review. In *Food Chemistry* (Vol. 375). Elsevier Ltd. https://doi.org/10.1016/j.foodchem.2021.131810
45. PlascticsEurope. (n.d.). *Plastics-the Facts 2021 An analysis of European plastics production, demand and waste data*.
46. Potenza, M., Bergamonti, L., Lottici, P. P., Righi, L., Lazzarini, L., & Graiff, C. (2022). Green Extraction of Cellulose Nanocrystals of Polymorph II from Cynara scolymus L.: Challenge for a "Zero Waste" Economy. Crystals, 12(5). https://doi.org/10.3390/cryst12050672
47. Potier, M., Tea, L., Benyahia, L., Nicolaï, T., & Renou, F. (n.d.). Viscosity of Aqueous Polysaccharide Solutions and Selected Homogeneous Binary Mixtures. Macromolecules, 2020(23). https://doi.org/10.1021/acs.macromol.0c02157i
48. Priyadarshi, R., & Rhim, J. W. (2020). Chitosan-based biodegradable functional films for food packaging applications. In Innovative Food Science and Emerging Technologies (Vol. 62). Elsevier Ltd. https://doi.org/10.1016/j.ifset.2020.102346

49. Pylkkänen, R., Mohammadi, P., Arola, S., De Ruijter, J. C., Sunagawa, N., Igarashi, K., & Penttilä, M. (2020). In Vitro Synthesis and Self-Assembly of Cellulose II Nanofibrils Catalyzed by the Reverse Reaction of Clostridium thermocellum Cellodextrin Phosphorylase. *Biomacromolecules*, *21*(10), 4355–4364. https://doi.org/10.1021/acs.biomac.0c01162
50. Rinaudo, M. (2006). Chitin and chitosan: Properties and applications. In *Progress in Polymer Science (Oxford)* (Vol. 31, Issue 7, pp. 603–632). https://doi.org/10.1016/j.progpolymsci.2006.06.001
51. Rochman, C. M., Hoh, E., Kurobe, T., & Teh, S. J. (2013). Ingested plastic transfers hazardous chemicals to fish and induces hepatic stress. *Scientific Reports*, *3*. https://doi.org/10.1038/srep03263
52. Ruberto, Y., Vivod, V., Grkman, J. J., Lavrič, G., Graiff, C., & Kokol, V. (2024). Slot-die coating of cellulose nanocrystals and chitosan for improved barrier properties of paper. Cellulose, 31(6), 3589–3606. https://doi.org/10.1007/s10570-024-05847-3

53. Ruiz-Palomero, C., Soriano, M. L., & Valcárcel, M. (2015). β-Cyclodextrin decorated nanocellulose: A smart approach towards the selective fluorimetric determination of danofloxacin in milk samples. *Analyst*, *140*(10), 3431–3438. https://doi.org/10.1039/c4an01967a
54. Salim, M. H., Abdellaoui, Y., Ait Benhamou, A., Ablouh, E. H., El Achaby, M., & Kassab, Z. (2022). Influence of cellulose nanocrystals from pea pod waste on mechanical, thermal, biodegradability, and barrier properties of chitosan-based films. *Cellulose*, *29*(9), 5117–5135. https://doi.org/10.1007/s10570-022-04587-6
55. Savadekar, N. R., Karande, V. S., Vigneshwaran, N., Bharimalla, A. K., & Mhaske, S. T. (2012). Preparation of nano cellulose fibers and its application in kappa-carrageenan based film. *International Journal of Biological Macromolecules*, *51*(5), 1008–1013. https://doi.org/10.1016/j.ijbiomac.2012.08.014
56. Sharma, P., Sharma, S., Ramakrishna, G., Srivastava, H., & Gaikwad, K. (2021). A comprehensive review on leguminous galactomannans: structural analysis,

functional properties, biosynthesis process and industrial applications. In *Critical Reviews in Food Science and Nutrition* (Vol. 62, Issue 2, pp. 443–465). Taylor and Francis Ltd. https://doi.org/10.1080/10408398.2020.1819196

57. Sharma, S., Kumar, K., & Thakur, N. (2023). A comprehensive review on analysis of functionalization techniques and techno-innovative uses of nano-cellulosic materials. *Industrial Crops and Products*, *206*. https://doi.org/10.1016/j.indcrop.2023.117632
58. Shen, M., Huang, W., Chen, M., Song, B., Zeng, G., & Zhang, Y. (2020). (Micro)plastic crisis: Un-ignorable contribution to global greenhouse gas emissions and climate change. In *Journal of Cleaner Production* (Vol. 254). Elsevier Ltd. https://doi.org/10.1016/j.jclepro.2020.120138
59. Silva, A. C., Valle, A. B. C. dos S., Lemos, A. S. de O., Campos, L. M., Fabri, R. L., Costa, F. F., da Silva, J. G., Vilela, F. M. P., Tavares, G. D., Rodarte, M. P., & Denadai, Â. M. L. (2024). Development and characterization of chitosan film containing hydroethanolic extract of Coffea arabica leaves for wound dressing application. *Materials Today Communications*, *38*. https://doi.org/10.1016/j.mtcomm.2024.108503
60. Thompson, R. C., Moore, C. J., Saal, F. S. V., & Swan, S. H. (2009). Plastics, the environment and human health: Current consensus and future trends. In *Philosophical Transactions of the Royal Society B: Biological Sciences* (Vol. 364, Issue 1526, pp. 2153–2166). Royal Society. https://doi.org/10.1098/rstb.2009.0053
61. Trinh, B. M., Smith, M., & Mekonnen, T. H. (2022). A nanomaterial-stabilized starch-beeswax Pickering emulsion coating to extend produce shelf-life. *Chemical Engineering Journal*, *431*. https://doi.org/10.1016/j.cej.2021.133905
62. Verma, J., Petru, M., & Goel, S. (2024). Cellulose based materials to accelerate the transition towards sustainability. In *Industrial Crops and Products* (Vol. 210). Elsevier B.V. https://doi.org/10.1016/j.indcrop.2024.118078
63. Wang, R., Zhang, S., Liu, S., Sun, Y., & Xu, H. (2023). A Contribution to Improve Barrier Properties and Reduce Swelling Ratio of κ-Carrageenan Film from the

Incorporation of Guar Gum or Locust Bean Gum. *Polymers*, *15*(7). https://doi.org/10.3390/polym15071751

64. Whitaker, J. B., Kim, D. H., Larson, B. W., Zhang, F., Berry, J. J., Van Hest, M. F. A. M., & Zhu, K. (2018). Scalable slot-die coating of high-performance perovskite solar cells. *Sustainable Energy and Fuels*, *2*(11), 2442–2449. https://doi.org/10.1039/c8se00368h
65. Wu, C., Li, Y., Du, Y., Wang, L., Tong, C., Hu, Y., Pang, J., & Yan, Z. (2019). Preparation and characterization of konjac glucomannan-based bionanocomposite film for active food packaging. *Food Hydrocolloids*, *89*, 682–690. https://doi.org/10.1016/j.foodhyd.2018.11.001
66. Xue, M., Wen, Z., Huang, R., Chai, X., Li, W., Chen, C., & Chen, H. (2022). Preparation of coated paper reinforced by a blend of anionic-starch-based nanocellulose/chitosan and its properties. *RSC Advances*, *12*(35), 22402–22409. https://doi.org/10.1039/d2ra03955a
67. Yadav, M., Behera, K., Chang, Y. H., & Chiu, F. C. (2020a). Cellulose nanocrystal reinforced chitosan based UV barrier composite films for sustainable packaging. *Polymers*, *12*(1). https://doi.org/10.3390/polym12010202
68. Yadav, M., Behera, K., Chang, Y. H., & Chiu, F. C. (2020b). Cellulose nanocrystal reinforced chitosan based UV barrier composite films for sustainable packaging. *Polymers*, *12*(1). https://doi.org/10.3390/polym12010202
69. Yuan, X., Wang, J., Song, Q., & Xu, Z. (2024). Integrated assessment of economic benefits and environmental impact in waste glass closed-loop recycling for promoting glass circularity. *Journal of Cleaner Production*, *444*. https://doi.org/10.1016/j.jclepro.2024.141155
70. Zhang, Y., Bi, J., Wang, S., Cao, Q., Li, Y., Zhou, J., & Zhu, B. W. (2019). Functional food packaging for reducing residual liquid food: Thermo-resistant edible super-hydrophobic coating from coffee and beeswax. *Journal of Colloid and Interface Science*, *533*, 742–749. https://doi.org/10.1016/j.jcis.2018.09.011

Ringraziamenti

Questo percorso di dottorato è stato reso possibile grazie alla collaborazione di numerosi professionisti, ai quali desidero esprimere il mio sincero ringraziamento.

Un sentito grazie va a Davines S.p.A. (A.D. Dr. Paolo Goi) per l'interesse e il costante supporto, che hanno arricchito la mia ricerca e offerto opportunità significative che hanno avuto un impatto fondamentale sul mio cammino.

Un ringraziamento speciale va al Prof. Corrado Sciancalepore (Dipartimento di Ingegneria e Architettura), la cui esperienza nell'analisi SEM e i preziosi consigli sono stati essenziali per il mio lavoro.

Desidero anche esprimere la mia gratitudine alla Dr.ssa Claudia Forte e alla Dr.ssa Lucia Calucci (Istituto di Chimica dei Composti Organometallici - CNR, Pisa) per la loro fondamentale collaborazione nelle analisi SSNMR, che ha contribuito in modo determinante al successo del progetto.

Un ringraziamento particolare alla Prof.ssa Vanja Kokol, che mi ha accolta nel suo laboratorio con generosità, permettendomi di ampliare le mie conoscenze e crescere nel campo della ricerca.

Desidero anche, esprimere la mia più sincera riconoscenza alla Prof.ssa Antonella Cavazza per la sua continua disponibilità e per le numerose collaborazioni che hanno arricchito il mio lavoro.

Il mio percorso di dottorato, pur essendo lungo e impegnativo, è volato via in un battito di ciglia. A questo punto, mi sembra giusto fermarmi e ringraziare di cuore tutte le persone che hanno reso possibile questa straordinaria esperienza.

Innanzitutto, vorrei ringraziare ancora e dal profondo del cuore la Prof.ssa Antonella Cavazza, per la sua professionalità, umanità e per avermi accolta nel laboratorio 011, dove tutto è iniziato. Il laboratorio 011 è come un ciclone che ti avvolge e non ti lascia più: al suo interno convivono tante personalità diverse, alcune con cui ci si può scontrare, ma dove sei sempre certo di poter trovare una spalla pronta a sorreggerti. Il lab 011 non è solo un luogo di lavoro, è uno stato d'animo.

Non posso fare a meno di porgere un ringraziamento speciale a Daiana e Olimpia, che mi hanno incoraggiato a partecipare al concorso di dottorato e mi hanno accompagnato lungo questo cammino, dal momento in cui mi sono immatricolato fino ad oggi. Senza il loro incessante supporto e la loro costante vicinanza, non avrei mai avuto il coraggio di intraprendere questa avventura e non l'avrei portata a termine con le stesse consapevolezze di oggi.

I miei più sentiti ringraziamenti vanno a Edmondo, amico fidato, il cui aiuto, pazienza e incoraggiamento sono stati essenziali sin dal primo giorno. Senza il suo supporto, non avrei nemmeno intrapreso questo viaggio.

Un sincero ringraziamento va ai miei colleghi, che negli anni sono diventati veri amici. A Manuela, Stefano e Gianmarco, grazie per i loro sinceri consigli e per aver condiviso con me serate indimenticabili, fatte di discussioni stimolanti e momenti di svago.

Non posso fare a meno di ricordare tutti i ragazzi che ho incontrato negli anni, come Gianluca e Simone, che mi hanno lasciato qualcosa di unico e prezioso. Un ringraziamento speciale va a Marzia, che è stata una presenza costante e un pilastro fondamentale durante l'ultimo anno, che si è rivelato particolarmente difficile.

Un ringraziamento speciale anche a Edoardo, che è entrato nel laboratorio in punta di piedi, ma ha subito dimostrato di essere un collega eccezionale, un ottimo amico e una persona sempre pronta a sostenermi.

Grazie a Laura, che mi ha accolta nel gruppo con calore e disponibilità. La sua vicinanza e il suo supporto mi hanno permesso di crescere e migliorare nel corso degli anni.

Un sentito grazie alla mia famiglia, che è sempre stata la mia guida. Mamma e papà, anche a distanza, mi hanno dato una forza straordinaria. Il loro amore incondizionato è stato il mio supporto nei momenti più difficili e mi ha permesso di superare ogni ostacolo.

Un ringraziamento speciale va a mia sorella, che non mi ha mai lasciato sola, che è il mio punto di riferimento e fonte di forza, e che riesce a farmi affrontare ogni sfida con determinazione. Ringrazio anche Julian, ragazzo di poche parole ma di tanti sorrisi, immensa bontà e disponibilità.

Un ringraziamento di cuore ad Angela, la seconda sorella che la vita mi ha dato. La sua attenzione, la sua determinazione nello spingermi sempre a fare del mio meglio e la sua capacità di farmi superare i miei limiti sono state determinanti nel mio percorso.

Ringrazio Chiara, amica speciale e paziente, che è stata al mio fianco anche quando la distanza tra noi sembrava insormontabile. La sua amicizia è un dono raro e prezioso, una fonte di serenità e sostegno.

Un ringraziamento speciale va agli amici reggiani che mi hanno accolta con affetto in questa città, facendomi sentire meno sola: Federica, Francesca, Tommi, Emma, Filippo, Federico, Francesca Z, Anna e Michela. Grazie per essere diventati il mio punto di riferimento, per aver arricchito i miei giorni con risate, allegria e spensieratezza, rendendo ogni momento più leggero e divertente. Grazie per i momenti di confronto, per le vacanze spensierate e per esserci sempre stati, su di loro ho sempre potuto contare.

Un ringraziamento speciale va a Vittorio, che, nonostante gli anni di distanza, non mi fa sentire “estranea” quando torno in Calabria. La sua presenza affettuosa è una costante fonte di conforto.

Ringrazio Marco, il mio compagno, per il suo amore incondizionato, per essere sempre al mio fianco nei momenti più difficili, per supportarmi in tutte le mie scelte, anche quelle più audaci. La sua pazienza e il suo amore sono stati il mio rifugio sicuro. Sono grata alla vita per avermi fatto incontrare una persona così speciale.

Un ringraziamento speciale va alla Prof.ssa Claudia Graiff, per la sua straordinaria professionalità, la sua gentilezza e per essere stata una guida fondamentale durante questi tre anni di dottorato. Sono profondamente grata di aver avuto l'opportunità di lavorare al suo fianco.

A questo punto, non posso che ringraziare me stessa, per non aver mai ceduto, per aver sempre creduto che ogni difficoltà potesse essere superata, per aver affrontato ogni sfida con determinazione e per aver portato a termine questo percorso, che è stato tanto impegnativo quanto gratificante. Sono profondamente orgogliosa di tutto quello che ho costruito.

La borsa di dottorato è stata cofinanziata con risorse del

Programma Operativo Nazionale Ricerca e Innovazione 2014-2020, risorse FSE REACT-EU

Azione IV.4 “Dottorati e contratti di ricerca su tematiche dell’innovazione”

e Azione IV.5 “Dottorati su tematiche Green”